POLAR SCIENCE

Complex mesoscale landscapes beneath Antarctica mapped from space

Helen Ockenden[1,2]*, Robert G. Bingham[2]*, Daniel Goldberg[2], Andrew Curtis[2], Mathieu Morlighem[3]

The landscape shrouded by the Antarctic Ice Sheet provides important insights into its history and influences the ice response to climate forcing. However, knowledge of this critical boundary has depended on interpolation between irregularly distributed geophysical surveys, creating major spatial biases in maps of Antarctica's subglacial landscape. As stress changes associated with ice flow over bedrock obstacles produce ice surface topography, recently acquired, high-resolution satellite maps of the ice surface offer a transformative basis for mapping subglacial landforms. We present a continental-scale elevation map of Antarctica's subglacial topography produced by applying the physics of ice flow to ice surface maps and incorporating geophysical ice thickness observations. Our results enrich understanding of mesoscale (2 to 30 kilometers) subglacial landforms and unmask the spatial distribution of subglacial roughness and geomorphology.

Despite being identified by the Intergovernmental Panel on Climate Change (IPCC) as a crucial boundary condition for projections of global sea level rise (*1*, *2*), less is known about the topography beneath the ice of Antarctica than any other planetary surface in the inner solar system (*3*–*6*). Understanding of the shape and composition of Antarctica's bed has traditionally come from airborne and ground-based geophysical surveys, which although extensive, have not been acquired systematically across the ice sheet. In many regions the spacing between survey tracks remains at 10 to 100 km (*7*, *8*), much greater than the kilometer resolutions that models require to predict future sea level with low uncertainties (*9*–*12*).

In well-confined, fast-flowing ice streams, mass conservation has been used to map topography between survey lines. In the interior of Antarctica, however, existing maps of subglacial topography use interpolation techniques such as kriging, adapted plate spline interpolation (Bedmap3) (*8*) and streamline diffusion (BedMachine v3) (*13*). In regions away from survey tracks, these techniques have not been able to reproduce the roughness of subglacial terrain observed along radar profiles or mesoscale landscapes truly analogous to those exposed by deglaciation of former ice sheets (*14*–*16*). Some studies have used statistical interpolation techniques such as in-painting or super-resolution (*17*–*19*) to simulate subglacial topography with realistic roughness, but maps produced with statistical techniques have not been widely applied in ice sheet modeling as they do not always satisfy physical laws.

An alternative approach, facilitated by the development of modern satellite remote sensing technology, is to apply inverse methods to high-resolution observations of the ice surface. We employed an inverse method termed Ice Flow Perturbation Analysis (IFPA) (*20*, *21*) that leverages the physics of ice flow to invert for subglacial topography from contemporary ice surface datasets (*22*–*24*). Previous studies that have applied IFPA to data from Thwaites Glacier (*20*) and Pine Island Glacier (*21*) have shown that IFPA can reproduce the pattern of subglacial hills and valleys seen in recent ice-penetrating radar surveys. More details about the IFPA method, its known limitations, and how these have been addressed in this work can be found in the methods and supplementary text.

Using limited ice thickness measurements (*13*), we produced a map of subglacial topography that captures the mesoscale nature and roughness of the landscape (IFPA*meso*) but also contains some long-wavelength offsets to geophysical survey observations. We therefore applied an additional correction to produce a second map (IFPA) which simultaneously includes the novel mesoscale details and is consistent with all the available geophysical data (see methods). The new IFPA map deploys ice physics (based on the full Stokes equations of ice flow) across the entirety of Antarctica's interior and reveals a diversity of new mesoscale landscape details.

New windows into mesoscale landscape variability

Our IFPA map of Antarctica's subglacial landscape (Fig. 1) shows mesoscale (2 to 30 km) topographic variability across the continent with unprecedented detail (Fig. 1B, Fig. 2, and figs. S11 to S28). Newly identified features or those resolved with substantially greater detail than before include incised valleys (Fig. 2, A to C), topographic boundaries or lineations likely to have a geological or tectonic origin (Fig. 2, D and E), and topographic details in subglacial highlands (Fig. 2, F to H).

In Maud Subglacial Basin, we find a steep-sided channel incised into the subglacial substrate, with average depth 50 m and width ~6 km, running for nearly 400 km (Fig. 2A), which we hypothesize may be connected to drainage systems from the mountains of Dronning Maud Land. In Wilhelm II Land, we find evidence for a set of unsurveyed channels cutting across substantial ridges (Fig. 2B), with dimensions similar to those of sub-ice sheet channels previously identified elsewhere by airborne radar surveys (*25*–*27*). From their surface expression, these channels have been hypothesized to form part of an extensive hydrological system draining from Subglacial Lake Qilin (*28*, *29*). Our map also reveals incised valleys across higher-elevation blocks, such as Hercules Dome, where several deep valleys cut across the subglacial plateau (Fig. 2C). These valleys are similar to "U-shaped" glacial valleys imaged nearby with multi-element swath radar, which have been interpreted to represent alpine glaciation in an initiation zone for ice sheet growth (*30*). Additional definition is added to channels in the Slessor Glacier Basin, Blackwall Glacier Trough, and between Highlands B and C (figs. S14.8, S14.7, and S26.32 respectively).

The IFPA-derived subglacial topography effectively captures sharp edges in basal topography that may characterize geological boundaries, as exemplified in Recovery Subglacial Basin (Fig. 2D). Radar surveys of the basin have shown that there is a region of raised topography in the center of the basin (*31*), flanked by lower ground in which sits a series of subglacial lakes (*32*, *33*). The lowlands versus highlands have broadly been interpreted from gravity and magnetic surveys to represent sedimentary basins versus crystalline massifs (*34*), but the wide spacing of the radar tracks had left the boundary between the two geological regions poorly resolved. Our map clearly picks out a sharp, linear transition between the two terrains (Fig. 2D). Further insight into subglacial geology is provided around East Antarctica's Zhigalov Subglacial Mountains, where the more finely resolved subglacial topography shows multiple features following a consistent strong north-south trend (Fig. 2E). Further west in the more intensively aerogeophysically surveyed Dronning Maud Land, similar north-south–trending landforms have been attributed to Paleozoic to Mesozoic rifting (*35*). We also see a much clearer outline of the boundary between Astrolabe Subglacial Basin and Porpoise Subglacial Highlands (fig. S25.29), as well as previously unresolved topographic structures along the crests of those highlands. The IFPA

[1]L'Institut des Géosciences de l'Environnement, Université Grenoble-Alpes, Saint-Martin-d'Hères, France. [2]School of GeoSciences, University of Edinburgh, Drummond Street, Edinburgh, UK. [3]Department of Earth Sciences, Dartmouth College, Hanover, NH, USA
***Corresponding author. Email: helen.ockenden@univ-grenoble-alpes.fr (H.O.); r.bingham@ed.ac.uk (R.G.B.)**

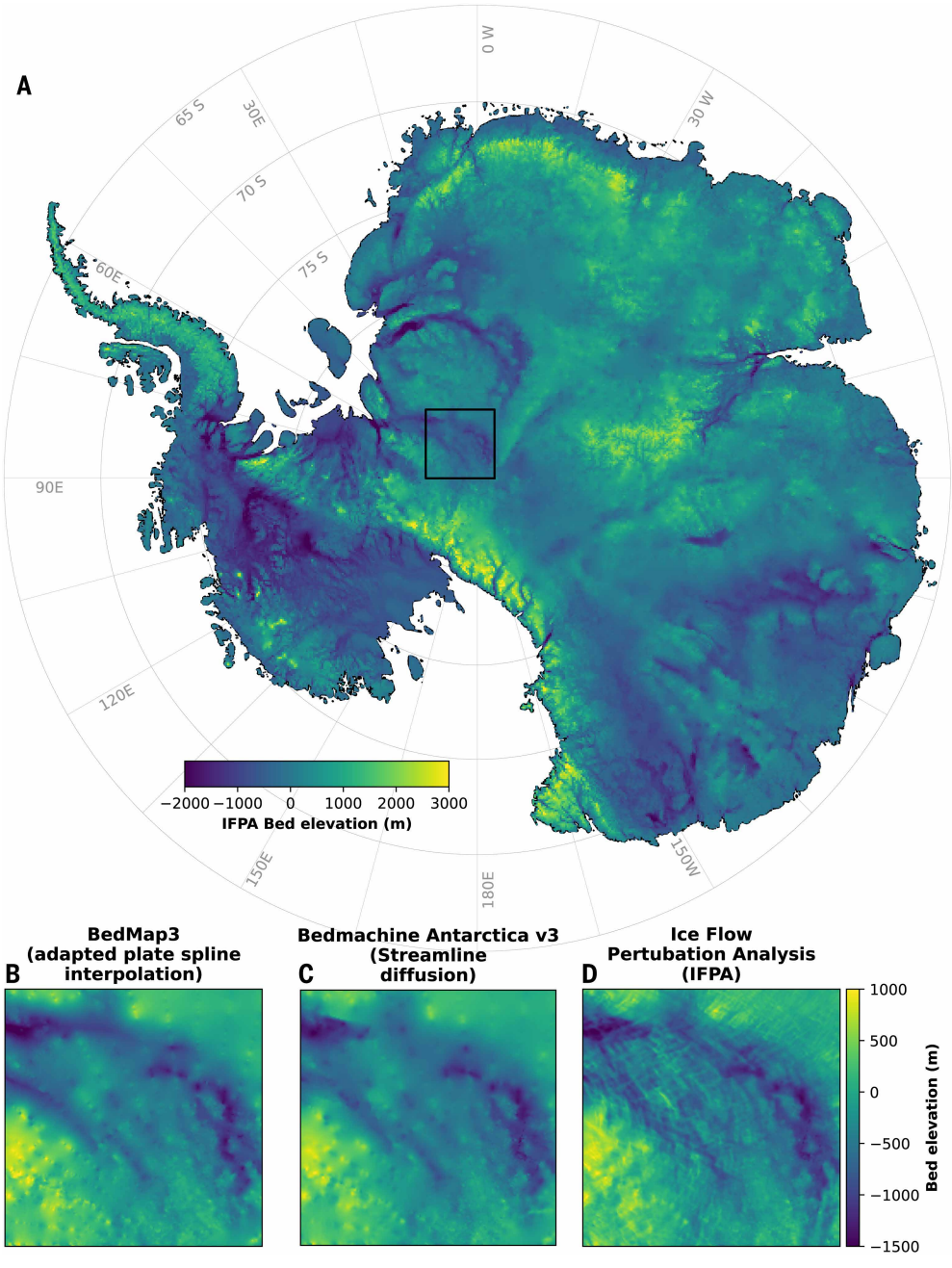

Fig. 1. IFPA subglacial topography of Antarctica. (**A**) shows the IFPA subglacial topography for the whole Antarctic continent and (**B** to **D**) show a comparison of different bed topography maps for the Pensacola-Pole Basin region [outlined in black on (A). (B) displays Bedmap3 (*8*), (C) displays BedMachine Antarctica v3 (*13*), and (D) displays IFPA subglacial topography. The map production workflow is detailed in the methods; the main input datasets include the Gapless REMA ice-surface digital elevation model (*24*), the MEaSURES Antarctic ice-velocity product (*23*), the BedMachine Antarctica v3 bed-elevation map (*13*), and all available geophysical survey measurements of ice thickness from Bedmap3 (*7*) and CReSIS SAR surveys (*59*). A considerably higher resolution version of (A) is available on Zenodo (*57*).

map identifies some small topographic features in the depths of Astrolabe Subglacial Basin, supporting the suggestion by geophysical surveys that subglacial water in the region is most likely not concentrated into a single lake but rather distributed across a more marsh-type environment (*36*).

We also resolve the mesoscale landscapes of Antarctica's subglacial highlands with unprecedented clarity for all of Antarctica's most poorly surveyed regions. For example, across highland blocks flanking East Antarctica's deep subglacial basins, we detect geometric features that resemble alpine valleys cutting across the highlands (Fig. 2, F and G). In the Highland A region, where these features have been surveyed by airborne radar, they have been interpreted as a preserved paleo-river landscape (*27*); our map shows a widespread distribution of these features across the continent's highlands. The new map also unmasks numerous new dendritic valley-ridge complexes thought to be diagnostic of alpine glaciation in other sparsely surveyed subglacial highlands of East Antarctica, such as the Golicyna Subglacial Mountains (Fig. 2H) (*37*).

The texture of Antarctica's ice sheet bed

To quantify the mesoscale subglacial landscape textures described above across the whole Antarctic continent, we applied a range of metrics to the IFPA map (methods). For comparison, we also applied these techniques to two of the most recently available bed Digital Elevation Models (DEMs): BedMachine Antarctica v3 (*13*) and Bedmap3 (*8*), which use streamline diffusion and adapted plate spline interpolation, respectively, to interpolate between geophysical surveys. The spatial pattern in texture obtained from the IFPA map contrasts strongly with those shown for the interpolated DEMs (Fig. 3), in which the spatial variability corresponds far more closely to the uneven distribution of ice-penetrating radar observations (Fig. 3C and S7). Our results give a new overview of the pancontinental subglacial landscape and allow us to generate the first picture of the texture of the entire Antarctic bed that leverages the physics of ice flow and high-resolution ice surface datasets to significantly reduce bias from geophysical survey density.

As a measure of mesoscale (2 to 30 km) topographic variability and a proxy for subglacial roughness, we consider the distribution of subglacial hills (defined as local maxima with at least 50 m of topographic prominence in a 5-km neighborhood). We identify twice as many subglacial hills in the IFPA topography map (71,997) than are counted in BedMachine Antarctica v3 (36,346), (Fig. 3A). The Bedmap3 hill count falls between these two values, but at mesoscale resolution it is highly influenced by ice thickness survey locations (fig. S7). We also see higher fractal dimensions (a spectral measure of topographic roughness at different length scales, sometimes linked to basal drag) (*15*, *38*) in the IFPA map (Fig. 3B), especially in regions where we know from geophysical surveying that there is elevated, rough topography. Alongside the topography map, these roughness

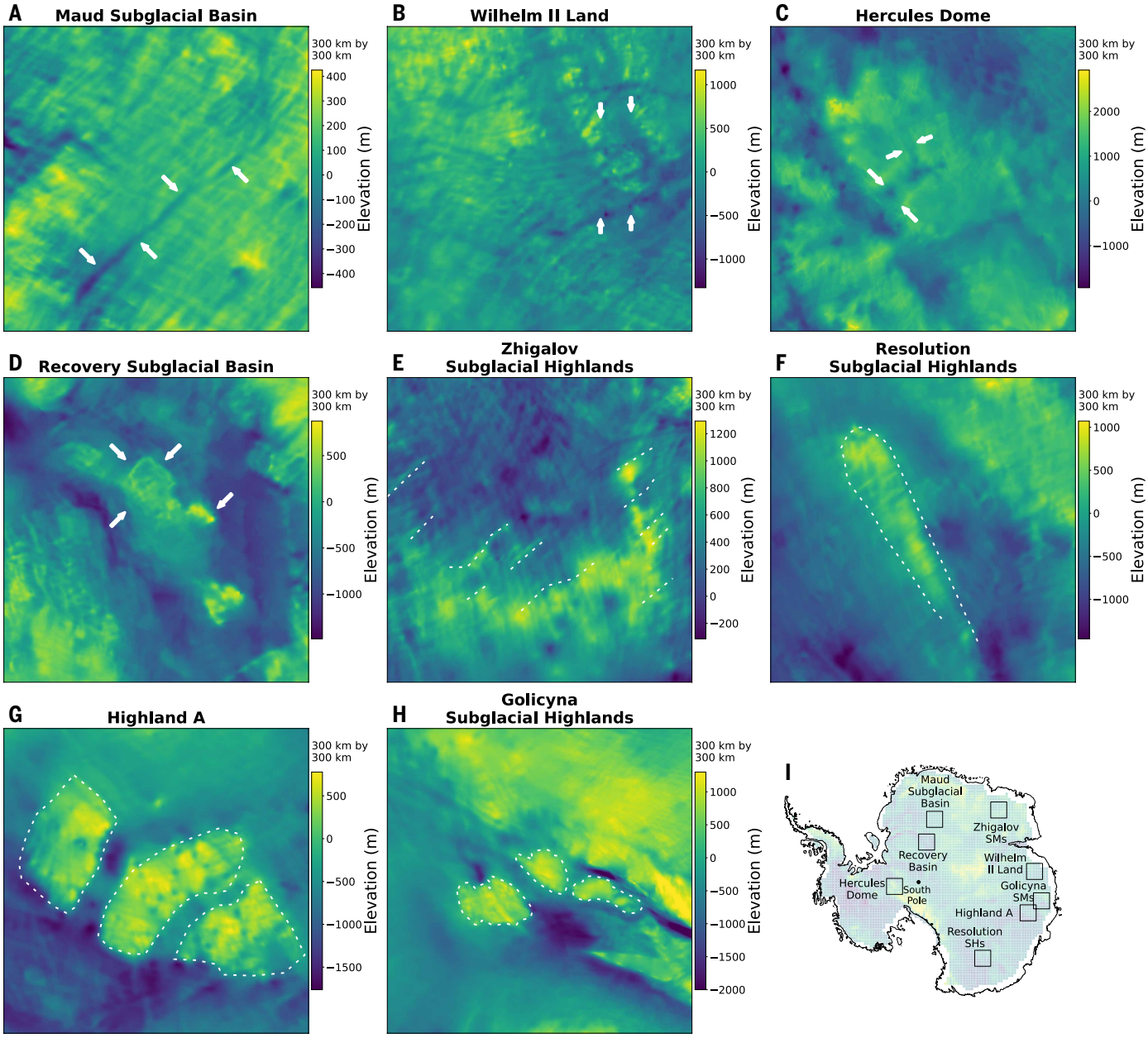

Fig. 2. Selected examples of new IFPA subglacial topography. (**A** to **C**) Examples of channels incised into the subglacial substrate; (**D** and **E**) improved definition of subglacial topographic lineations likely related to tectonics; and (**F** to **H**) newly defined topography in subglacial highlands. Note that the panels vary in size from 100 × 100 km to 300 × 300 km. (**I**) Panel locations. Key linear features are annotated with white arrows and area features are outlined with dotted white lines. See supplementary figures for examples shown alongside topography from BedMachine Antarctica v3 (*13*) and Bedmap3 (*8*), as follows: Maud Subglacial Basin (fig. S16.11), Hercules Dome (fig S13.5), Recovery Subglacial Basin (fig. S16.12), Zhigalov Subglacial Highlands (figs. S24.28 and S28.36), Resolution Subglacial Highlands (fig. S22.23), Highland A (fig.S26.32), Golicyna Subglacial Highlands (fig. S27.34).

metrics may provide important insights into basal drag, a key boundary condition for ice sheet models.

The landscape beneath Antarctica's ice

Research on formerly glaciated landscapes has demonstrated that broad-scale relationships exist between the nature of the landscape and its glacial history (*39*–*41*). High-relief alpine landscapes are produced by cirque and valley glaciers in elevated regions, at the beginning and end of glaciations (*42*, *43*). Low-relief landscapes [such as central northern Canada (*39*) and coastal Scandinavia (*44*)] have been inferred to represent ubiquitous erosion (previously termed areal scouring) beneath unconstrained ice flow with abundant subglacial meltwater, during peak glaciation. In regions with variable hydrological conditions, landscapes of "selective erosion" develop, in which terrains of low-relief high ground (protected from erosion due to basal freezing) are dissected by deeply eroded glacial troughs (recording where water and thus erosion occurred at some time) (*45*, *46*).

Using selected example regions of low-relief, alpine, and selectively eroded topography, as well as the textural characteristics detailed in the methods, we made a simple division of the landscape of Antarctica into regions by topographic style. As we focused on

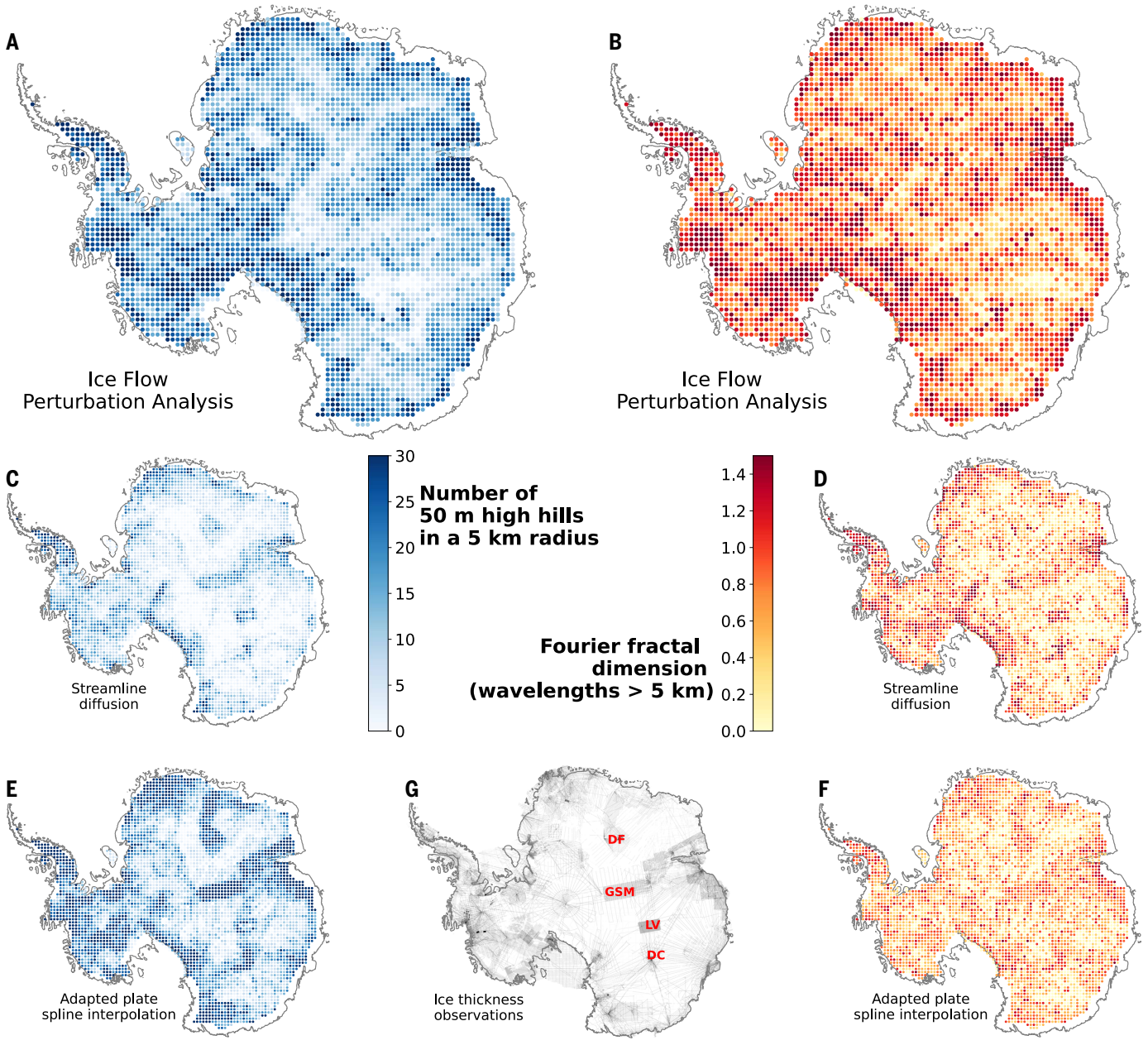

Fig. 3. The texture of Antarctica's ice sheet bed. (**A**, **C**, and **E**) Number of 50-m hills within a 5-km radius and (**B**, **D**, and **F**) Fourier fractal dimension for wavelengths >5 km (a proxy for subglacial landscape roughness), extracted from (A) and (B) IFPA topography, (C) and (D) topography interpolated between geophysically derived bed picks using streamline diffusion (BedMachine Antarctica v3) (*13*), and (E) and (F) an adapted plate spline interpolation (Bedmap3) (*7*,*8*). Each pixel represents a 50 km × 50 km region. (**G**) Locations of bed picks used to derive both interpolated topographies (From Bedmap3 thickness survey count) (*8*). The most densely surveyed regions of East Antarctica are annotated: DF, Dome Fuji; GSM, Gamburtsev Subglacial Mountains; LV, Lake Vostok; DC, Dome C. Note the significant correspondence between the spatial patterns in interpolated topographies (C) and (E) and geophysical survey locations (G). By contrast, (A) and (B) show that with IFPA we can now calculate subglacial landscape texture across Antarctica consistently, without major bias from geophysical survey locations.

metrics of mesoscale texture, the characteristics employed for this classification were calculated using the IFPA*meso* map to give a self-consistent picture of the subglacial landscape and reduce the effect of uneven geophysical survey spacing. This is the first landscape classification applied to a subglacial DEM produced primarily from ice surface datasets, and the first to reveal landscape dynamics across the whole continent including for regions away from geophysical survey lines.

Although all major subglacial mountain ranges in Antarctica have already been identified in previous studies (*37*, *47*, *48*), the greater revelations of our IFPA*meso*-guided classification lie in the respective distributions of low-relief and selectively eroded landscapes, which deviate from previous mapping and interpretations. Notably, we identify fewer regions of low-relief topography. In part this is because many of the areas identified (*42*) as having low-relief subglacial topography in 2014 ("areal scour") were located in gaps between radar surveys (e.g., Princess Elizabeth Land, central Dronning Maud Land, and the South Pole Basin), and were naturally, albeit erroneously, recorded as flatter ground than our IFPA*meso* analysis shows. Our classification clarifies that most of Antarctica's low-subglacial relief

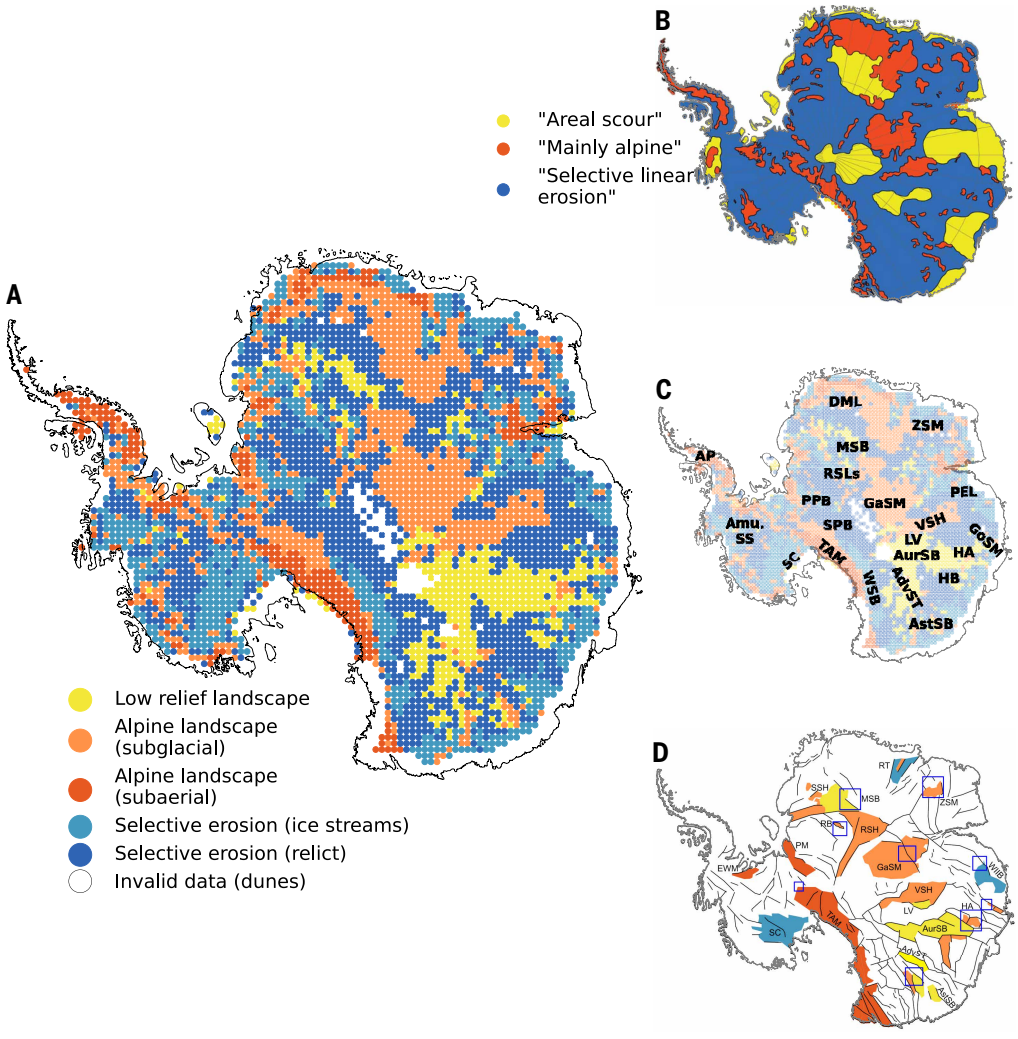

Fig. 4. Geomorphological classification of Antarctica's subglacial landscape. (**A**) Application to IFPA*meso* subglacial topography. (**B**) Previous classification applied in 2013 to interpolated bed topography (Bedmap2) (*60*), adapted from Jamieson *et al*. (*42*). In each panel the classification shows regions of low-relief, alpine (both fully submerged–subglacial and partially submerged–subaerial) and selectively eroded landscapes. (**C**) Locations discussed in text. (**D**) Locations of tectonic boundaries across Antarctica, adapted from (*34*). We have colored some examples of regions where the geological structure mirrors the tectonic structures that we see. Adv. ST, Adventure Subglacial Trench; Amu. SS, Amundsen Sea Sector; AP, Antarctic Peninsula; Ast SB, Astrolabe Subglacial Basin; Aur SB, Aurora Subglacial Basin; DML, Dronning Maud Land; EWM, Ellsworth Mountains; GaSM, Gamburtsev Subglacial Mountains; GoSM, Golicyna Subglacial Mountains; HA, Highland A; HB, Highland B; LV, Lake Vostok; MSB, Maud Subglacial Basin; PEL, Princess Elizabeth Land; PM, Paxutent Mountains; PPB, Pensacola-Pole Basin; RT, Ragnhild Trough; RSH, Recovery Subglacial Highlands; RSLs, Recovery Subglacial Lakes; SC, Siple Coast; SPB, South Pole Basin; WIIB, Wilhelm II Basin; WSB, Wilkes Subglacial Basin; ZSM, Zhigalov Subglacial Mountains.

regions are in central East Antarctic basins thought to contain deep sedimentary infills (*49*, *50*) and confined by tectonic boundaries observed in magnetic and gravity surveys (e.g., Aurora Subglacial Basin, Adventure Subglacial Trench, and Maud Subglacial Basin, Fig. 4D). Low-relief landscapes are also seen in regions previously identified as containing a high density of subglacial lakes [e.g., Recovery Subglacial Lakes (*32*) and Astrolabe Subglacial Basin (*51*)]. Our classification reimagines the interpretation of the lowest-relief subglacial topography in the interior of Antarctica, suggesting that substantial landscapes of areally scoured bedrock are likely to be rare in actively glaciated regions, and that in the interior these landscapes instead represent wide-ranging regions of sedimentary infill. However, this does not mean that there are not landscapes of areal scour present, only that more sophisticated methods are required to identify them.

In our textural classification, areas collectively termed as resulting from selective erosion cover 56% of Antarctica and describe any topography that is not clearly low-relief or alpine. We further identified a subclass of these regions, with high RMS slope and low fractal dimension (methods), geographically clustered around present-day ice streams such as those along the Siple Coast (figs. S12.3 and S12.4b), the Amundsen Sea Sector, and the Pensacola-Pole Basin. This allowed us to distinguish between areas where we hypothesize erosion is an active modern day process and areas where the relict landscape of selective erosion is preserved in the absence of major ice streams and variable ice flow today (figs. S25.30 and S27.33). These preserved landscapes may reflect multiple phases of past ice sheet growth and retreat of a less extensive Antarctic Ice sheet, most likely before the mid-Miocene (14 million years ago) (*52*). Radio-echo soundings from Highland B (*53*) confirm the presence of landscapes where deep troughs selectively breach uplands around ice sheet margins, and there are numerous analogs around the fringes of East Greenland and various Arctic ice caps (*54*–*56*).

Mapping a way ahead

Our IFPA map of Antarctica's subglacial landscape reveals that an enormous level of detail about the subglacial topography of Antarctica can be inverted from satellite observations of the ice surface, especially when combined with ice thickness observations from geophysical surveys (*7*, *13*). We have used the map to illustrate the step forward we have taken in our understanding of the mesoscale (2 to 30 km) topography beneath Antarctica, exploring selected examples of the landscape features that it uncovers, and showing that previous topographic maps have been limited by bias toward geophysical survey locations. Additionally, from the mesoscale texture of this new topography, we have interpreted primary glacial geomorphological regimes across the Antarctic continent and thus provided insights for developments in the process of understanding of ice sheet history and future ice sheet dynamics.

Although IFPA cannot resolve features that are shorter in length than the ice thickness, because flow over these features does not induce any perturbations in the ice surface, landscapes tend to have fractal roughness structures (*15*), meaning that the mesoscale textures that we identify will be correlated with small-scale roughness and can provide

information about ice flow regimes (*38*). Our landscape classification and topographic map therefore serve as important guides toward more focused studies of Antarctica's subglacial landscape, informing where future detailed geophysical surveys should be targeted, as well as the extents and resolutions (e.g., flight-track spacing) required to capture the fine details required for ice flow modeling.

REFERENCES AND NOTES

1. Intergovernmental Panel on Climate Change (IPCC), "The Ocean and Cryosphere in a Changing Climate: Special Report of the Intergovernmental Panel on Climate Change" (Cambridge Univ. Press, 2022); https://doi.org/10.1017/9781009157964.
2. Intergovernmental Panel on Climate Change (IPCC), "9 – Ocean, Cryosphere and Sea Level Change" (Cambridge Univ. Press, 2023); https://doi.org/10.1017/9781009157896.011.
3. K. Gwinner *et al.*, *Earth Planet. Sci. Lett.* **294**, 506–519 (2010).
4. R. R. Herrick, D. L. Stahlke, V. L. Sharpton, *Eos* **93**, 125–126 (2012).
5. K. J. Becker *et al.*, "First global digital elevation model of Mercury" in *47th Annual Lunar and Planetary Science Conference* (2016); pp. 2959.
6. Y. Yu, D. T. Sandwell, G. Dibarboure, *Science* **386**, 1251–1256 (2024).
7. A. C. Frémand *et al.*, *Earth Syst. Sci. Data* **15**, 2695–2710 (2023).
8. H. D. Pritchard *et al.*, *Sci. Data* **12**, 414 (2025).
9. G. Durand, O. Gagliardini, L. Favier, T. Zwinger, E. le Meur, *Geophys. Res. Lett.* **38**, L20501 (2011).
10. S. Sun, S. L. Cornford, Y. Liu, J. C. Moore, *Cryosphere* **8**, 1561–1576 (2014).
11. F. McCormack, B. Galton-Fenzi, H. Seroussi, J. Roberts, The impact of bed elevation resolution on Thwaites Glacier ice dynamics. *Twenty-Fifth Annual WAIS Workshop* (2018).
12. B. A. Castleman, N.-J. Schlegel, L. Caron, E. Larour, A. Khazendar, *Cryosphere* **16**, 761–778 (2022).
13. M. Morlighem *et al.*, *Nat. Geosci.* **13**, 132–137 (2020).
14. M. Margold, C. R. Stokes, C. D. Clark, *Earth Sci. Rev.* **143**, 117–146 (2015).
15. K. A. Hogan *et al.*, *Cryosphere* **14**, 2883–2908 (2020).
16. F. A. M. Falcini, M. Krabbendam, K. A. Selby, D. M. Rippin, *J. Glaciol.* **68**, 518–532 (2022).
17. E. MacKie, D. Schroeder, J. Caers, M. Siegfried, C. Scheidt, . *J. Geophys. Res. Earth Surf.* **125**, e2019JF005420 (2020).
18. W. J. Leong, H. J. Horgan, *Cryosphere* **14**, 3687–3705 (2020).
19. Y. Cai *et al.*, *IEEE Trans. Geosci. Remote Sens.* **61**, 1–17 (2023).
20. H. Ockenden, R. G. Bingham, A. Curtis, D. Goldberg, *Cryosphere* **16**, 3867–3887 (2022).
21. H. Ockenden, R. G. Bingham, A. Curtis, D. Goldberg, *J. Glaciol.* **69**, 1–10 (2023).
22. I. M. Howat, C. Porter, B. E. Smith, M.-J. Noh, P. Morin, *Cryosphere* **13**, 665–674 (2019).
23. J. Mouginot, E. Rignot, B. Scheuchl, *Geophys. Res. Lett.* **46**, 9710–9718 (2019).
24. Y. Dong, J. Zhao, C. Li, M. Liao, *ISPRS J. Photogramm. Remote Sens.* **186**, 70–82 (2022).
25. K. C. Rose *et al.*, *Geology* **42**, 971–974 (2014).
26. S. J. Livingstone, W. Chu, J. C. Ely, J. Kingslake, *Geology* **45**, 551–554 (2017).
27. S. S. R. Jamieson *et al.*, *Nat. Commun.* **14**, 6507 (2023).
28. S. S. R. Jamieson *et al.*, *Geology* **44**, 87–90 (2016).
29. X. Cui *et al.*, *Earth Syst. Sci. Data* **12**, 2765–2774 (2020).
30. A. O. Hoffman *et al.*, *Nat. Geosci.* **16**, 1–9 (2023).
31. R. E. Bell, M. Studinger, C. A. Shuman, M. A. Fahnestock, I. Joughin, *Nature* **445**, 904–907 (2007).
32. A. Humbert, D. Steinhage, V. Helm, S. Beyer, T. Kleiner, *J. Geophys. Res. Earth Surf.* **123**, 2802–2826 (2018).
33. A. Diez *et al.*, *J. Geophys. Res. Earth Surf.* **124**, 287–304 (2019).
34. A. R. A. Aitken *et al.*, *Reviews of Geophysics* **61**, e2021RG000767 (2023).
35. O. Eisen, A. Winter, D. Steinhage, T. Kleiner, A. Humbert, *Ann. Glaciol.* **61**, 162–175 (2020).
36. D. W. Ashmore, R. G. Bingham, *Antarct. Sci.* **26**, 758–773 (2014).
37. E. J. Lea, S. S. Jamieson, M. J. Bentley, *Cryosphere* **18**, 1733–1751 (2024).
38. C. Schoof, *J. Glaciol.* **48**, 407–416 (2002).
39. D. E. Sugden, B. S. John, *Edward Arnold London* **365**, 1–363 (1976).
40. M. J. Siegert, J. Taylor, A. J. Payne, *Global Planet. Change* **45**, 249–263 (2005).
41. S. Franke *et al.*, *Earth Surf. Process. Landf.* **46**, 2728–2745 (2021).
42. S. S. Jamieson *et al.*, *Antarct. Sci.* **26**, 724–741 (2014).
43. C. Lambiel, B. Maillard, M. Kummert, E. Reynard, *J. Maps* **12**, 160–172 (2016).
44. O. Fredin *et al.*, *Nat. Commun.* **8**, 14879 (2017).
45. D. Sugden, *J. Glaciol.* **20**, 367–391 (1978).
46. A. M. Hall, K. Ebert, J. Kleman, A. Nesje, D. Ottesen, *Geology* **41**, 1203–1206 (2013).
47. F. Ferraccioli *et al.*, New aerogeophysical survey targets the extent of the West Antarctic Rift System over Ellsworth Land. in *10th International Symposium on Antarctic Earth Sciences*. A. K. Cooper, C. R. Raymond, Eds. (USGS, 2007); Extended Abstract 113, pp. 1–10.
48. T. T. Creyts *et al.*, *Geophys. Res. Lett.* **41**, 8114–8122 (2014).
49. A. Baranov, A. Morelli, A. Chuvaev, *Front. Earth Sci. (Lausanne)* **9**, 722699 (2021).
50. A. R. A. Aitken *et al.*, *Geophys. Res. Lett.* **41**, 2390–2400 (2014).
51. M. J. Siegert, N. F. Glasser, *Polar Res.* **16**, 63–72 (1997).
52. D. E. Sugden, S. S. Jamieson, *Scott. Geogr. J.* **134**, 203–223 (2018).
53. D. A. Young *et al.*, *Nature* **474**, 72–75 (2011).
54. H. Holtedahl, *Geogr. Ann., Ser. A* **49**, 188–203 (1967).
55. O. H. Løken, D. Hodgson, *Can. J. Earth Sci.* **8**, 185–195 (1971).
56. D. Sugden, *Landscapes of Glacial Erosion in Greenland and their Relationship to Ice, Topographic and Bedrock Conditions* (Univ. of Aberdeen, 1974); 177–195.
57. H. Ockenden, Data accompanying manuscript: Complex mesoscale landscapes beneath Antarctica mapped from space, v3, Zenodo (2025); http://dx.doi.org/10.5281/zenodo.15223468.
58. H. Ockenden, hockenden97/Antarctic_subglacial_topo: Minor edits to figures, v4.0.0, Zenodo (2025); https://zenodo.org/records/17601672.
59. CReSIS, Center for Remote Sensing of Ice Sheets (CReSIS) radio-echo sounding data repository, Open Polar Data Centre (2025); https://data.cresis.ku.edu/data/rds/.
60. P. Fretwell *et al.*, *The Cryosphere* **7**, 375–393 (2013).

ACKNOWLEDGMENTS

This research has only been made possible through the many colleagues behind the acquisition, analysis, and open publication of the underpinning satellite datasets. In particular, we acknowledge DigitalGlobe (now Maxar Technologies); WorldView and GeoEye programmes for REMA; JAXA's ALOS; ESA's Envisat and ERS; NASA's Landsat; CSA's RADARSAT programmes for MEaSUREs; University of Minnesota's NSF-funded Polar Geospatial Data Center for REMA; NASA and NSIDC for MEaSUREs; and the provision and open publication of six decades of geophysical dataset acquisition across Antarctica by multiple colleagues in the Scientific Committee for Antarctic Research Bedmap consortium. To all of these colleagues, we extend our gratitude and appreciation. The authors also thank S. Jamieson and G. Paxman for valuable comments on an early draft and the two referees of this paper, whose reviews significantly improved the final manuscript. **Funding:** This research was supported by the Natural Environment Research Council (NERC) E4 Doctoral Training Partnership (grant NE/S007407/1), the International Thwaites Glacier Collaboration (ITGC, grant nos. NERC NE/S006672, NERC NE/S006621/1, NERC NE/S006613/1, NERC NE/S006796/1, NSF PLR 1738934), and the Evans Family Fellowship (through a postgraduate fellowship for H.O. to visit Dartmouth College), and the ANR AIAI project (ANR-22-CE01-0014). This is ITGC Contribution No. ITGC-161. **Author contributions:** Conceptualization: H.O., R.G.B., D.G., and A.C.; Code development and mapping: H.O. and M.M.; Analysis & interpretation: H.O. and R.G.B.; Visualization: H.O.; Writing (original draft): H.O. and R.G.B.; Writing (review & editing): H.O., R.G.B., D.G., A.C., and M.M. **Competing interests:** The authors declare no competing interests. **Data, code, and materials availability:** The IFPA map dataset and other datasets required to produce the figures in this manuscript are available on Zenodo (*57*). The code used to generate the IFPA map presented here, and the figures in this manuscript, is available on GitHub and (*58*). All other data needed to evaluate the conclusions in the paper are present in the paper or the supplementary material. No samples or new materials were collected or generated for this study. **License information:** Copyright © 2026 the authors, some rights reserved; exclusive licensee American Association for the Advancement of Science. No claim to original US government works. https://www.science.org/content/page/science-licenses-journal-article-reuse

SUPPLEMENTARY MATERIALS

science.org/doi/10.1126/science.ady2532
Methods; Supplementary Text; Figs. S1 to S28; References (*61–80*)

Submitted 15 April 2025; accepted 25 November 2025

10.1126/science.ady2532

Science
AAAS

Supplementary Materials for

Complex mesoscale landscapes beneath Antarctica mapped from space

Helen Ockenden *et al*.

Corresponding authors: Helen Ockenden, helen.ockenden@univ-grenoble-alpes.fr; Robert G. Bingham, r.bingham@ed.ac.uk

Science **391**, 314 (2026)
DOI: 10.1126/science.ady2532

The PDF file includes:

Methods

Ice Flow Perturbation Analysis

When ice flows over perturbations in the bed topography and slipperiness, this creates variability in the ice-surface elevation and velocity fields (*61–63*). The Ice Flow Perturbation Analysis (IFPA) methodology leverages this relationship and high-resolution observations of the ice surface to invert for bed topography, and is based on a mathematical framework developed by Gudmundsson (2003, 2008) (*64, 65*), and which describes the physics of ice flowing over perturbations for an ice slab of constant viscosity and isotropic rheology. Although those works considered perturbations evolving through time, for the IFPA methodology presented here, we simplify the physics by assuming a steady state, removing the need for a Laplace transform, and by linearising the system, with the assumption of flow approximated by a planar slab with constant viscosity and isotropic rheology.

Previous works explored the suitability of IFPA and these assumptions for inverting Antarctic bed topography, and concluded that when applied to Thwaites Glacier (*20*) and Pine Island Glacier (*21*), in West Antarctica, IFPA produces realistic topography which correlates well with the features seen in ice-penetrating radar surveys, even when little or no information on the ice thickness is available. The amplitude of subglacial features depends on the basal slipperiness prescribed in the inversion. Although basal slipperiness is not well constrained by observations, this parameter can be tuned using ice-penetrating radar surveys (*21*). Here, we extend this work by applying IFPA to the entire Antarctic continent.

The mathematics of Ice Flow Perturbation Analysis

For ice flowing in a planar slab aligned in the direction of ice flow, the non-dimensionalised Fourier transforms of perturbations in ice-surface elevation, ($\hat{S}$), and velocity, ($\hat{U}$, $\hat{V}$), can be calculated from the non-dimensionalised Fourier transforms of perturbations in bed topography, ($\hat{B}$), and basal slipperiness, ($\hat{C}$):

$$\hat{S}(k,l) = T_{SB}(k,l)\ \hat{B}(k,l) + T_{SC}(k,l)\ \hat{C}(k,l), \tag{S1}$$

$$\hat{U}(k,l) = T_{UB}(k,l)\ \hat{B}(k,l) + T_{UC}(k,l)\ \hat{C}(k,l), \tag{S2}$$

$$\hat{V}(k,l) = T_{VB}(k,l)\ \hat{B}(k,l) + T_{VC}(k,l)\ \hat{C}(k,l), \tag{S3}$$

where T_{SB}, T_{SC}, T_{UB}, T_{UC}, T_{VB}, T_{VC} are wavenumber specific non-dimensional transfer functions which describe the ratio of perturbations in the bed properties relative to the ice-surface properties, and which vary with the wavenumbers k and l, angle of slope α, sliding-law parameter m, and mean non-dimensional slipperiness $\bar{C}$. The wavenumber j is calculated as $j^2 = k^2 + l^2$.

For full-Stokes flow, as applied to produce the maps presented in this manuscript, these transfer functions take the following forms (see Gudmundsson 2003 (*64*) for the full derivation,):

$$T_{SB\,num}(k,l) = jk\Big((1+\bar{C})\big(\bar{C}j\sinh(j)+\cosh(j)\big)+\cosh(j)\big(1+\bar{C}+\bar{C}^2j^2\big)\Big), \tag{S4}$$

$$\begin{aligned} T_{S\,den}(k,l) =& jk(1+\bar{C})\Big(\cosh(j)\big(\bar{C}j\sinh(j)+\cosh(j)\big)+1+j^2\big(1+\bar{C}\big)\Big) \\ &+ i\cot(\alpha)\Big(\big(Cj\sinh(j)+\cosh(j)\big)\sinh(j)-j\Big), \end{aligned} \tag{S5}$$

$$T_{SB}(k,l) = T_{SB\,num}(k,l) \,/\, T_{S\,den}(k,l), \tag{S6}$$

$$\begin{aligned} T_{UB\,num}(k,l) =& \Big(\sinh^2(j)\Big(j^2\cot(\alpha)\sinh(j)\cosh(j)\Big(\bar{C}\big(2-k^2(\bar{C}^2j^2+4+\bar{C})\big)+4\Big) \\ &+ ik\Big(j^4\bar{C}\Big(3\bar{C}k^2(1+\bar{C})-4\Big)+2\Big(j^2\big(k^2(4\bar{C}+2+\bar{C}^2)+4+4\bar{C}\big)-2k^2(1+\bar{C})\Big) \\ &+ j^3\Big(\bar{C}^3j^2\big(k^2(1+\bar{C})+2\big)+\bar{C}k^2\big(5\bar{C}+4\big)+2\big(3\bar{C}-2\big)\big(1+\bar{C}\big)\Big)-4k^2j\bar{C}(1+\bar{C})\Big) \\ &+ j\cot(\alpha)\Big(\big(-3\bar{C}^2k^2+2\bar{C}(2+\bar{C})\big)j^2-k^2(2+\bar{C})^2\Big)\Big)-2j^3\cot(\alpha)\Big(\bar{C}^2k^2+\bar{C}+2\Big) \\ &+ 2ikj\Big(j^2\Big(k^2\big(5\bar{C}^2+6\bar{C}+2\big)-4-4\bar{C}\Big)-j^4\Big(2+5\bar{C}+4\bar{C}^2\Big)+2k^2\Big(1+\bar{C}\Big)\Big)\Big), \end{aligned} \tag{S7}$$

$$\begin{aligned} T_{vel\,den}(k,l) =& j^2\Big(j\cosh^3(j)\Big(ik(1+\bar{C})\Big(\bar{C}^2j^2+2\Big)-3\bar{C}\cot(\alpha)\Big) \\ &+ j\cosh(j)\Big(\cot(\alpha)\Big(2+3\bar{C}\Big)-ik(1+\bar{C})\Big(j^2\big(\bar{C}^2-2\bar{C}-2\big)-2\Big)\Big) \\ &+ \sinh^3(j)\Big(3ikj^2\bar{C}\Big(1+\bar{C}\Big)-\cot(\alpha)\Big(2+\bar{C}^2j^2\Big)\Big) \\ &+ \sinh(j)\Big(\cot(\alpha)\Big(j^2\bar{C}-2\Big)+ikj^2\bar{C}(1+\bar{C})\Big(j^2(1+\bar{C})+4\Big)\Big)\Big), \end{aligned} \tag{S8}$$

$$T_{UB}(k,l) = T_{UB\,num}(k,l) \,/\, T_{vel\,den}(k,l), \tag{S9}$$

$$
\begin{aligned}
T_{VB\ num}(k,l) =& kl\Big(\sinh(j)\cosh(j)\Big(ik\Big(3\bar{C}^2 j^4(1+\bar{C}) + 2j^2(2+4\bar{C}+\bar{C}^2) - 4 - 4\bar{C}\Big) \\
&\quad - j^2\bar{C}\cot(\alpha)\Big(j^2\bar{C}^2 + \bar{C} + 4\Big)\Big) \\
&+ \sinh^2(j)\Big(ikj\Big(\bar{C}^3 j^4(1+\bar{C}) + \bar{C}j^2(5\bar{C}+4) - 4\bar{C}(1+\bar{C})\Big) \\
&\quad - j\cot(\alpha)\Big(3j^2\bar{C}^2 + (2+\bar{C})^2\Big)\Big) \\
&- 2\bar{C}^2 j^3\cot(\alpha) + 2ikj\Big(j^2\Big(5\bar{C}^2 + 6\bar{C} + 2\Big) + 2 + 2\bar{C}\Big)\Big)
\end{aligned} \tag{S10}
$$

$$
T_{VB}(k,l) = T_{VB\ num}(k,l)\ /\ T_{vel\ den}(k,l), \tag{S11}
$$

$$
T_{SC}(k,l) = \Big(-\bar{C}kj\cosh(j)\Big)\ /\ T_{s\ den}(k,l), \tag{S12}
$$

$$
\begin{aligned}
T_{UC\ num}(k,l) =& \bar{C}\Big(\sinh(j)\cosh(j)\Big(j^2\cot(\alpha)\Big(\bar{C}k^2 - 2\Big) \\
&\quad + ik\Big(2\bar{C}j^4(1+\bar{C}) - j^2\Big(k^2(2+\bar{C})(1+\bar{C}) + 4\Big) + 2k^2\Big)\Big) \\
&+ j\sinh^2(j)\Big(\cot(\alpha)\Big(k^2(2+\bar{C}) - 2j^2\bar{C}\Big) + ik\Big(j^2\big(2 - \bar{C}k^2(1+\bar{C})\big) + \bar{C}k^2\Big)\Big) \\
&+ 2j\Big(j^2\cot(\alpha) + ik\Big(j^4(1+\bar{C})^2 + j^2\big(2+\bar{C} - k^2(1+\bar{C})^2\big) - k^2\Big)\Big)\Big),
\end{aligned} \tag{S13}
$$

$$
T_{UC}(k,l) = T_{UC\ num}(k,l)\ /\ T_{vel\ den}(k,l), \tag{S14}
$$

$$
\begin{aligned}
T_{VC\ num}(k,l) =& -kl\bar{C}\Big(\sinh(j)\cosh(j)\Big(ik\Big(j^2(2+\bar{C})(1+\bar{C}) - 2\Big) - j^2\bar{C}\cot(\alpha)\Big) \\
&+ \sinh^2(j)\Big(ikj\bar{C}\Big(j^2(1+\bar{C}) - 1\Big) - \cot(\alpha)\Big(2+\bar{C}\Big)\Big) + 2ijk\Big(j^2(1+\bar{C})^2 + 1\Big)\Big),
\end{aligned} \tag{S15}
$$

$$
T_{VC}(k,l) = T_{VC\ num}(k,l)\ /\ T_{vel\ den}(k,l). \tag{S16}
$$

The mathematical form of the shallow-ice-stream approximation version (Gudmundsson 2008, (*65*)) can be found in the supplement to Ockenden et al. (2023) (*21*). The python code to calculate these transfer functions can be found in the files transferfuncs2008.py and transferfuncs2003.py.

Applying Ice Flow Perturbation Analysis: A single isolated patch

For a square grid with grid coordinates x and y, we need ice-surface elevation $s(x, y)$, ice-surface velocities in the x and y direction $u(x, y)$ and $v(x, y)$ respectively, and a mean ice thickness $\bar{h}$. The dimensions of the grid (*square_size*) need to be several times larger than the ice thickness, so that perturbations within that region represent local processes and not far-field stresses. However, it should be sufficiently small that the assumption of planar flow within an inclined slab still holds. To calculate the bed properties using IFPA, these steps are followed:

1. **Ice flow direction**

   The mean ice-flow direction is calculated.

2. **Subtraction of a reference planar slab**

   From the interpolated ice-surface elevation and velocity, a reference slab inclined in the direction of ice flow is calculated. This slab has angle of slope α. The sloped surface of the reference slab is subtracted from the elevation data, and the mean ice-velocity is subtracted from $u(x, y)$ and $v(x, y)$, leaving only perturbations from the reference slab.

3. **Non-dimensionalisation**

   Elevations are non-dimensionalised with the scaling factor equal to the mean ice thickness of the reference planar slab, $\bar{h}$. Velocities are non-dimensionalised with the scaling factor equal to the mean ice velocity.

4. **Fourier transform**

   After applying a simple tapering function to avoid edge effects over a specified fraction of the grid (*tapering*), the non-dimensionalised ice-surface elevation and velocities are Fourier transformed to give $\hat{S}(k', l')$, $\hat{U}(k', l')$ and $\hat{V}(k', l')$, where k' and l' are the wavenumbers aligned with the x and y coordinates of the antarctic polar stereographic grid respectively.

5. **Calculation of wavenumbers aligned to ice flow**

   To calculate the IFPA transfer functions we need to know the surface conditions relative to the wavenumbers k and l, aligned with the ice flow and perpendicular to the ice flow respectively. This is a simple rotation operation, for which we use trigonometry to calculate k

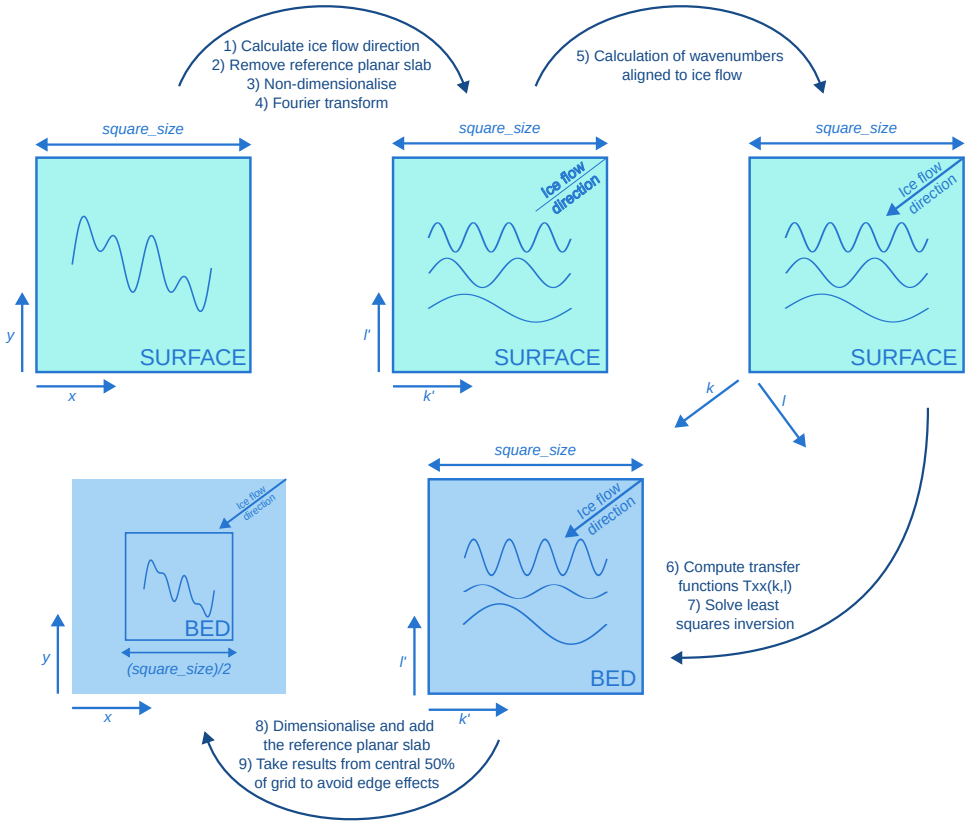

Figure S1: **Steps in the Ice Flow Perturbation Analysis methodology.** A schematic illustrating the order in which various steps are carried out when IFPA is applied to a single patch. Step numbers correspond to the description in the text.

and l from k', l' and the ice flow direction, giving us $\hat{S}(k,l)$, $\hat{U}(k,l)$ and $\hat{V}(k,l)$. In previous iterations of the IFPA methodology, this step was avoided by interpolating the data onto a grid aligned with the flow direction. This new method is mathematically equivalent, and much more computationally efficient.

6. **Computing the Transfer functions**

The transfer functions $T_{SB}(k,l)$, $T_{SC}(k,l)$, $T_{UB}(k,l)$, $T_{UC}(k,l)$, $T_{VB}(k,l)$ and $T_{VC}(k,l)$, are calculated using either the full-Stokes flow (2003) or shallow-ice-stream approximation equations (2008) depending on which is most suitable. For topography which will be applied in a shallow-ice-stream model we recommend the shallow-ice-stream equations. Due to their more complex form, the full-Stokes flow transfer functions take approximately twice as long

to compute.

7. **Least squares inversion**

   Equations S1, S2 and S3 can be solved to give $\hat{B}(k,l)$ and $\hat{C}(k,l)$ using a weighted least squares inversion, for each combination of k and l, following the method of Thorsteinsson et al. (2003) (*66*) and Appendix C of Ockenden et al. (2022) (*20*). To balance the relative sizes of the perturbations in velocity and elevation in the least squares equation, we apply a weighting factor er (also referred to as $\sum_S$). To suppress artificial amplification of small wavelengths which fall within the null space of the inversion, we use filtering parameters p and $wavcut$, to reduce small wavelengths. Landforms aligned to ice flow also fall in the null space of the inversion and are removed using the directional parameters, cut.

8. **Dimensionalisation and adding the reference planar slab**

   The resulting non-dimensionalised topography, $\hat{B}(k',l')$, and slipperiness, $\hat{C}(k',l')$, are inverse Fourier transformed, and then re-dimensionalised. Elevations are dimensionalised with the scaling factor equal to the mean ice thickness of the reference planar slab, $\bar{h}$. Slipperiness is dimensionalised with the scaling factor equal to the mean dimensional slipperiness, $\bar{c}$. The dimensionalised topography is positioned vertically by adding the mean surface elevation $\bar{s}$ and the slope of the reference planar slab, and subtracting the mean ice thickness $\bar{h}$.

9. **Results**

   This process calculates the bed topography, $b(x,y)$, and bed slipperiness, $c(x,y)$ on the polar stereographic grid. Only the central part of the original grid is used to avoid edge effects, and ensure and that areas smoothed during tapering are also cropped. For $tapering = 0.1$, we use the central 50% of the original grid.

This process is illustrated schematically in Figure S1, and can be carried out in python using the function bed_conditions_clean from the package inversion_module_v3.py.

Applying Ice Flow Perturbation Analysis: Larger areas

To apply the IFPA methodology over a wider area, we use multiple patches (dimension *square_size x square_size*), which overlap, such that every grid cell is included in n x n different patches (Here

n = 3, so each grid point is included in 9 different patches). Each of these individual patches is detrended using a planar trend. If we were to simply take the mean over the 9 overlapping patches, then the resulting DEM would have small, but noticeable, edge effects from the patches, because the planar trend for each patch is not exactly the same (although it is normally very similar) (*20*). However, we apply a weighted average, using a sinusoidal function for the weighting, such that in the centre of a patch, it is weighted 1, and at the edges it is weighted 0, removing edge effects and leading to a smooth final product. In the code for the inversion, the number of overlapping patches used in each region is specified with the parameter n, and the number of adjacent patches to be calculated in the x and y directions is specified with the parameter adj. We also report the weighted standard deviation of the overlapping patches, which can be considered as a proxy for the suitability of some of the assumptions in the IFPA method, in particular the assumption of small perturbations to planar flow in a uniform inclined slab.

This process is illustrated schematically in Figure S2, and can be carried out in python using the function terminal_inversion_smooth from the package inversion_module_v2.py. A worked example of applying the IFPA method to data from Antarctica is provided in the Jupyter Notebook Antarctic_IFPA_worked_example.ipynb, beginning with the application of IFPA to a single region specified by the user, and then illustrating how multiple single patches are combined to produce bed topography for a large region.

Applying Ice Flow Perturbation Analysis: The whole of Antarctica

A list of coordinates was prepared with 50 km spacing in the x and y directions on the polar stereographic grid. Coordinates were saved if they fell within the Antarctic continent, did not contain any null values in the surface elevation and velocity data, and if they had a mean surface elevation of more than 250 m. Coordinates with a lower mean surface elevation were assumed to be too close to the grounding line, where the physical processes are not captured in the linearised equations used in IFPA. Message Passing Interface (MPI) was used to parallelise the running of the IFPA code over this list of coordinates on the University of Edinburgh linux servers. We used the Gapless REMA digital elevation model (*24*), and the MEaSURES Antarctic ice velocity product (*23*). Previous versions of IFPA in Antarctica have used the NASA ITS_LIVE velocity product (*67*), but we have switched to using the MEaSURES velocity product to reduce artefacts

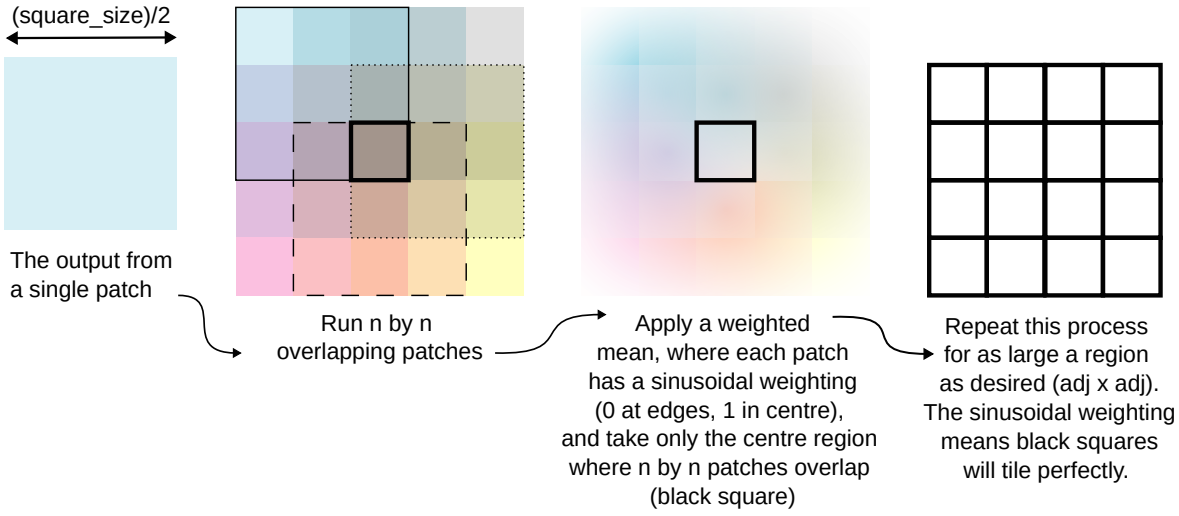

Figure S2: **Combining multiple patches across a domain.** A schematic diagram to illustrate the steps taken when combining multiple overlapping patches to produce a smooth data product over a larger area.

(see Supplementary Text, Artefacts from surface elevation and velocity).

The following parameters were used, where an asterisk (*) indicates values chosen because they returned reasonable amplitude features in previous work on Thwaites Glacier (*20*) and Pine Island Glacier (*21*):

- **Tapering parameter*:** $tapering = 0.1$

  The percentage of the grid (on each edge) which is subject to tapering to prepare for the Fourier transform.

- **Sliding exponent*:** $m = 1$

  Glaciological sliding exponent. Must be set to 1 for the full Stokes equations, can be varied for the shallow-ice-shelf equations (see (*64, 65*).)

- **Wavelength filtering parameters*:** $p = -2$, $wavcutB = 1$, $wavcutC = 2$

  p is a parameter which removes problematic short wavelengths from the IFPA inversion to avoid infinite amplification of small wavelengths (see (*20*)). *wavcutB* and *wavcutC* are additionally wavelength filtering parameters for the topography and slipperiness respectively, which are set as multiples of the ice thickness, h, to ensure that the IFPA topography does not

incorrectly show landforms smaller than the ice thickness which can not mathematically be resolved. Any features smaller than the ice thickness which are removed are likely artefacts.

- **Weighting factor*:** $er = 10^{-3}$

  To ensure a good balance in the least squares solution between elevation perturbations (order 0.001) and velocity perturbations (order 1), we provide a weighting factor for the velocity data.

- **Mean non-dimensional slipperiness*:** $\bar{C} = 50$

  The effect of varying $\bar{C}$ was explored in Ockenden et al. (2023) (*21*). A value of $\bar{C} = 50$ was chosen to better reflect variability in the slower flowing interior regions, where we expect the IFPA method to be the most useful. Note that slipperiness is not expected to be constant across Antarctica, but there are very few observation data with which to constrain it, so we use a constant value.

- **Directional filtering parameters:** $cutB = 10$ and $cutC = 15$

  The angle (in degrees) from the flow direction at which variability in the basal conditions, which falls into the null space of the inversion, is removed.

- **Patch dimensions:** $square\_size = 50000$

  The dimensions of the grid ($square\_size$) need to be several times larger than the ice thickness, so that perturbations within that region represent local processes and not far-field stresses. However, it should be sufficiently small that the assumption of planar flow within an inclined slab still holds. For this reason, we settle on dimensions of 50 km, covering multiple ice thicknesses even in the deepest regions of Antarctica. However, it would definitely be possible to use a smaller dimension, particularly in mountainous regions with thinner ice, to better capture the local ice behaviour.

- **Number of overlapping grids:** $n = 3$

  See Figure S2.

- **Number of adjacent grids:** $adj = [6, 6]$

  Note that a larger value of adj would reduce the grid spacing required in the list of coordinates,

and reduce run time by lowering the number of repeat calculations between neighbouring patches. We used a value of 6 to keep memory usage low, as all adjacent patches are kept in memory simultaneously until the results are saved.

- **Transfer functions:** Full-Stokes flow transfer functions (2003 equations)
  Either the full-Stokes flow (2003) or shallow-ice-stream approximation equations (2008) depending on which is most suitable. For topography which will be applied in a shallow-ice-stream model we recommend the shallow-ice-stream equations. Due to their more complex form, the full-Stokes flow transfer functions take approximately twice as long to compute. See (*21*) or (*68*) for a discussion of the differences between these transfer functions.

- **Mean ice thickness:** $\bar{h}$
  For each patch, initial estimates of the mean ice-thickness are derived from BedMachine Antarctica v3 (*13*). In previous iterations of IFPA, we used a 50 km neighbourhood for this baseline ice thickness, which illustrated the potential of the method to resolve topography without needing ice-thickness observations. In order to better incorporate the existing observations we now use a 8.3 km neighbourhood, which matches the dimensions of the central region of the overlapping tiles ($square\_size/2n$). Figure S3 illustrates how little topographic information is provided to the inversion by this mean ice thickness for these parameters, and the impact of this methodological change.

A total of 4269 patches of bed topography, each 50 km by 50 km, were analysed. This process was carried out in python using the script mpi_inversion.py. As a result of the weighted mean procedure used when applying IFPA over larger areas, these patches could then be smoothly joined together without edge effects to create a map of topography across the whole of Antarctica. This joining process was carried out in python using the script Stitching.py.

The IFPA method allows us to invert for both topography and non-topographic bed conditions (in the form of basal slipperiness), as explored in (*21*). However, we do not present slipperiness results here due to a lack of data with which to constrain slipperiness. Improved observations of subglacial hydrology, geology, sediment distribution and other factors expressed in models through friction would allow for better constraints on the inverted slipperiness field.

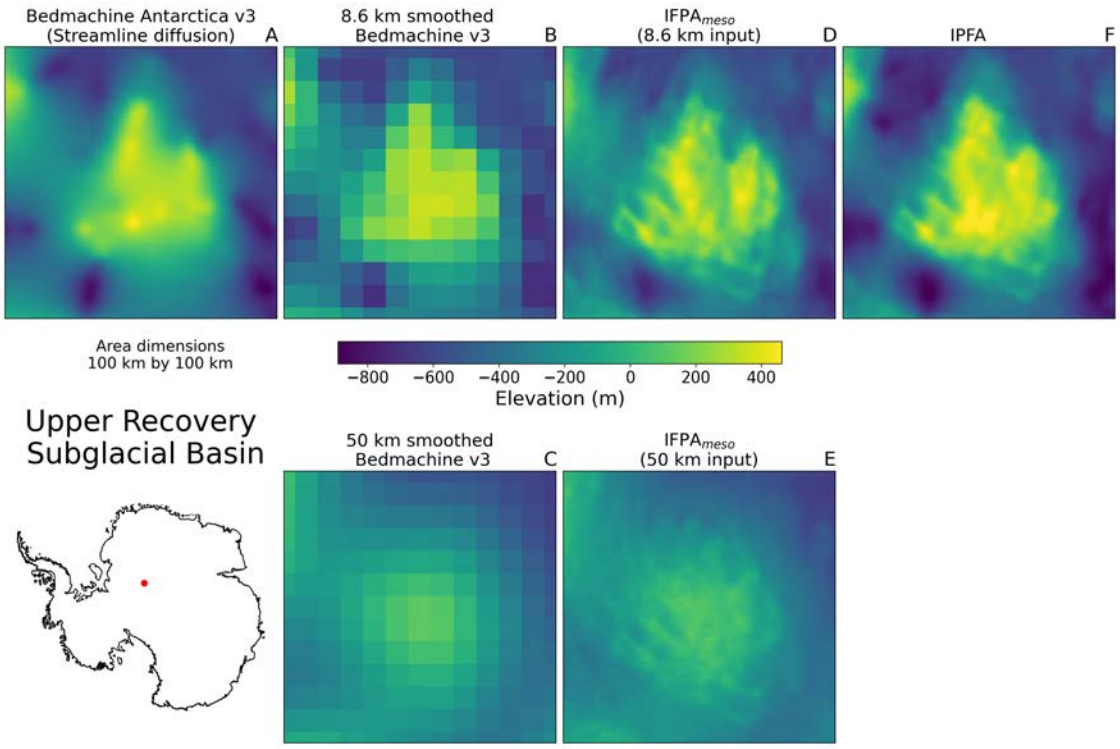

Figure S3: **The influence of smoothing the reference baseline bed topography to 50km or 8.6km averages on the output from the IFPA method.** A comparison for part of the Upper Recovery Subglacial Basin of (A) bed topography from BedMachine Antarctica v3 (*13*), with (B) an 8.6 km mean (to match the central area of the overlapping grids) and (C) a 50 km mean (used in previous iterations of IFPA); and the resulting bed topography produced by applying IFPA$_{meso}$ with (D) the 8.6 km mean topography and (E) the 50 km mean topography as a baseline. In panel (F) the IFPA bed topography has been derived with a final correction to elevations based on all the available ice-thickness observations. In panels (B) and (C), each individual square pixel is 8.6 km square ($square\_size/2n$).

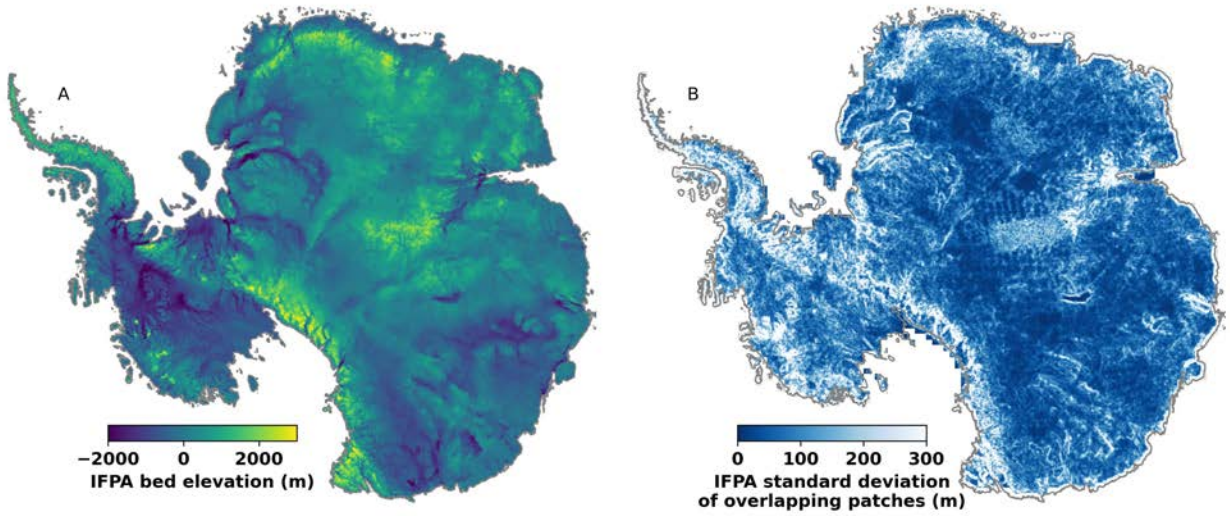

Figure S4: **A proxy for uncertainty in the IFPA method: The standard deviation of overlapping patches.** A) The IFPA bed topography (repeated from Figure 1), and B) the standard deviation of overlapping patches from the IFPA method. Although not a true error measurement for the IFPA method, the standard deviation of overlapping patches gives an indication of regions where the assumptions behind the method are not valid, particularly the assumption of planar flow in a slightly inclined slab - for example in mountainous terrain with steep slopes, where the standard deviation is high (light blue/white). Note that the color scale is capped at 300 m.

We do, however, provide the weighted standard deviation of the 9 overlapping patches at each point (Figure S4). To apply the IFPA method, we assume that the ice flow can be approximated by planar flow in an inclined slab, and that small perturbations to the base of the slab cause perturbations in the ice surface. In regions where the ice flow can reasonably be approximated in this way, we expect that the reference slabs for each overlapping patch will be similar, and the resulting topographies will have a low standard deviation. In regions where this assumption about the ice flow does not hold, the standard deviation of the resulting topographies will be higher. We expect this to be the case in regions where the topography has steep slopes and sharp transitions, for example in mountainous areas and in steep sided glacial troughs (e.g. the Transantarctic Mountains and the Denman Glacier trough). These tend to be regions where other methods, such as mass conservation, perform well. We expect the IFPA method to work best in areas where the topographic variability is relatively small compared to the ice thickness, for example in wide glacial basins and the continental interior (e.g. Thwaites Glacier, Wilkes Basin, Aurora Basin).

Re-calibrating IFPA with radar data

Our initial map, produced using the steps detailed above and henceforth referred to as IFPA_{meso}, captures the overall roughness and mesoscale features well. However, due to uncertainties in the baseline ice thickness and in the basal slipperiness applied, it suffers from offsets of 100s of m in some places. To remedy this problem, we produce a correction map that is added to the initial map in order to match the long scale depth from the radar data. We do this by interpolating our calculated ice thickness onto all available radar lines and subtracting it from the radar-inferred ice thickness. Ice-thickness measurements come from the Bedmap3 compilation (*7*), and from Open Polar Radar (*69*)(https://data.cresis.ku.edu/data/rds/). This process provides corrections along flight lines. These corrections are then extrapolated using a streamline-diffusion algorithm, following (*13*), in order to avoid kriging artefacts. This complete 2-dimensional correction map is then applied to the entire IFPA_{meso} map, to produce a map which contains the novel mesoscale details from the IFPA_{meso} map, but which is simulataneously consisent with all the available geophysical data. We refer to this radar corrected map simply as IFPA.

Figure S5 shows the effect of this correction along 2 ice-penetrating radar profiles from Highlands B and C and from the South Pole Basin. For Highlands B and C, where the ice-penetrating

radar survey observations had already been included in BedMachine v3 before IFPA was applied, both the IFPA$_{meso}$ and the radar-corrected IFPA map correspond well with the ice-penetrating radar surveys (Pearson correlation coefficient of 0.95 and 0.98 respectively). For the South Pole Basin, the radar observations were collected more recently than the BedMachine v3 map was compiled. In this region, the mean elevation of the IFPA$_{meso}$ map has the same offset from the ice penetrating radar as BedMachine v3, which was used as the baseline. However, the shape of the IFPA$_{meso}$ topography shows the same hills and valleys as the ice-penetrating radar profile, demonstrating that the IFPA method can reveal the mesoscale structure of the landscape even in regions with fewer ice-thickness measurements. For additional comparisons to ice-penetrating radar profiles, we refer the reader to (*20, 21*), which present comparisons with the results of the IFPA methodology (albeit an older version) for Thwaites Glacier and Pine Island Glacier respectively.

We can further explore the robustness of the IFPA method by withholding radar data, applying the IFPA methodology, and then comparing the resulting bed topography to topography produced from the with-held radar data. Figure S6 illustrates this for two example regions: the Upper Thwaites Glacier region, explored further in (*20*), and Princess Elizabeth Land in East Antarctica. In the Thwaites Glacier region, we assume a constant ice thickness of 2000 m, giving a 'baseline topography' which is 2000 m below the ice surface. For Princess Elizabeth Land, we use BedMachine Antarctica v1 (*13*) as the baseline topography, representing a time before which the region had not yet been intensively surveyed. In both cases, the landscape features seen in the resulting IFPA$_{meso}$ bed topography can also be seen in the BedMachine v3 bed topography (*13*), which uses streamline diffusion to interpolate between radar survey lines (*7*). This demonstrates that the IFPA methodology reveals real topographic features which are also observed in ice-penetrating radar surveys, even when the ice-thickness information is withheld.

Landscape texture analysis

We calculate a range of textural and spectral metrics for the following bed topography maps: 1) Ice Flow Perturbation Analysis (IFPA), 2) Ice Flow Perturbation Analysis without the re-calibration to radar data (IFPA$_{meso}$), 3) BedMachine Antarctica (*13*), and 4) Bedmap3 (*8*). These metrics are calculated for all 4269 regions, each 50 km by 50 km.

Metrics focused on the elevation distribution are the mean and the standard deviation with the

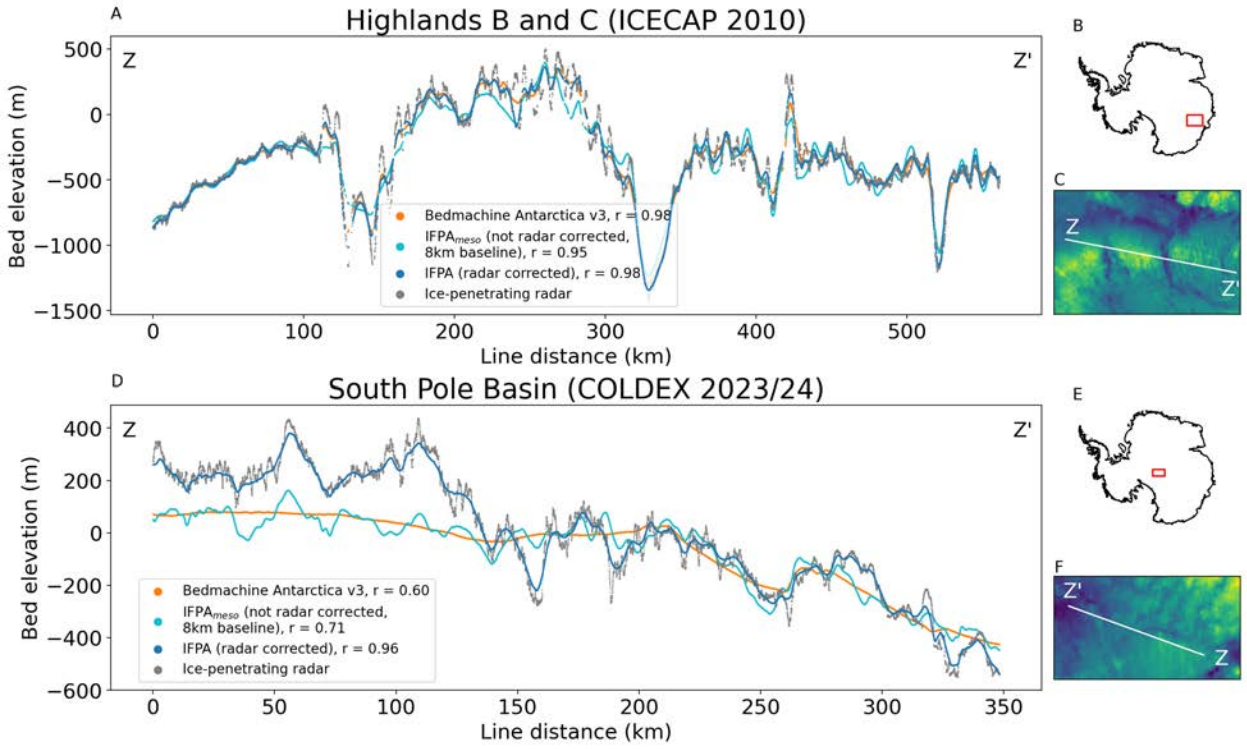

Figure S5: **IFPA reveals the mesoscale structure of the landscape even in regions with fewer ice-thickness measurements.** Panels A) Highlands B and C, and D) South Pole Basin show profiles of bed topography from BedMachine Antarctica v3 (*13*) (orange), the IFPA$_{meso}$ (light blue), IFPA (dark blue), and ice-penetrating radar observations of bed elevation (grey). The ice-penetrating radar profiles are from the UTIG 2010 ICECAP survey (Highlands B and C) (*7*), and the 2023/24 COLDEX survey (South Pole Basin). The Pearson correlation coefficient is given for a comparison between the ice-penetrating radar profiles and the different topographies. Panels B) and E) show survey-track locations, and panels C) and F) show the local topography, for Highlands B and C and the South Pole Basin respectively. The South Pole Basin line showcases how strongly IFPA performs in regions where there is no ice-penetrating radar data, as crucially the IFPA$_{meso}$ topography (derived with no calibration to the location of geophysical measurements) captures the frequency of hills and valleys which were later surveyed by COLDEX ice-radar profiling.

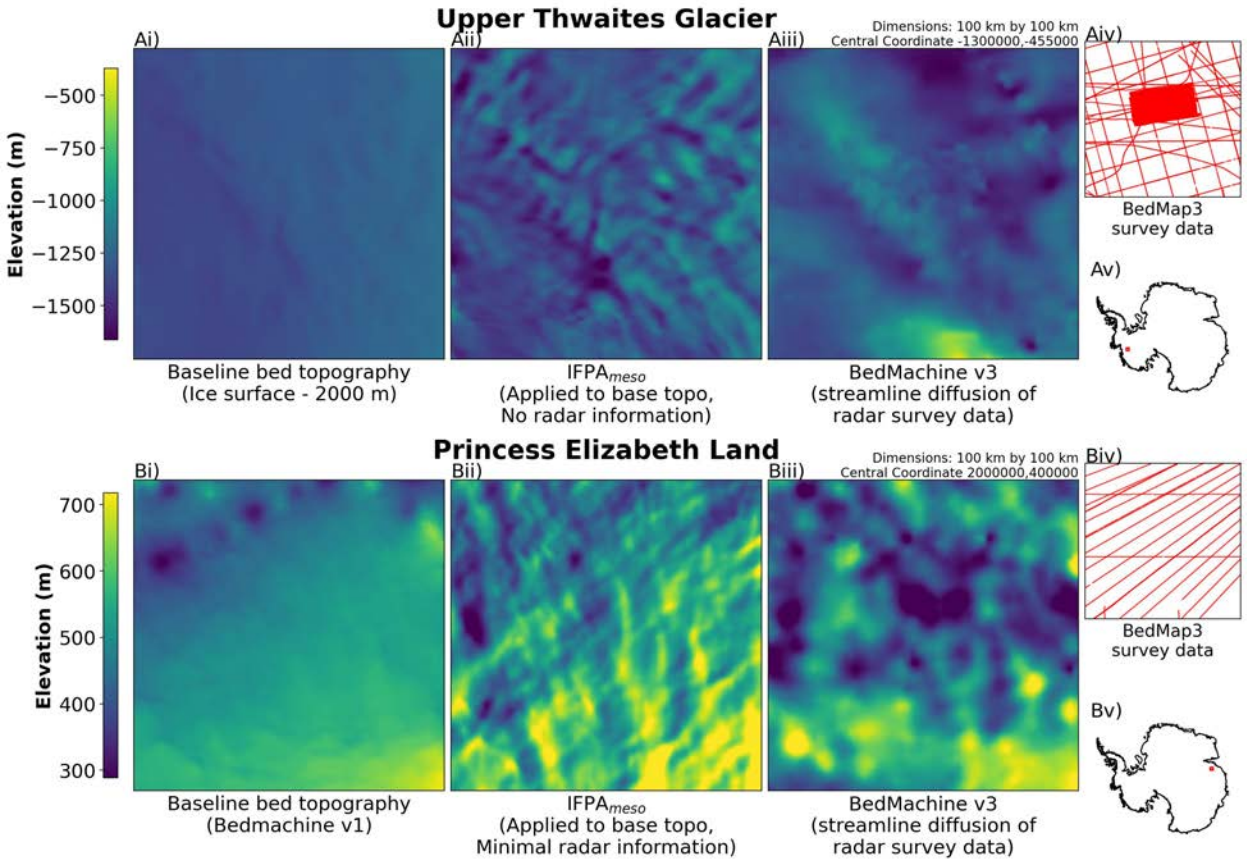

Figure S6: **Even without ice-thickness information, IFPA$_{meso}$ maps real topographic features, as seen in geophysical surveys.** For A) the Upper Thwaites Glacier region, and B) part of Princess Elizabeth Land, a comparison of i) a baseline bed topography with minimal ice-thickness information from geophysical surveys (a single ice thickness value of 2000 m for Upper Thwaites Glacier, the BedMachine v1 bed topography for Princess Elizabeth Land), ii) the bed topography when IFPA is applied with this baseline bed topography, iii) bed topography produced by streamline diffusion between geophysical surveys (from BedMachine Antarctica v3). Panels iv) and v) show the location of geophysical survey observations in the Bedmap3 compilation (*7*) in the region shown, and the location of the region within Antarctica respectively.

local mean slope removed. To characterise the texture, we also calculated the RMS slope and RMS curvature. The Fourier transform of the elevation reveals the spatial frequency spectrum, and we calculated its fractal dimension, and the wavelength of the strongest power component. Since we expect IFPA to contribute new topography mainly at short wavelengths, we also applied high and low frequency band-pass filters to the topography, and calculated the standard deviation and RMS slope for the band-pass filtered topography. Another way to look at the new topography at short wavelengths is to count local maxima (or minima), and we counted peaks with amplitudes of 20 m, 50 m, 100 m and 250 m in a 5 km radius.

The following metrics were calculated:

- **Mean elevation**

- **Standard deviation with the slope removed**

  We calculate the best fit plane to the bed topography DEM, and then subtract this from the DEM. This is a simple way to remove the long wavelength topography, and to see roughness from the short wavelength landforms.

- **RMS slope**

  The root mean square of the first derivative of the bed topography. All derivatives were calculated using the np.gradient function.

- **RMS curvature**

  The root mean square of the second derivative.

- **Low and High frequency Standard deviation**

  We use the skimage.filters.difference_of_gaussians function to band-pass filter the bed topography for High and Low wavelengths with $\sigma = 4$, and $\sigma = 80$, respectively. The standard deviation was calculated for each of these band-pass filtered topographies.

- **Low and high frequency RMS slope**

  The root mean square of the first derivative of the band-pass filtered topography.

- **Fractal dimension (> 5 km)**

  Fourier fractal dimension is a statistical measure of the level of detail in a surface, with a higher

fractal dimension indicating a more complex surface, or rougher subglacial topography. The Fourier fractal dimension of a surface (D_{ff}) can be calculated from (β), the gradient of the line of best fit to the Fourier power spectrum of the topography (*70, 71*).

$$D_{ff} = \frac{6+\beta}{2} \tag{S17}$$

We calculate the Fourier spectrum using the fast Fourier transform following Equation S18, with Hann windowing to reduce edge effects, in this case only for wavelengths greater than 5 km. The power spectral density is the square of the Fourier transform, corrected for grid spacing and windowing, as in Equation S19.

$$\hat{f}(k,l) = \sum_{x=0}^{N_x-1} \sum_{y=0}^{N_y-1} f(x,y)w(x,y)\ \exp\left(-2\pi i\left(\frac{kx}{N_x} + \frac{ly}{N_y}\right)\right) \tag{S18}$$

$$k = 0, ..., N_x - 1, l = 0, ..., N_y - 1$$

$$PSD(k,l) = \frac{|\ \hat{f}(k,l)\ |^2\ \Delta_x\Delta_y}{\sum_{x=0}^{N_x-1}\sum_{y=0}^{N_y-1} w(x,y)^2} \tag{S19}$$

where $w(x,y)$ is a Hann windowing function, k and l are the wavenumbers, and Δ_x and Δ_y are the grid spacings in the x and y directions.

- **Fractal dimension (for wavelengths > ice thickness)**

  The Fourier fractal dimension when only wavelengths greater than the ice thickness are considered, calculated as above.

- **Wavelength of maximum power**

  The Fourier power spectrum is wavelength normalized with comparison to the line of best fit to the Fourier power spectrum, and we take the wavelength with the highest normalized power.

- **The number of 20 m / 50 m / 100 m / 250 m hills in 5 km**

  Using the scipy.ndimage.filters.maximum_filter function, we count the number of grid cells which are the highest cell in their 5 km neighborhood and are at least 20 m/50 m/100 m/250 m higher than their lowest neighbor. This analysis was also done for minima instead of maxima, but yields almost identical results, so only the maxima are reported here. Figure S7 shows the

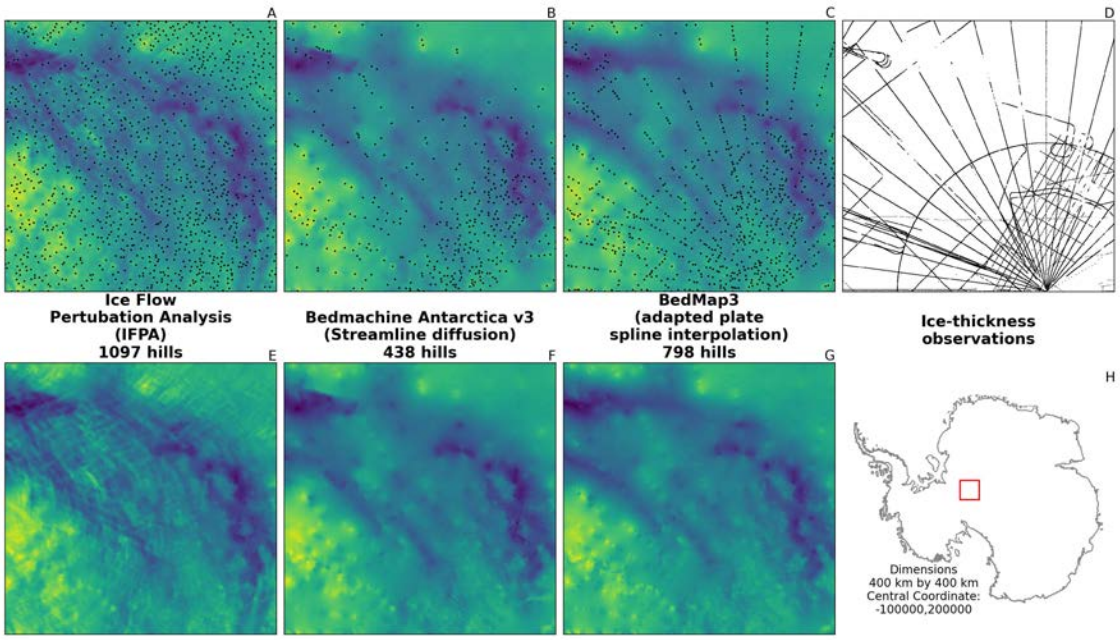

Figure S7: **50 m hills in a 5 km neighborhood in the Pensacola-Pole Basin for different topography maps.** For A) Bedmap3 (*8*), B) BedMachine Antarctica v3 (*13*) and C) the IFPA map, all points which are the highest cell in their 5 km neighborhood, and which are at least 50 m higher than their lowest 5 km neighborhood are marked by black dots. Panels E, F and G show the regional topography from the respective bed topography map. The ice-thickness observations in the region are shown in D), and the location of the region in Antarctica in H). The IFPA topography identifies hills in regions away from survey lines, whereas the pattern of hills in Bedmap3 is clearly influenced by the distribution of ice-thickness measurements.

locations of 50 m hills for IFPA, BedMachine Antarctica and Bedmap3 in the Pensacola Pole region. This also illustrates that roughness in the IFPA map is more uniformly distributed, whereas in interpolated maps the roughness is isotropic, and focused along geophysical survey lines.

These metrics can be calculated in python using the script metrics.py.

Geomorphological domain classification

Much of what is known about the subglacial topography of Antarctica is contextualised with reference to the deglaciated beds of former ice sheets in North America, Patagonia and Scan-

dinavia (*14, 72–74*). Early work by Sugden and John (1976) (*40*) classified exposed Antarctic marginal topography using a process-based geomorphological approach based on other deglaciated landscapes. Following the release of Bedmap2 (*60*), this classification was extended to the ice-covered parts of the continent by Jamieson et al. (2014) (*39*). Although our work builds upon these classifications, we divide topography into alpine, with sub-categories for subglacial (fully submerged) and subaerial (partially submerged), low-relief (previously termed "areal scour" (*39, 40*)) or selective erosion (previously termed "selective linear erosion"). In light of the improved spatially consistent understanding which our new map provides, we propose that these descriptions may more accurately reflect the subglacial landscape of Antarctica.

Using selected example regions of each topographic style, we leverage the textural and spectral characteristics of the topography to create a manual classification protocol, and to divide up 4629 regions of Antarctica, each 50 km by 50 km, into these categories. Regions with the distinctive properties of artefacts from undulating dunes in the ice surface are removed. For each of these categories, we identified three 150 km by 150 km regions of relevant topography from across Antarctica (Figure S8), giving nine 50 km by 50 km regions where the textural metrics were calculated for the IFPA_{meso} topography map. Figure S9 shows how these metrics vary for the different topographic styles.

We use metrics from the IFPA_{meso} map to give a more self-consistent picture of the subglacial landscape, and reduce the effect of uneven geophysical survey spacing. For this reason, the classification was done using metrics which do not include the absolute relief of the topography, instead focusing on relative amplitudes and textural metrics. There is undoubtedly further geomorphological analysis which can be carried out on the radar-corrected IFPA map. Additionally, we only used a very small sample of training data for the classification, and future geomorphological analyses could make better use of deglaciated landscapes for training data, alongside using more sophisticated classification algorithms, particularly given the increasing availability of machine-learning techniques for image classification problems.

For the simple classification used here, we begin with topographic types with very distinct and identifiable characteristics: low-relief landscapes and artefacts from dunes. Low-relief areas have notably smooth topography, and hence can be identified by low RMS curvature (< 0.025, Fig. S9a) and few hills of any prominence ($<$ 15 of 20 m height, Fig. S9b), as well as a low RMS slope for

the high frequency (σ = 4 for the difference of Gaussians) component of the topography (< 0.07, Fig. S9c). Areas with artefacts from dunes in the ice surface are dominated by small-amplitude and high-frequency landforms, with very few 100 m high hills in a 5 km radius (= 0, Fig. S9e), and a low dominant wavelength (< 5 km, Fig. S9e). Their texture is also distinctive, combining low RMS slope (< 0.9, Fig. S9a) and high RMS curvature (RMS slope/RMS curvature < 14.75, Fig. S9a).

Subaerial alpine topography can be distinguished by high relief, but also by high RMS slope for the high frequency component of the topography (> 2, Fig. S9d) and a large number of 250 m high hills in a 5 km radius (> 10, Fig. S9d). Subglacial alpine topography is not as easy to distinguish as subaerial alpine topography, due to the thicker ice reducing the imprint of buried mountains in the ice surface. However, their distinctive branching-tendril texture means that these regions can be distinguished from lower topography due to a moderate RMS slope (< 1.1, Fig. S9a) and a moderate Fourier fractal dimension (> 0.5, Fig. S9b). We also classify high elevation regions (> 1000 m) with high standard deviation at low frequencies (> 19) as subglacial alpine topography.

Following Sugden and John (1976) (*40*) and Jamieson et al. (2014) (*39*), we classify anything which is not definitely within one of these categories as other selective erosion. However, we also identify a sub-class of selective linear erosion topography with a distinctive pattern of many individual topographic bumps not connected by ridges, which is spatially distributed around modern day ice streams. These regions have a high RMS slope (> 1.0, Fig. S9a) and low Fourier fractal dimension (< 0.25, Fig. S9b). Due to their geographical location, we propose that this subclass represents active ice stream processes, and that the remainder of the selective erosion class represents a relict landscape.

This geomorphological classification utilised the radar-uncorrected IFPA bed topography to give a self-consistent spatial picture of the subglacial landscape of Antarctica. For this reason, the classification was done using metrics which do not include the absolute relief of the topography, instead focusing on relative amplitudes and textural metrics. There is undoubtedly further geomorphological analysis which can be carried out on the radar-corrected IFPA map. Additionally, we only used a very small sample of training data for the classification, and future geomorphological analyses could make better use of deglaciated landscapes for training data, alongside using more sophisticated classification algorithms, particularly given the increasing availability of machine-learning techniques for image classification problems.

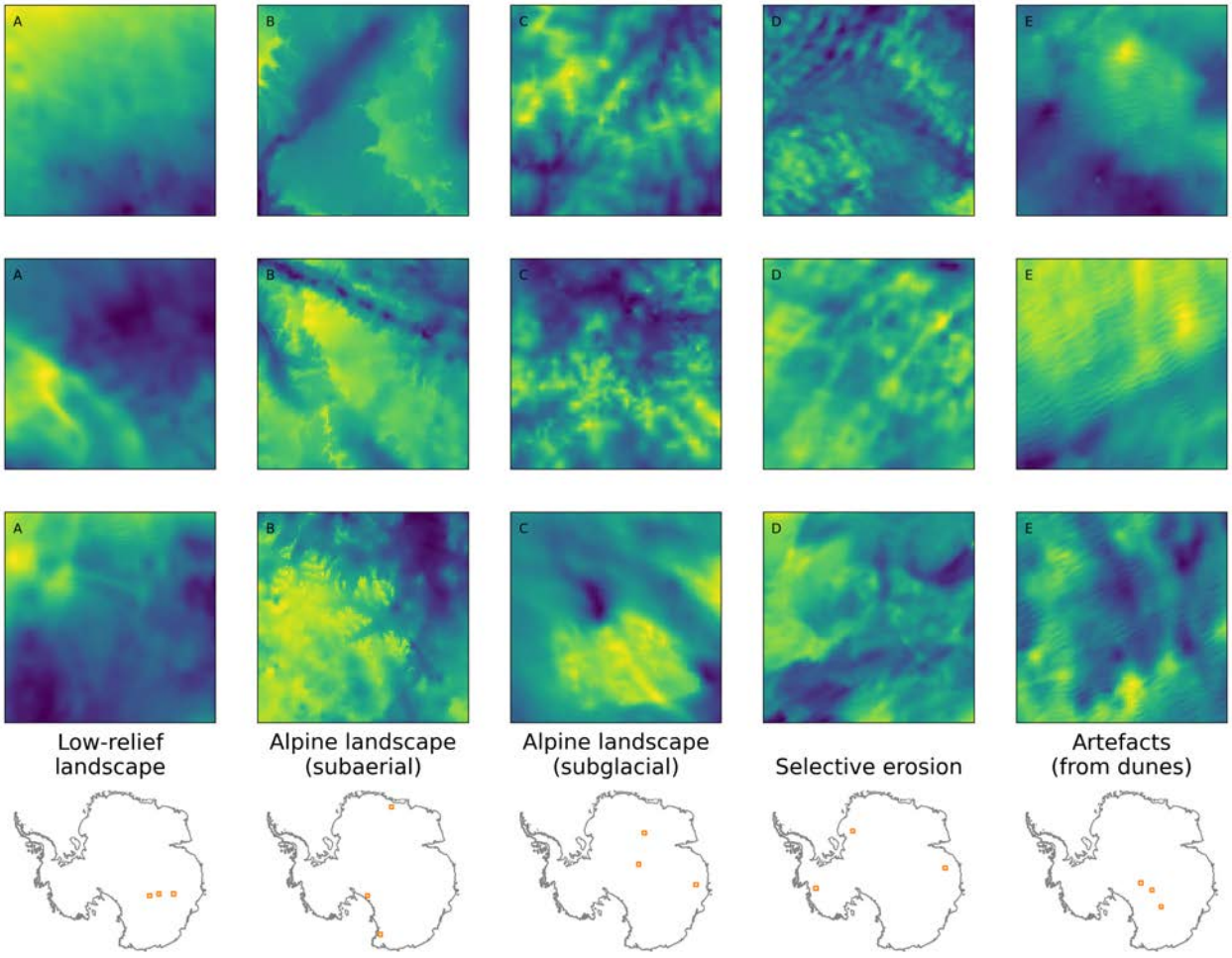

Figure S8: **Examples regions with different topographic styles.** 150 km by 150 km topographic patches from IFPA for A) areal scour, B) alpine (subglacial), C) alpine (aerial), D) selective linear erosion in ice streams and E) artefacts caused by dunes in the ice surface. The locations of the chosen topographic patches are shown on the maps at the bottom of each column.

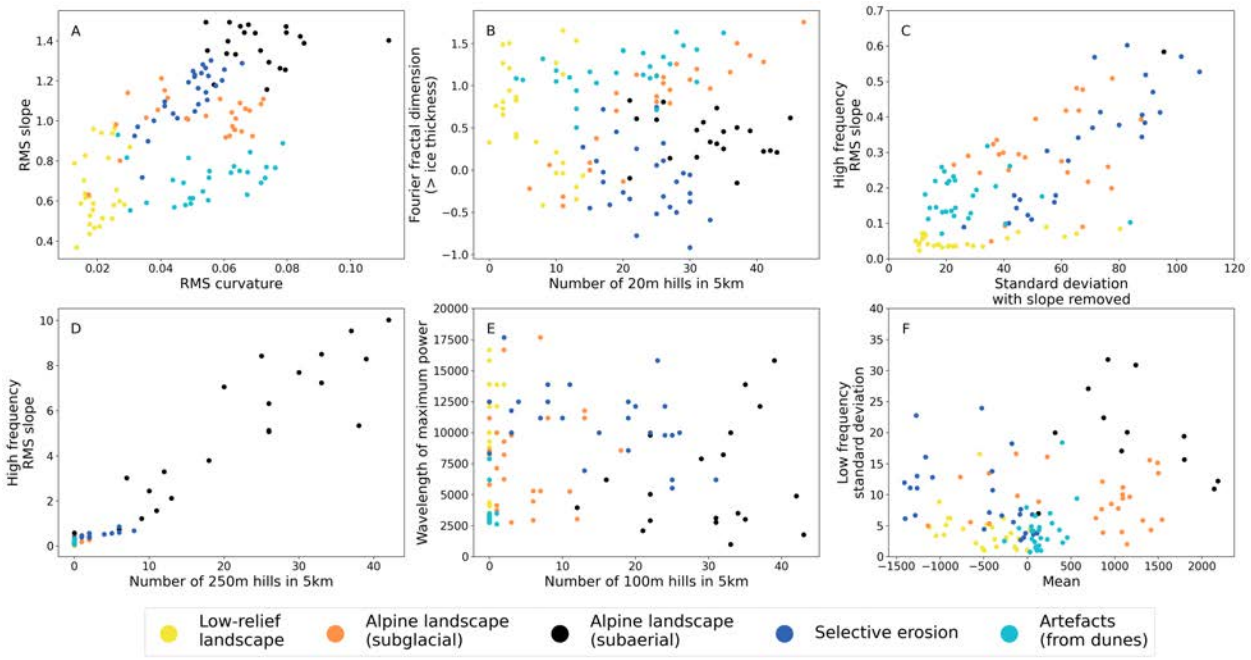

Figure S9: **Textural and spectral characteristics of different topographic styles.** Eleven textural and spectral characteristics plotted for the example regions for five classes of subglacial topography (areal scour in yellow, alpine (subglacial) in orange, alpine (aerial) in black, selective linear erosion (SLE) in ice streams in dark blue and artefacts from dunes in light blue). Note that the axis scales for panel C) have been chosen to show the variability between regions of areal scour and regions with artefacts from dunes, and so most data points for alpine (aerial) fall outside of the chosen region.

Supplementary Text

Which features can Ice Flow Perturbation Analysis resolve?

Ockenden *et al.* (*20*) carried out an extensive study using synthetic data of the features which can and can not be inverted using Ice Flow Perturbation Analysis. Features can be resolved at the bed if they have a horizontal amplitude which is greater than the ice thickness in that region, and a vertical amplitude greater than ~0.005 x of the ice thickness (assuming errors of ±2 m in the surface data (*22*) and ±15 ms^{-1} in the velocity data (*67*)). In Antarctica, this translates to roughly 2 km horizontal and 10 m vertical as the minimum bounds for features resolvable using IFPA. We apply a wavelength filter ($wavcutB$ = 1) to remove features smaller than the ice thickness in the IFPA topography. Since, the IFPA perturbation analysis method looks at local perturbations from the long-wavelength background state, and we apply the method here to small patches ($square\_size$ = 50 km), the largest possible local perturbations that IFPA can resolve are roughly 30 km. We describe the wavelength range of features resolvable using IFPA (2-30 km) as mesoscale topographic variability.

Additionally, synthetic tests show that landforms can only be resolved if they are not aligned to the flow direction (*20*). When studying subglacial environments with IFPA, this is not a huge concern because the most common landforms aligned to flow are MSGL, which have a horizontal wavelength less than the ice thickness, and which we would not expect to resolve. Additionally, along-flow bedforms are normally produced by ice flow, rather than being controls on ice flow, and are less important for ice-sheet models. However, due to this null space in the inversion, surface features aligned to the ice flow can produce artefacts in the basal topography. We apply a directional filter during the IFPA inversion process ($cutB$ = 10) to remove these artefacts. However, in some regions this directional filtering process can lead to some cross hatched textures which are connected to the method and not the bed topography.

Previous work has also explored the role of the mean non-dimensional slipperiness parameter ($\bar{C}$) (*20,21*). Although the amplitude of features increases as $\bar{C}$ decreases, the position and geometry of features does not change. A value of $\bar{C}$ = 50 was chosen for this work to better reflect variability in the slower flowing interior regions, where we expect the IFPA method to be the most useful. Additionally, we apply the post-processing correction which aligns the $IFPA_{meso}$ topography with

all available ice-penetrating radar survey lines to produce the corrected IFPA map. This correction helps to account for the uncertainty in the amplitude of features due to the lack of constraints on the most appropriate value of $\bar{C}$.

During this post-processing correction, we use all the available radar data, including some data from before 1980 which has very uncertain spatial coordinates due to the lack of concurrent GPS measurements. In some regions, these pre-GPS observations cause bulls-eye artefacts in the IFPA map which are not present in the IFPA$_{meso}$ map (e.g. Figure S28.36). However, we continue to include these observations because the radar information is still valuable in these regions even if the positioning is not certain, and because in some regions these are the only data available.

Artefacts from surface elevation and velocity

IFPA assumes that all topography in the ice surface occurs as a result of ice flow over bed perturbations. However, in some regions, surface processes can also create topography. The regular periodic waves of megadunes produced by katabatic winds on the East Antarctic plateau (*75*) are a good example of this, and we see the imprint of these landforms in the IFPA bed topography (Figure S10a). Artefacts in the bed can also be produced when there are artefacts in the input data sets. In the South Pole Basin region, the ITS_LIVE velocity product contains many linear features which closely follow lines of latitude, forming curves centered on the pole (*67*) (Figure S10b), and these linear features are also present in the IFPA bed topography if this data set is used. For this reason, we have applied IFPA across Antarctica using the MEaSURES phase-based ice velocity product (*23*), which does not suffer from these artefacts. To aid future users of the IFPA bed topography, we do however, identify regions which are potentially influenced by artefacts in the extended figures in the appendix.

Although these two types of artefacts can be detected, and only cover a small proportion of the total mapped region, other surface processes or randomly distributed data artefacts may be present which are harder to identify and remove. As new techniques for processing satellite observations are developed and become more standardised, gridded velocity products will contain fewer artefacts, so the application of IFPA to future datasets may reveal new features which are currently obscured. Applying the IFPA methodology to different datasets for the ice-surface elevation and velocity would also allow for consistent features to be identified and distinguished from transient features

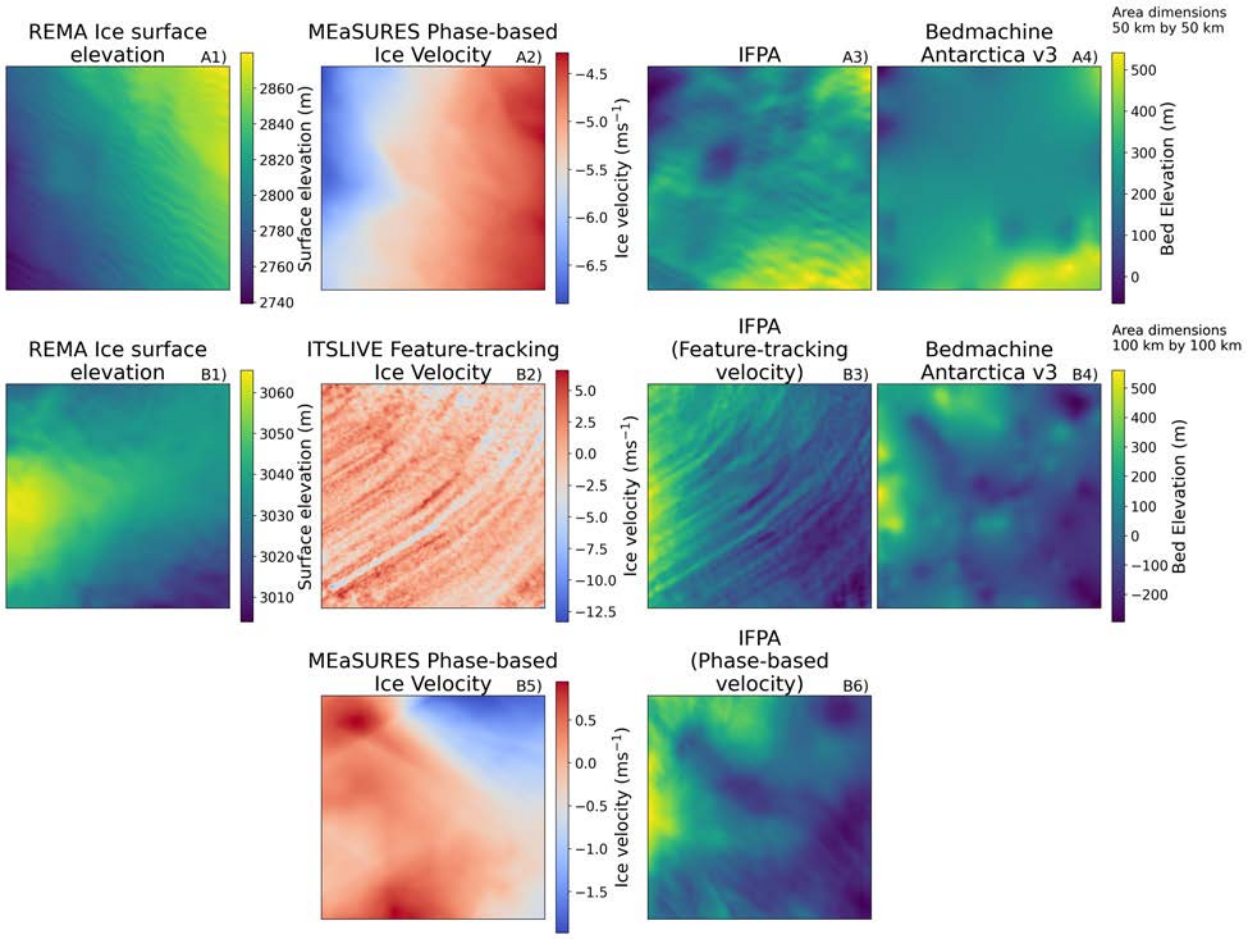

Figure S10: **Examples of artefacts in the IFPA topography from surface data sets.** Subglacial topography produced from IFPA can have artefacts produced by A) features in the ice surface which are not produced by ice-flow processes, in this case megadunes formed by katabatic winds, and B) artefacts in the surface data, in this case velocity artefacts caused by proximity to the South Pole. Panels show the ice-surface elevation (*22, 24*) (A1 and B1), the ice-surface velocity from either the MEaSURES phase-based velocity product (*23*) (A2 and B6) or the ITS_LIVE feature-tracking velocity product (*67*) (B2), the resulting IFPA bed topography (a3,b3,b6), and the bed topography from from BedMachine Antarctica v3 (*13*). For the region shown in panels B), artefacts in the ITS_LIVE velocity product (B1) led to artefacts in the IFPA topography (B3). Using the MEaSURES phase-based velocity product (B5) which does not contain these artefacts leads to IFPA bed topography (B6) which matches the topography seen in BedMachine Antarctica v3, illustrating how some artefacts may be removed with the application of different surface datasets.

caused by artefacts, as we did when we switched from the ITS_LIVE velocity product (*67*) to the MEaSURES velocity product (*23*).

The IFPA method assumes that the ice flow is in equilibrium, and that signals from all the basal features have had time to propagate to the ice surface (*20, 21, 68*). However, in many regions of Antarctica, there is active erosion happening beneath the ice sheets (*76–78*), offering the possibility that the application of paired velocity and elevation data might allow us to identify regions where erosion has occurred. However, due to the short temporal length of satellite observations, and the amount of time required for basal evolution on mesoscale wavelengths, it is unlikely that we would be able to identify signatures of changes in the bed topography in the ice surface without paired data spanning centuries.

Where are the physical assumptions of the IFPA method not applicable?

Since IFPA makes the assumption of planar flow in an inclined slab, we do not expect IFPA to give the best results in regions where there are significant changes in the local basal slope, especially in mountainous regions where the ice-cover is thin and there are nunataks above the ice. In the TransAntarctic Mountains (Figure S13.5), the Sør Rondane Mountains (Figure S21.21), and around the coast of Marie Byrd Land (Figure S12.3), we see that steep slopes and mountain ridges create a spindly texture in the IFPA_{meso} topography that is not really representative of the bed. The IFPA map, with its radar correction, does not contain these artefacts.

Additionally, the IFPA method assumes that variability in the elevation of the bed is transferred to the ice surface by flowing ice. In regions with extremely slow flowing ice, the surface may not be in equilibrium with the bed. In these regions, such as central Kemp land (Figure S28.36), the Northern Recovery Subglacial Highlands (Figure S20.19a) and to the east of the Gamburtsev Subglacial Mountains (Figure S18.16, upper centre), correcting topography to sparse radar observations may leave obvious artefacts, and more detailed surveying is required to reveal the true nature of the bed. In other regions, however, such as the Aurora Subglacial Basin, smooth bed topography is seen even in the geophysical surveys, with a complete lack of roughness even at the smallest scales. We suggest that this may be due to a uniform sedimentary infill, providing lubricated and consistent ice flow conditions.

Finally, and as previously discussed, the IFPA method assumes that all variability in the surface

elevation and velocity datasets comes from the bed topography, and neglects the impact of shallow-ice and surface level processes, as well as artefacts in those input datasets. In the Terre Adélie Subglacial Highlands, the new map shows a defined channel feature, but likely also contains a lot of small scale artefacts from the ice surface data giving the repetitive linear texture. The new IFPA map shows that the interior of Wilkes Subglacial Basin (Figure S18.16) is significantly rougher than previously thought. However, there is a strong linear component of the topographic signal in this region (orientated at about 80 degrees from the vertical in the figures), and we suggest that this linear component is most likely inherited from an artefact in the input satellite data, rather than a feature of bed topography.

A more comprehensive selection of subglacial topography maps

We present in the main body of the text a selected regions of bed topography with features of particular interest. For completeness, we include a larger selection of figures here, covering the interior regions of the entire Antarctic continent, and providing a more comprehensive overview of the features detected using IFPA. In addition, we show the location of all the survey lines included in the Bedmap3 compendium (*7*), alongside a bed topography map compiled from these lines using streamline diffusion interpolation (BedMachine Antarctica v3, (*13*)), the IFPA$_{meso}$ bed topography, and the full IFPA topography which has been corrected to included all the information from the geophysical survey lines. This allows us to illustrate the new features which have been revealed in the bed topography using IFPA, and the step change in understanding from previous maps produced using interpolation methods, but also to highlight examples of regions where the IFPA method works less well. In general, and especially on the scale of the figures presented here, the new mesoscale details unveiled by the IFPA topography are most apparent in regions with a lower density of geophysical surveys. The majority of the landscape features discussed here are therefore in East Antarctica, which has a much lower geophysical survey density, but there are also new features in West Antarctica. The plots begin with West Antarctica, and then progress across Antarctica with an increasing x polar stereographic coordinate.

A few key points to consider while browsing these figures:

- **IFPA reveals intriguing new features in regions with sparse geophysical survey coverage**

In addition to the incised channels, tectonic boundaries, and increased detail in subglacial highlands discussed in the main body of the text, we see significantly more small scale roughness in the IFPA map than in previous topographic maps of subglacial Antarctica, particularly in fast flowing glacier trunks such as the Pensacola Pole Subglacial Basin (Figure S13.6), and Mellor Glacier (Figure S24.27). In the Foundation Basin, to the west of the Patuxent Range (bottom left of Figure S13.6), the IFPA topography map shows a ridge which cuts across the basin, but which does not have an obvious glacial explanation.

The IFPA map also provides insights into the spatial extent of rougher terrain. In appears that the mountainous terrain inland of the Denman Glacier rift, in the Golicya Subglacial Mountains, continues much further inland than detailed in previous topographic maps (Figure S27.34. Additionally, it highlights new smaller 'highland' provinces, such as to the west of Highlands B and C (Figure S26.31, upper part) and between the Slessor Subglacial Highlands and Maud Subglacial Basin (Figure S16.12, centre left).

In regions with some geophysical survey coverage, the IFPA map helps to show how topographic features are connected between radar survey lines, such as the valley which runs from the South Pole Basin in the direction of Enderby Land (Figure S15.10), and in the southern part of the Vostok Subglacial Highlands (Figure S19.17). In Interior Enderby Land, the new IFPA shows a strong linear trend to the topography, which is not identified in geophysical surveys due to their orientations.

- **IFPA is a complementary method to geophysical surveys**

  The Gamburtsev Subglacial Mountains (Figures S19.18, and S23.26) have already comprehensively surveyed (AGAP, (*48*)), and the interpolated topography in the survey area is much more detailed than the IFPA topography. However, outside of the survey rectangle, we see some ridges in the IFPA topography which were not detailed in the radar surveys (top left/middle of panel S23.26, and centre left of panel S19.18), illustrating how IFPA works as a complement to geophysical data collection methods.

  In the Golicyna Subglacial Mountains, we identify a new mountain range of more than 50 km in width in the IFPA topography (middle lower part of Figure S27.34). The geophysical survey line which crosses this region was not used in BedMachine Antarctica v3, but is used

in the radar corrected IFPA topography, and shows that this mountain range is much closer to the surface than it initially appeared. The region illustrates that IFPA is very effective at identifying subglacial features, even if the absolute elevation is unknown, and the positive effects of applying a post-processing step to correct for radar ice-thickness observations.

In the Pine Island Glacier region (Figure S11.1), we see an interesting phenomenon, where the ice-bed interface has previously been incorrectly identified in ice-penetrating radar data, due to the presence of an unusually thick volcanic layer in the ice column (*79*). This caused anomalous topography in BedMachine Antarctica v3, but has now been corrected for the IFPA map.

- **Some of the names used here are not currently included in the SCAR Composite Gazetteer of Antarctica.**

  We indicate those informal names which are not included with an asterisk (*) in the Figure caption, although we note that many of these are in common usage in the scientific literature.

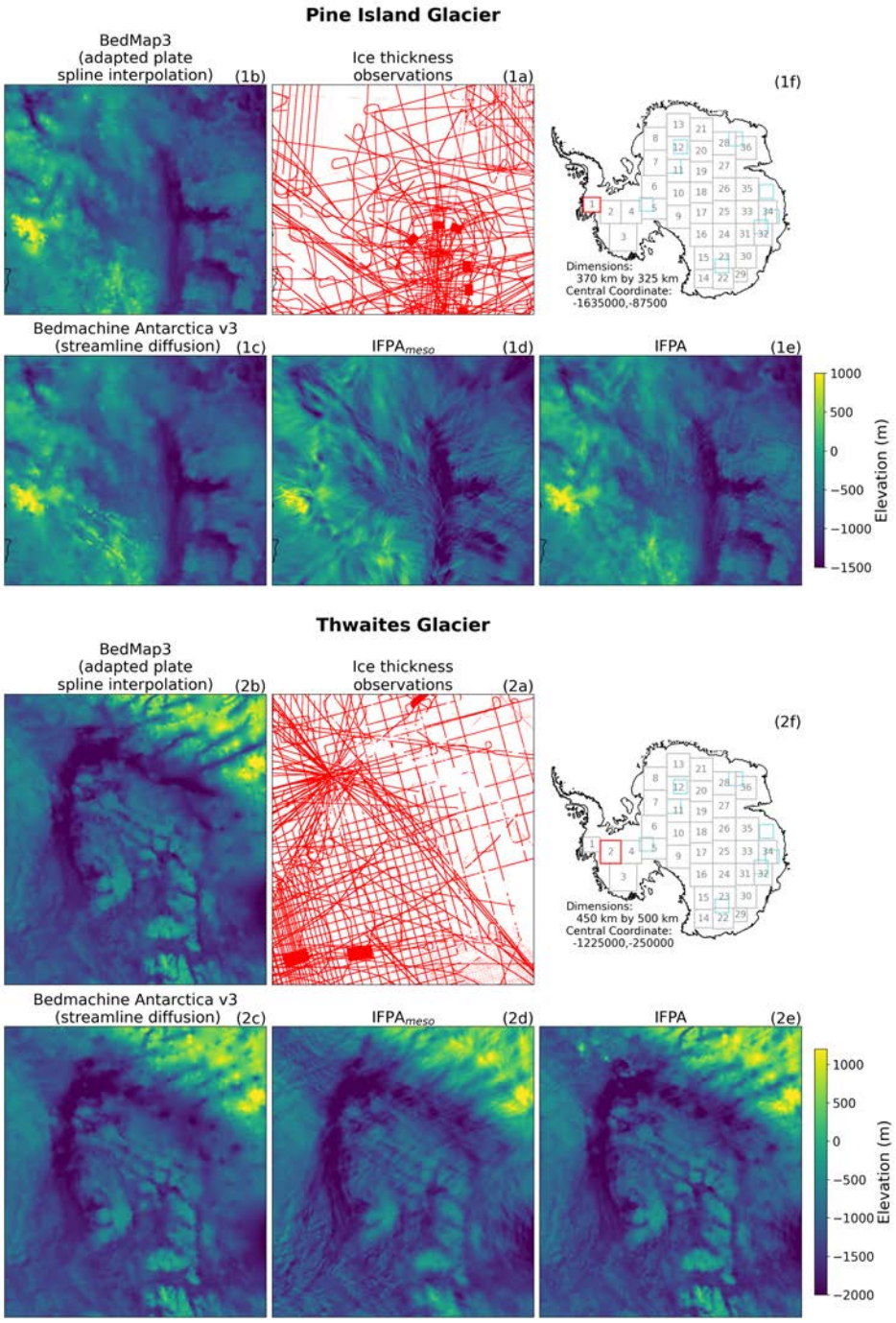

Figure S11: **Pine Island Glacier and Thwaites Glacier**. Panels (a) show the radar data available in the Bedmap3 compendium (*7*) in this region. Panels (b-e) show a comparison of the bed topography from (b) Bedmap 3 (which uses an adapted plate spline interpolation), (c) BedMachine Antarctica v3 (which uses streamline diffusion in interior sectors to interpolate between radar observations of ice thickness), (d) IFPA$_{meso}$ (prior to applying correction to geophysical thickness measurements), and (e) IFPA (with geophysical correction implemented). Panel (f) shows the location of the region in the Antarctic overview map.

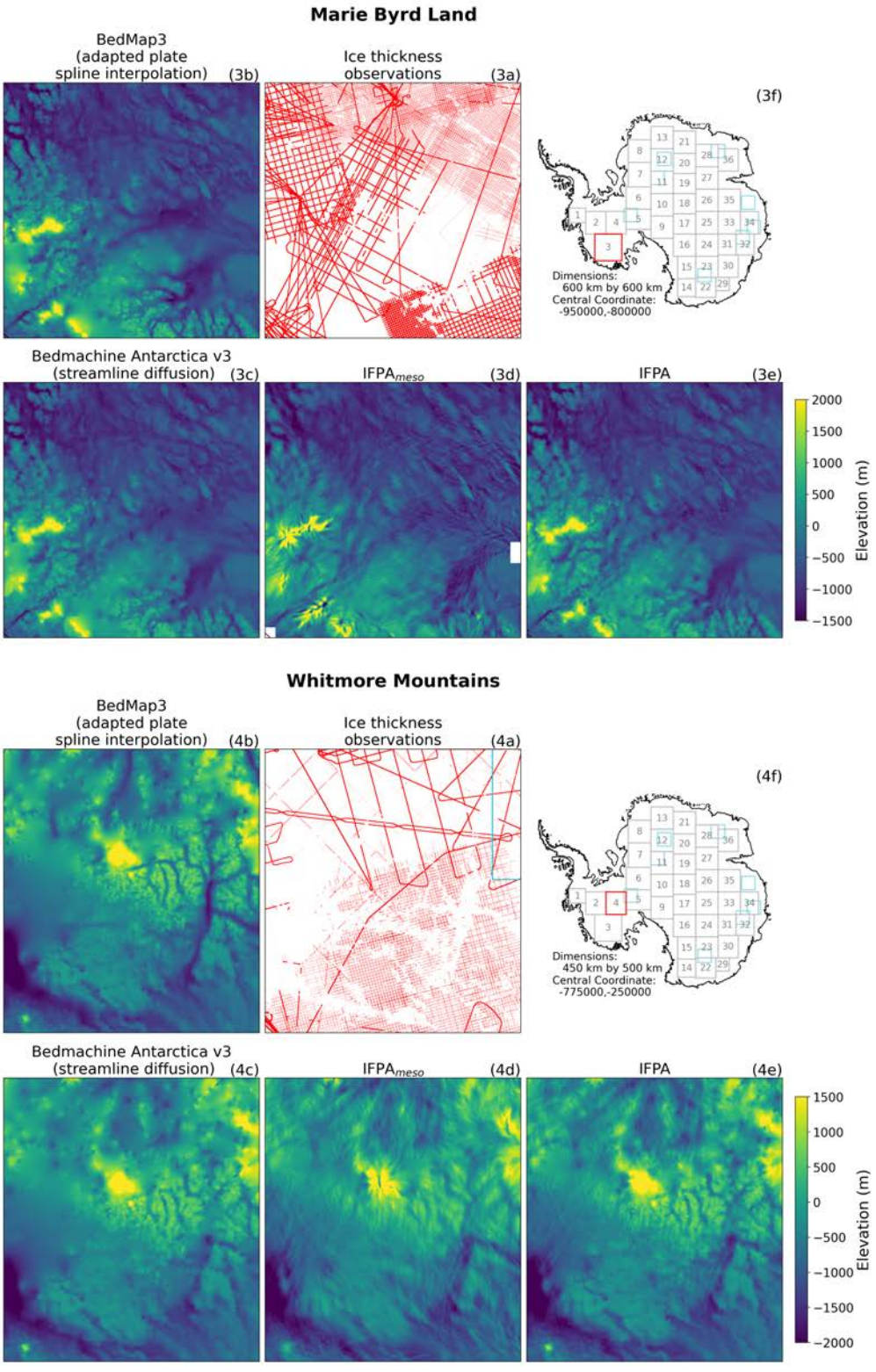

Figure S12: **Marie Byrd Land, and Whitmore Mountains**. Panels the same as S11.

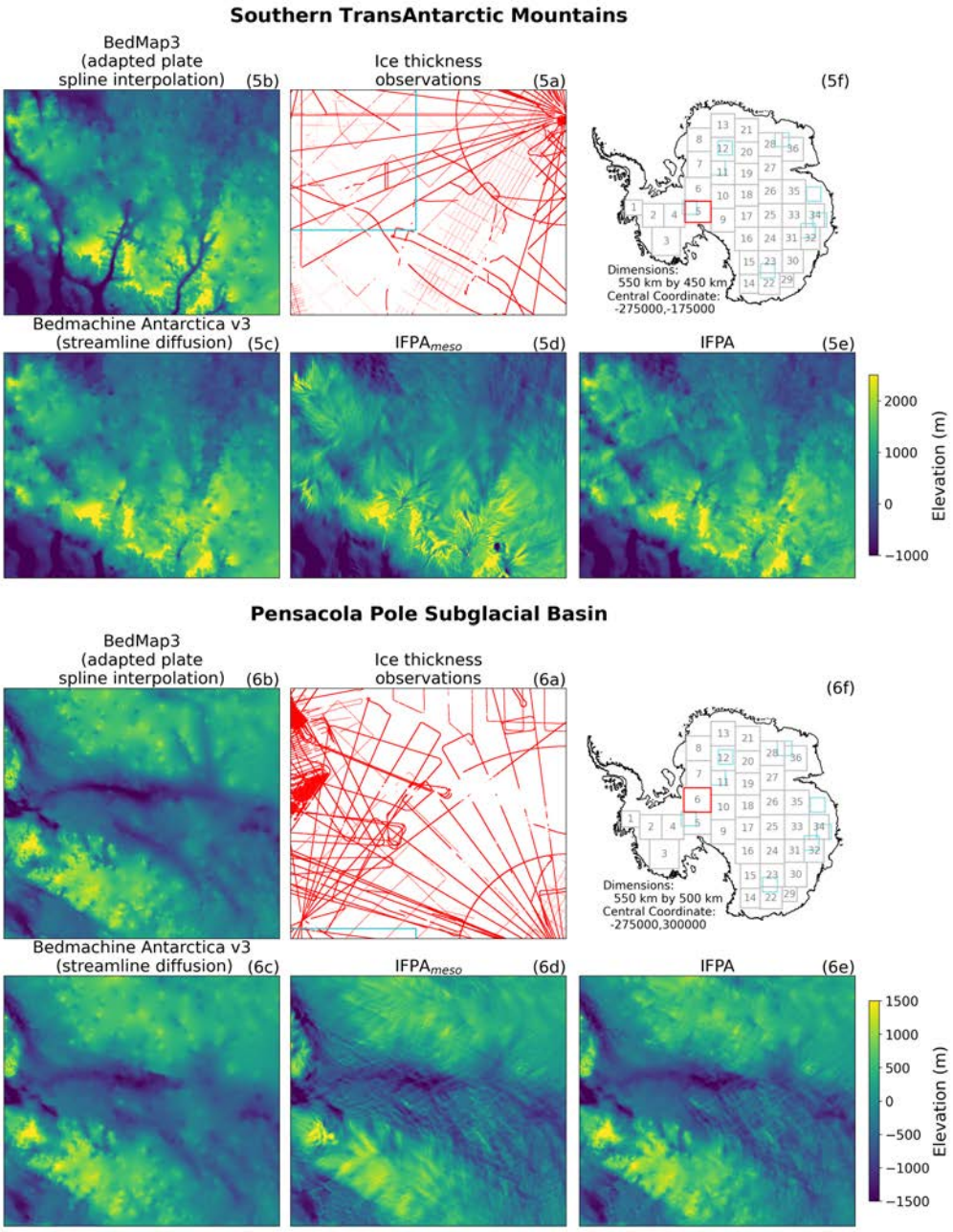

Figure S13: **Southern TransAntarctic Mountains and Pensacola Pole Subglacial Basin***. Panels the same as S11.

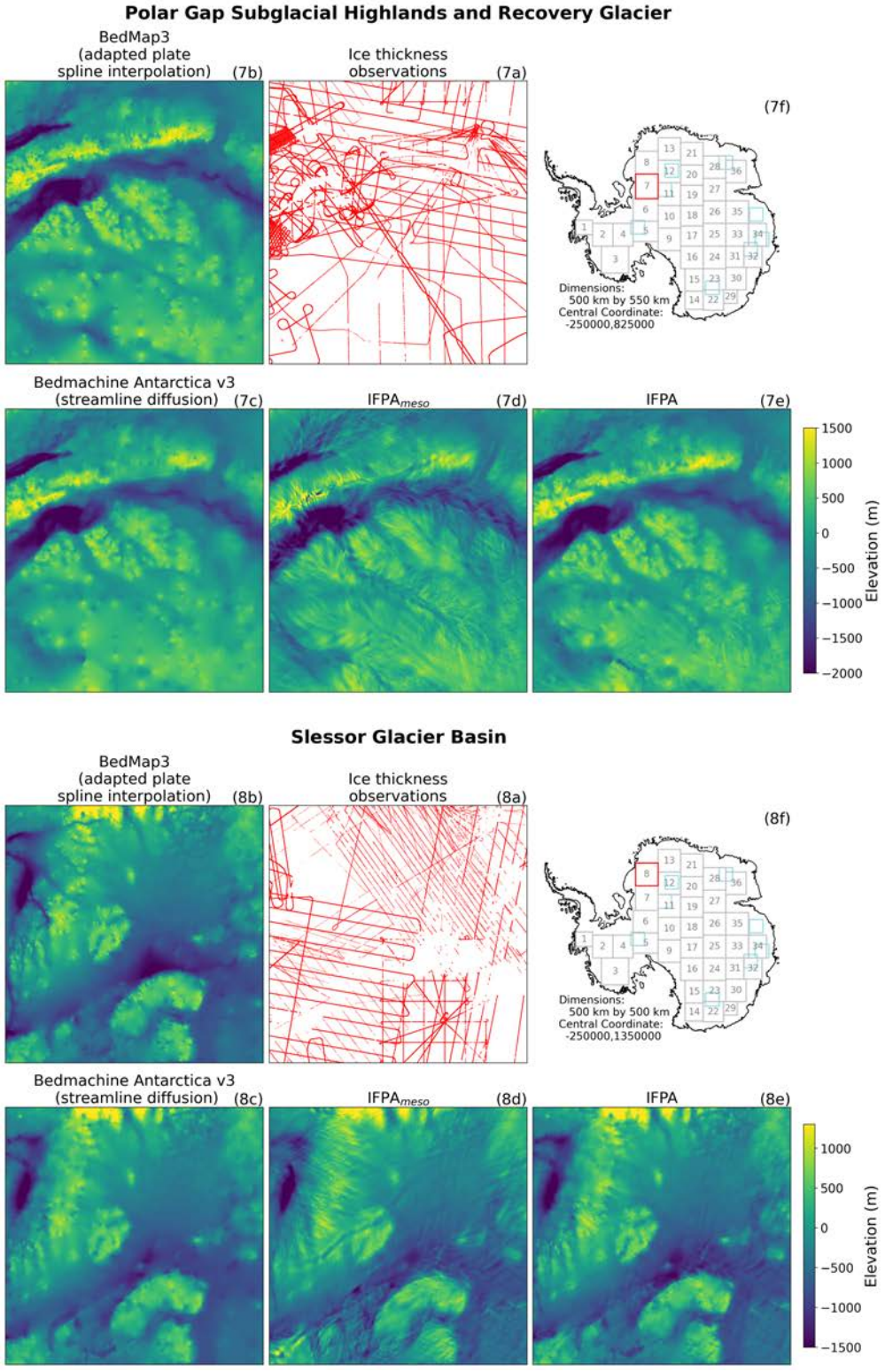

Figure S14: **Polar Gap Subglacial Highlands, Recovery Glacier, and Slessor Glacier Basin**. Panels the same as S11.

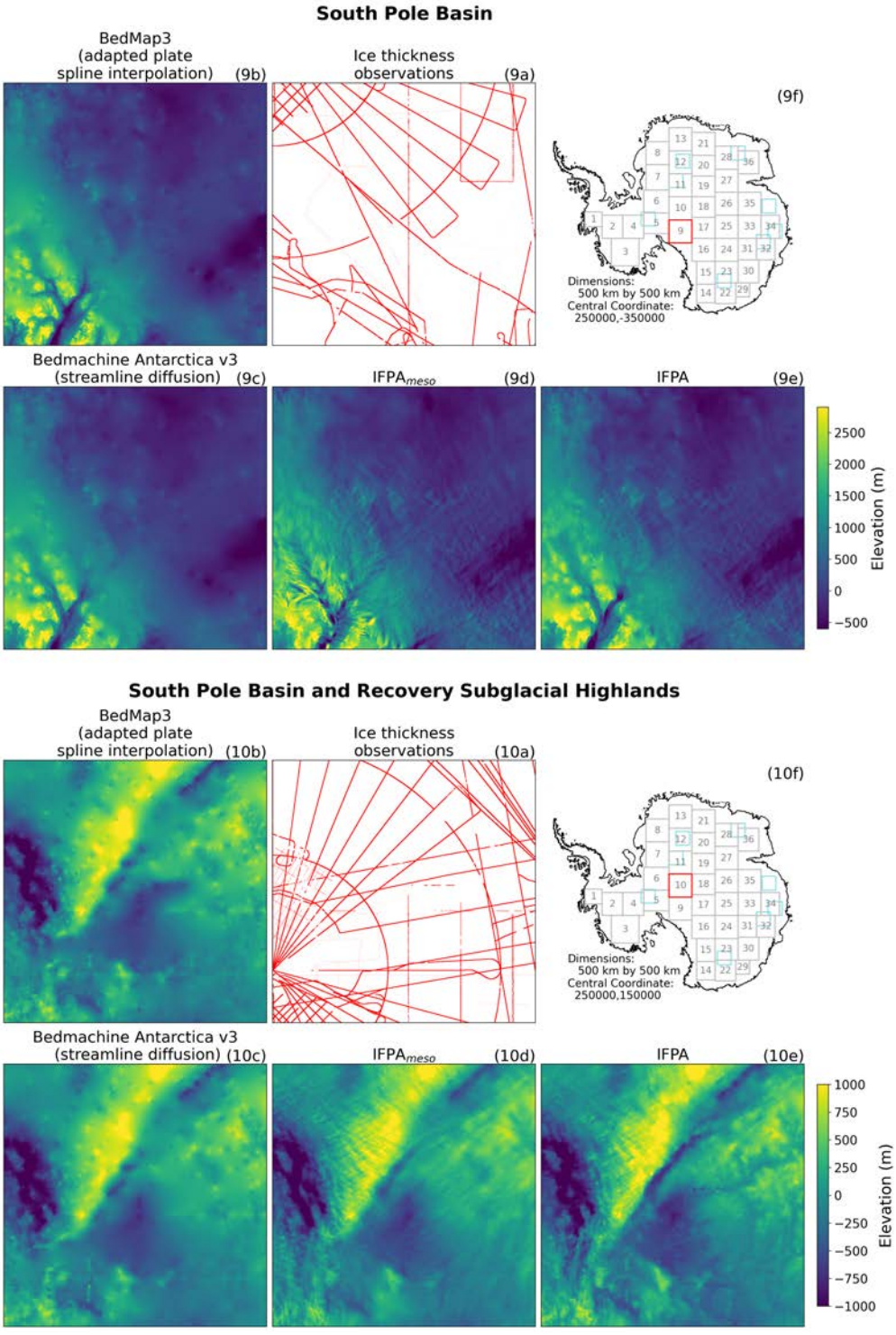

Figure S15: **South Pole Basin and Recovery Subglacial Highlands***. Panels the same as S11.

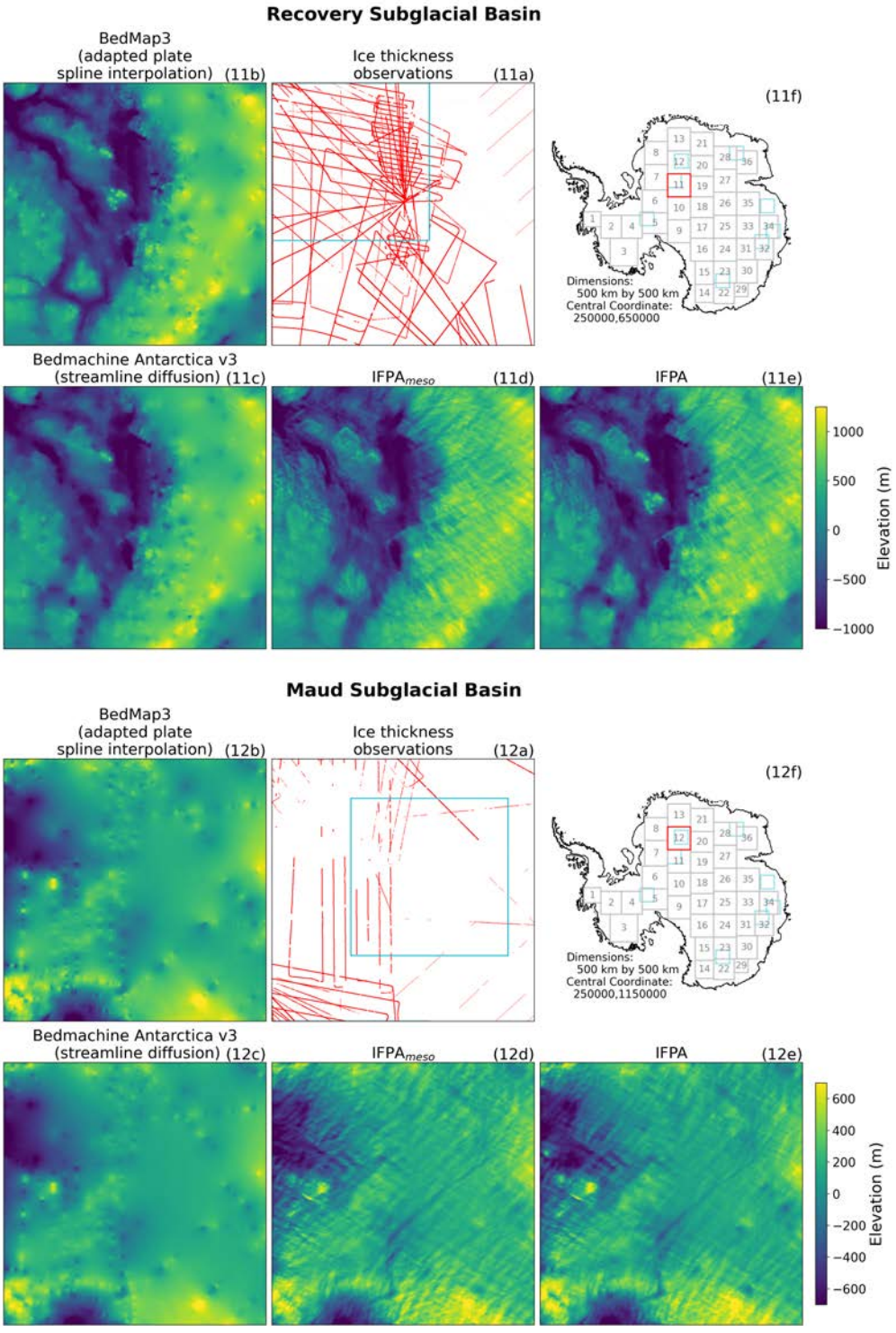

Figure S16: **Recovery Subglacial Basin and Maud Subglacial Basin.** Panels the same as S11.

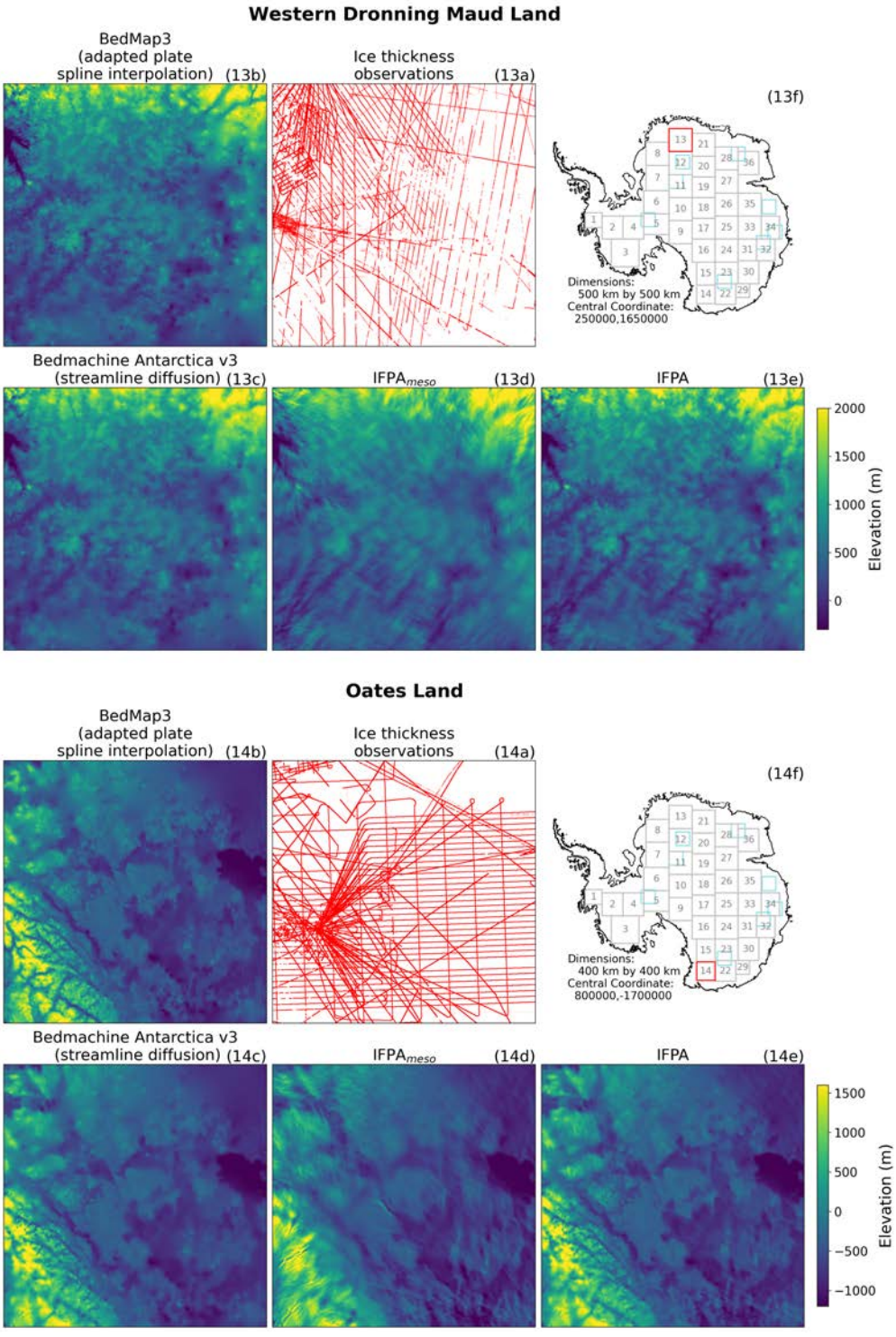

Figure S17: **Western Dronning Maud Land and Oates Land**. Panels the same as S11.

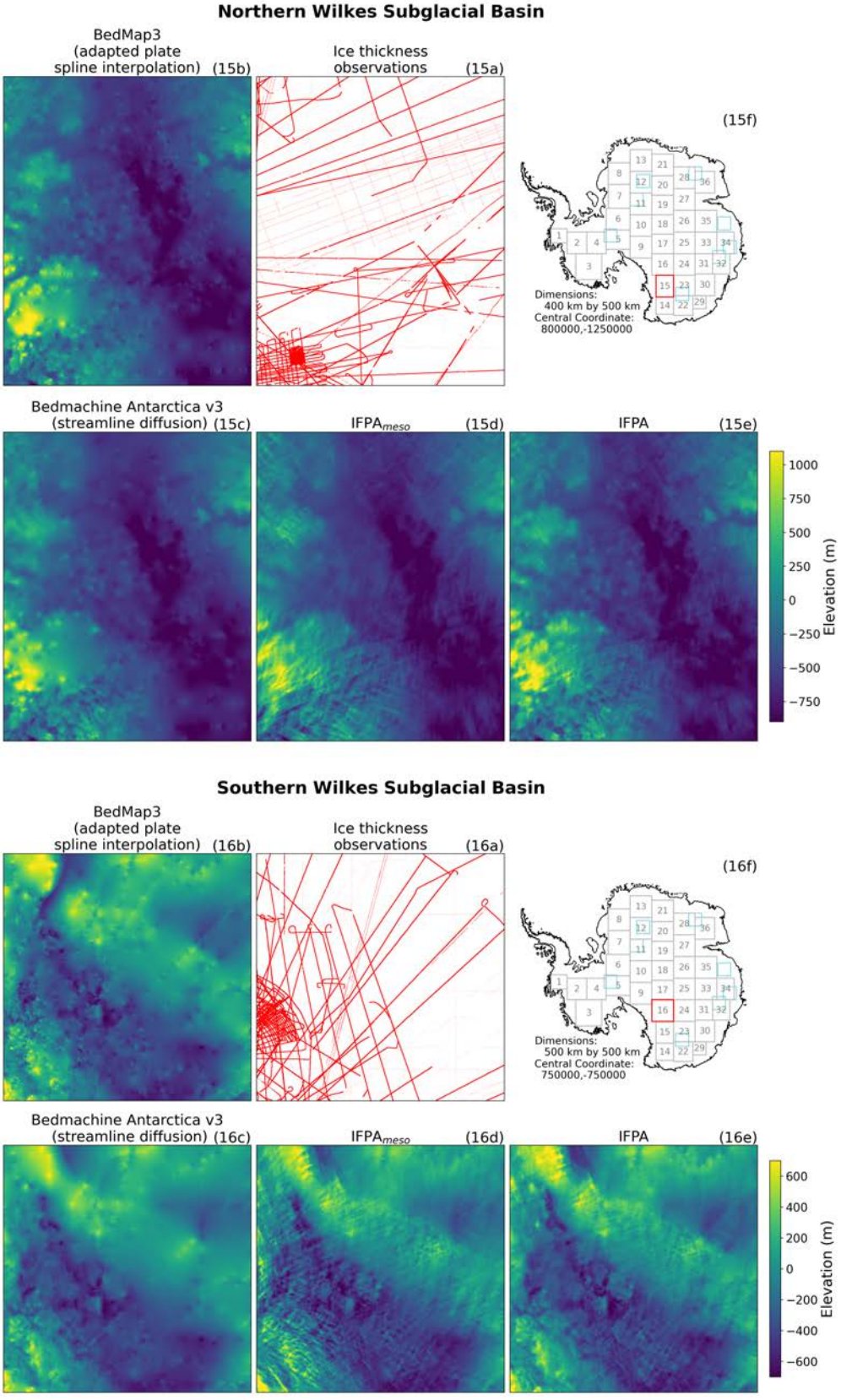

Figure S18: **Northern Wilkes Subglacial Basin and Southern Wilkes Subglacial Basin.**. Panels the same as S11.

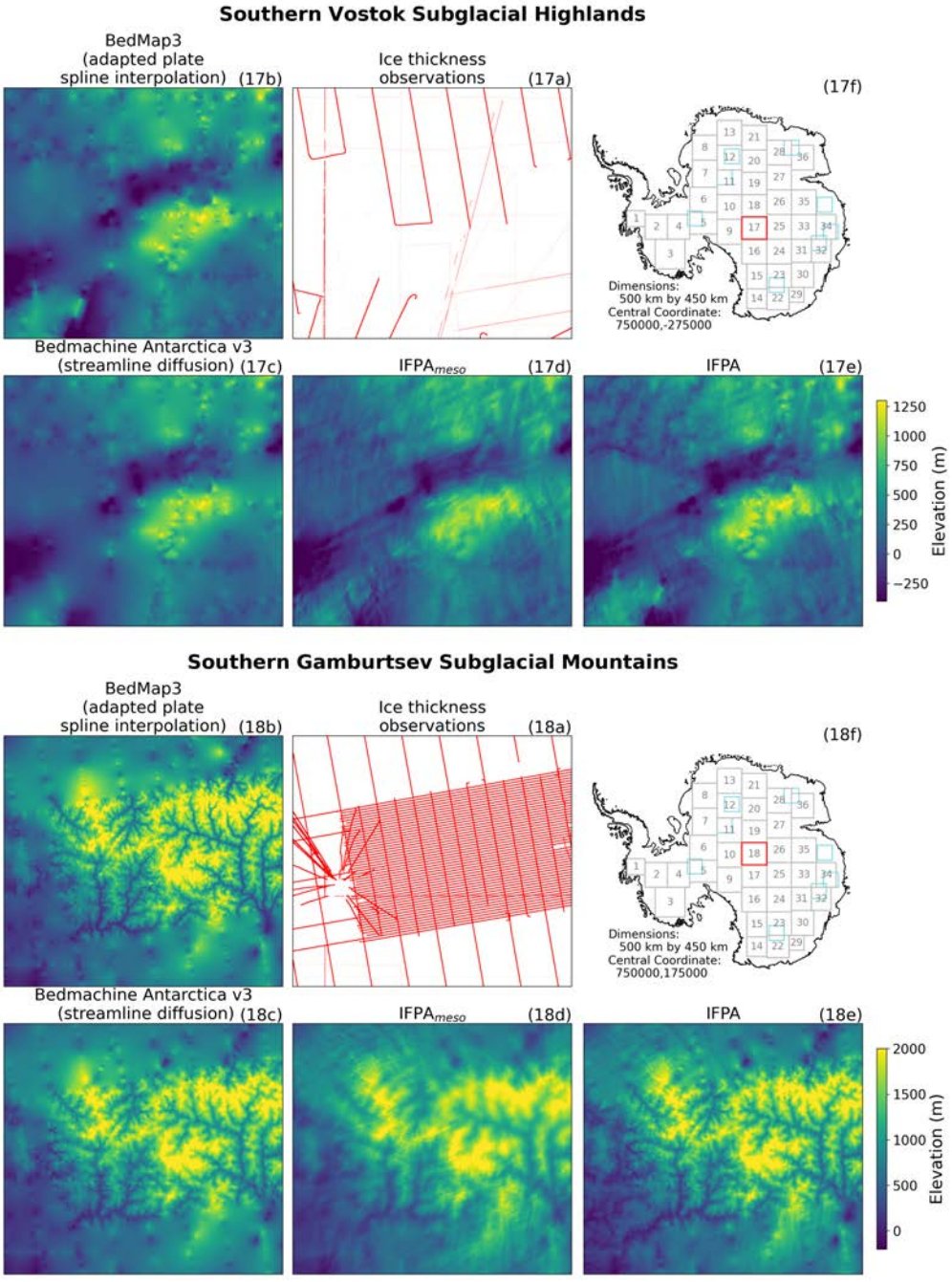

Figure S19: **Southern Vostok Subglacial Highlands and Southern Gambertsev Subglacial Mountains.** Panels the same as S11.

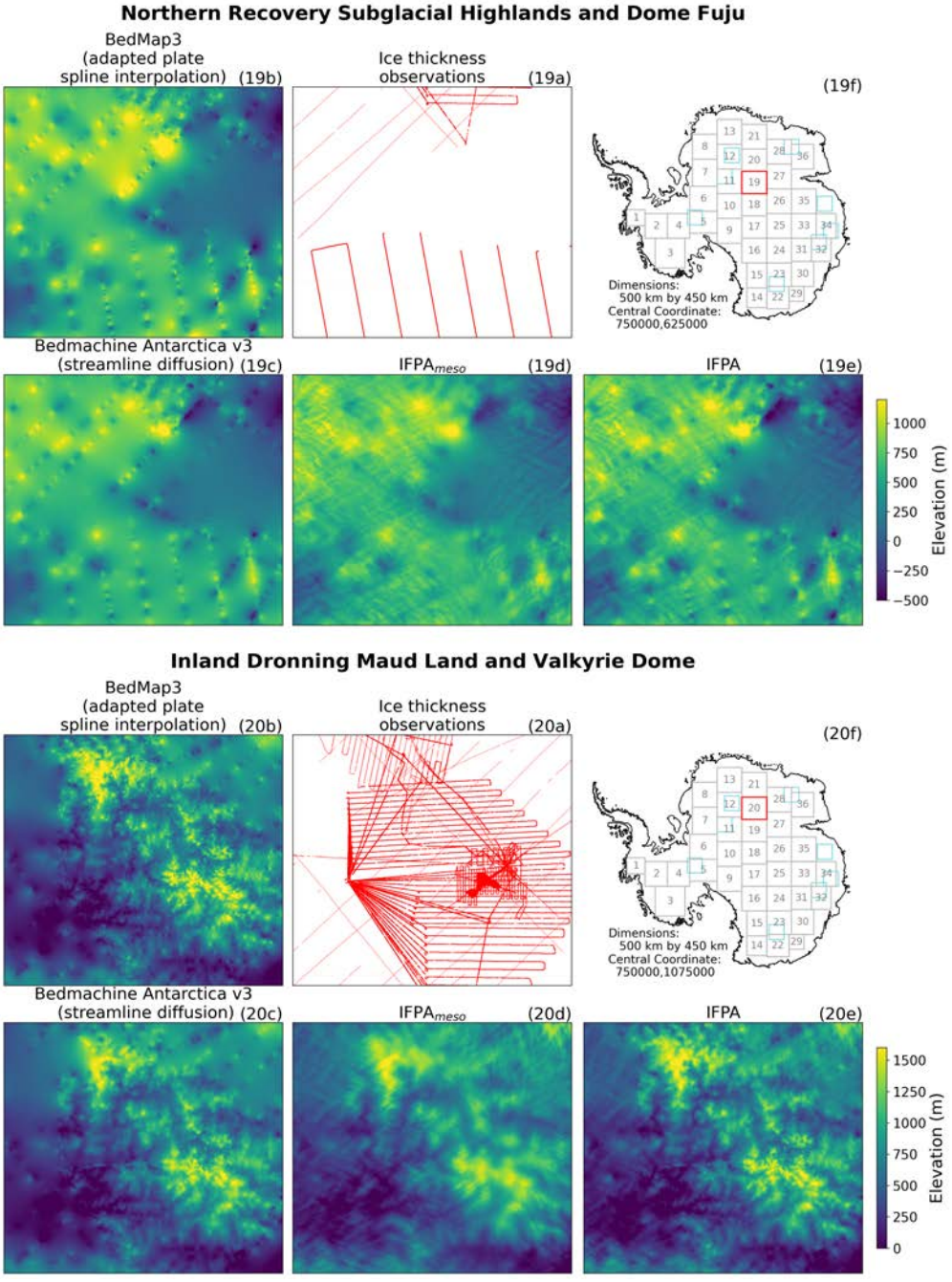

Figure S20: **Northern Recovery Subglacial Highlands, Dome Fuji, Inland Dronning Maud Land, Valkyrie Dome.** Panels the same as S11.

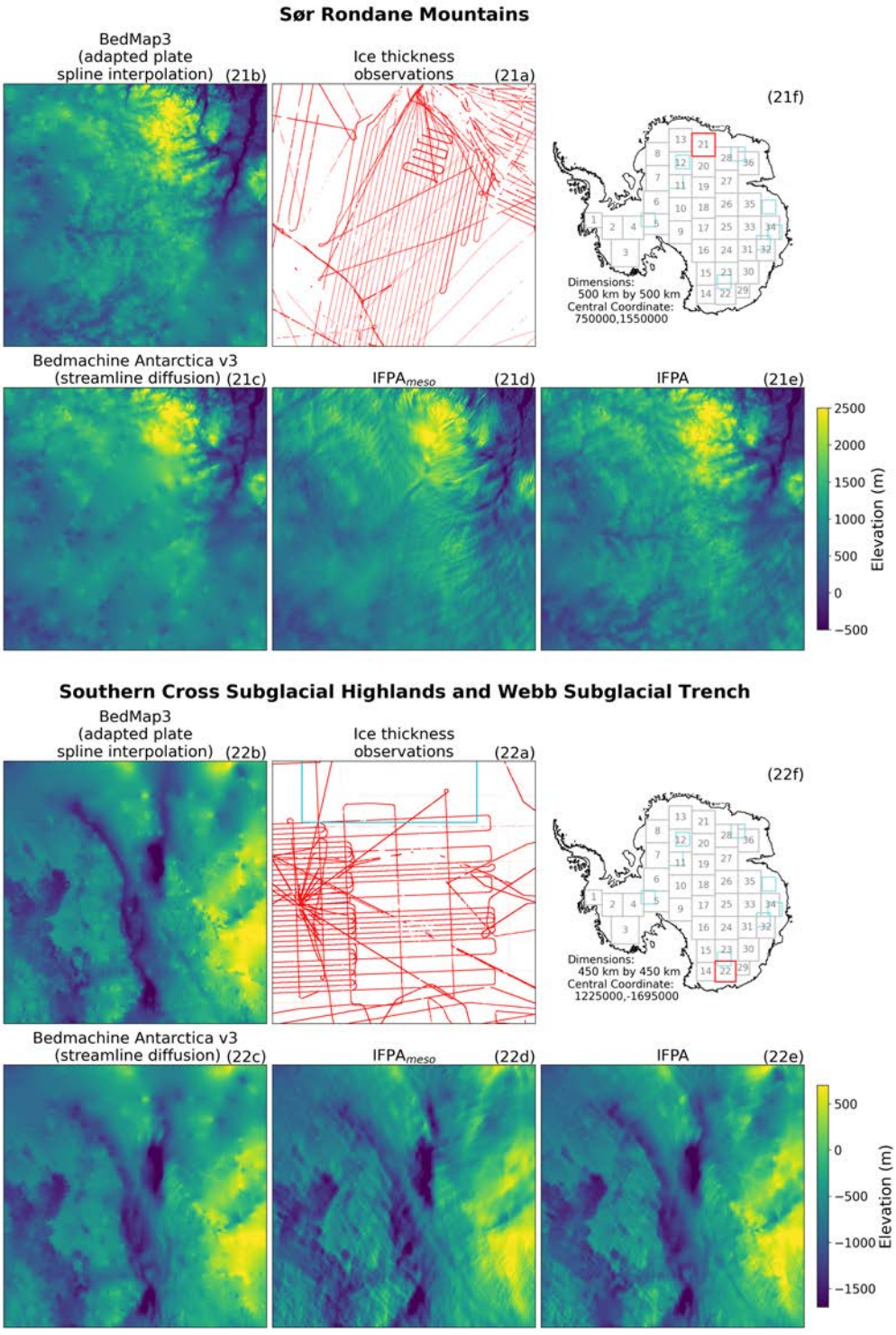

Figure S21: **Sør Rondane Mountains, Southern Cross Subglacial Highlands and Webb Subglacial Trench*.** Panels the same as S11.

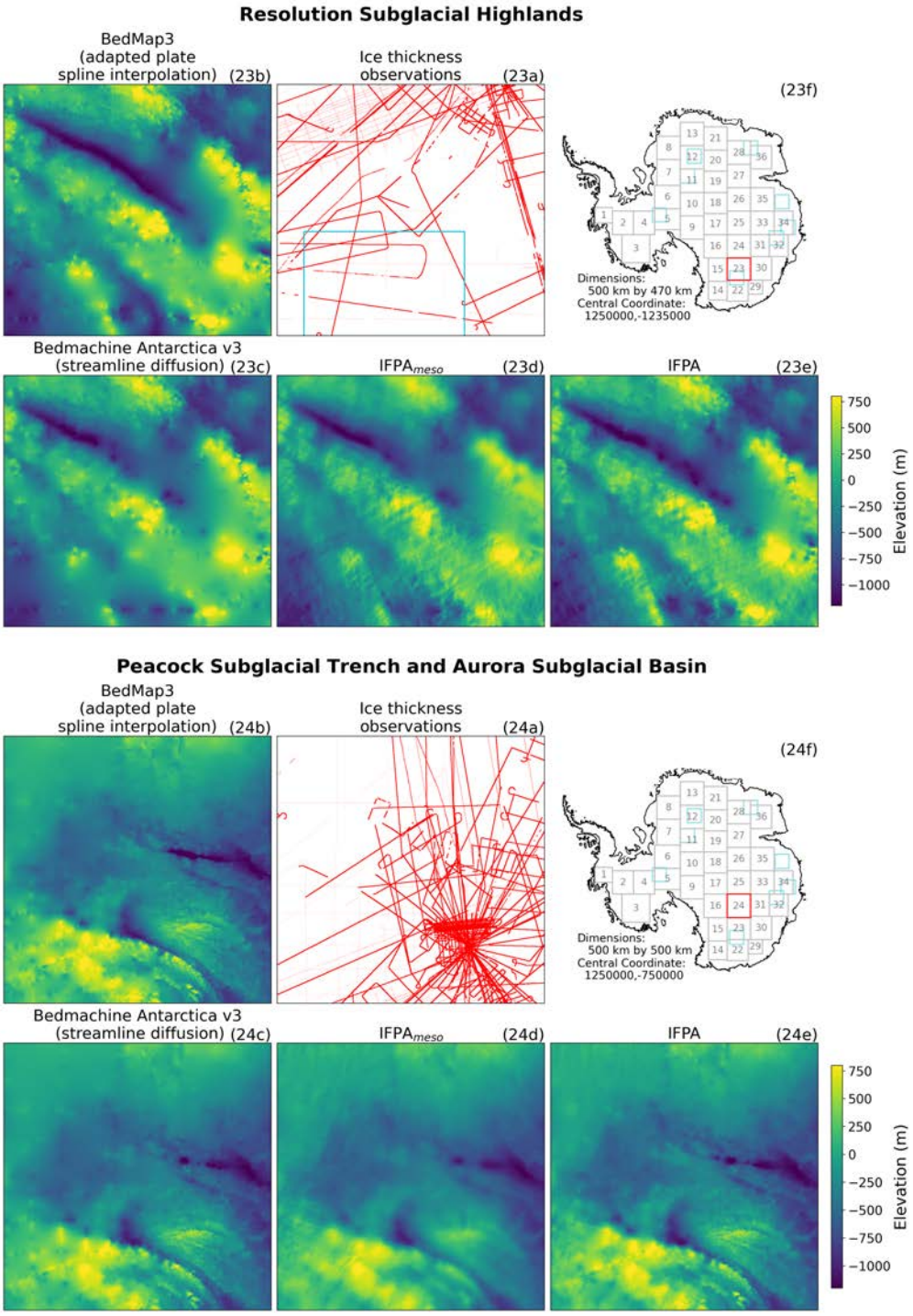

Figure S22: **Resolution Subglacial Highlands, Peacock Subglacial Trench and Aurora Subglacial Basin.** Panels the same as S11.

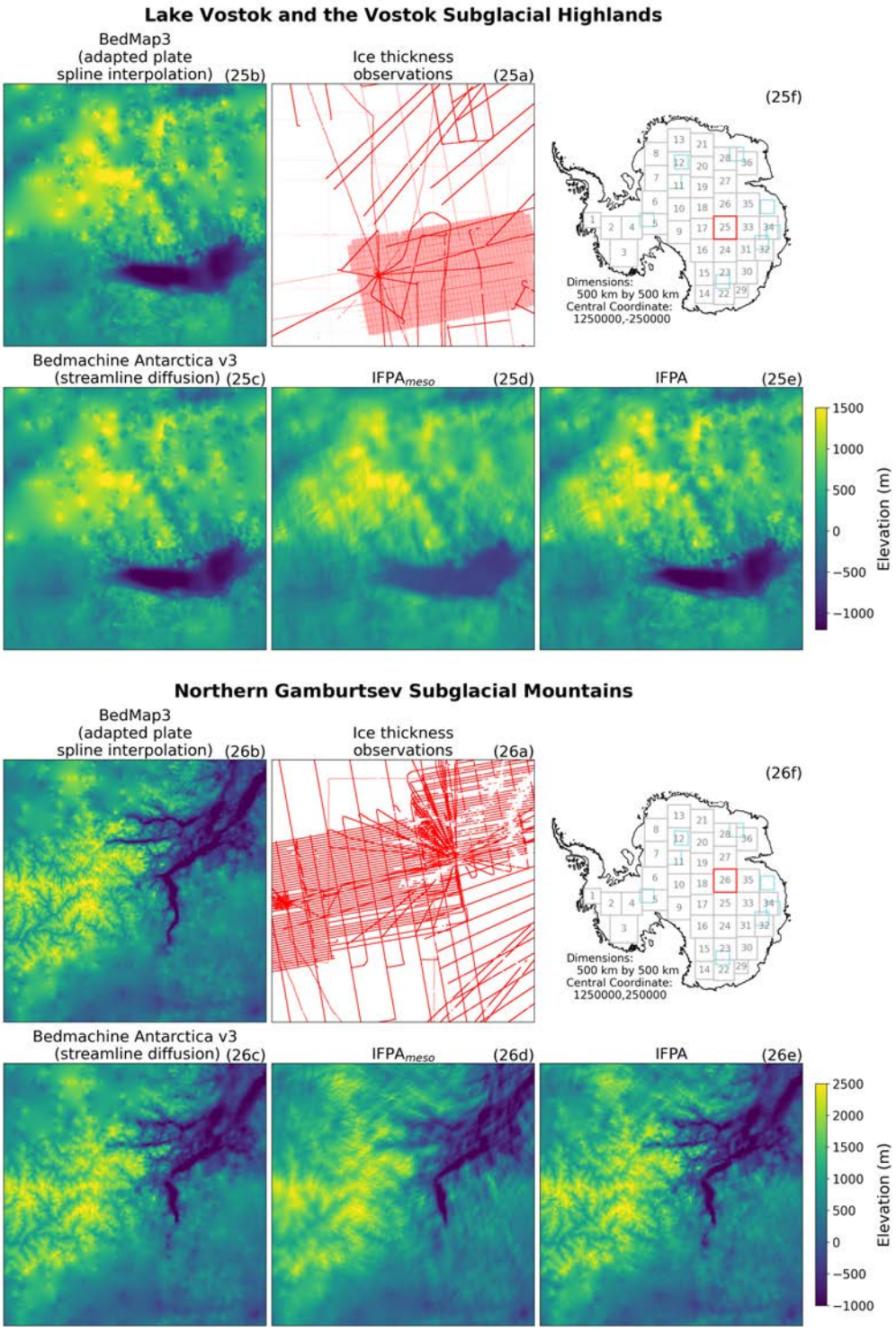

Figure S23: **Lake Vostok, the Vostok Subglacial Highlands, and the Northern Gamburtsev Subglacial Mountains** Panels the same as S11.

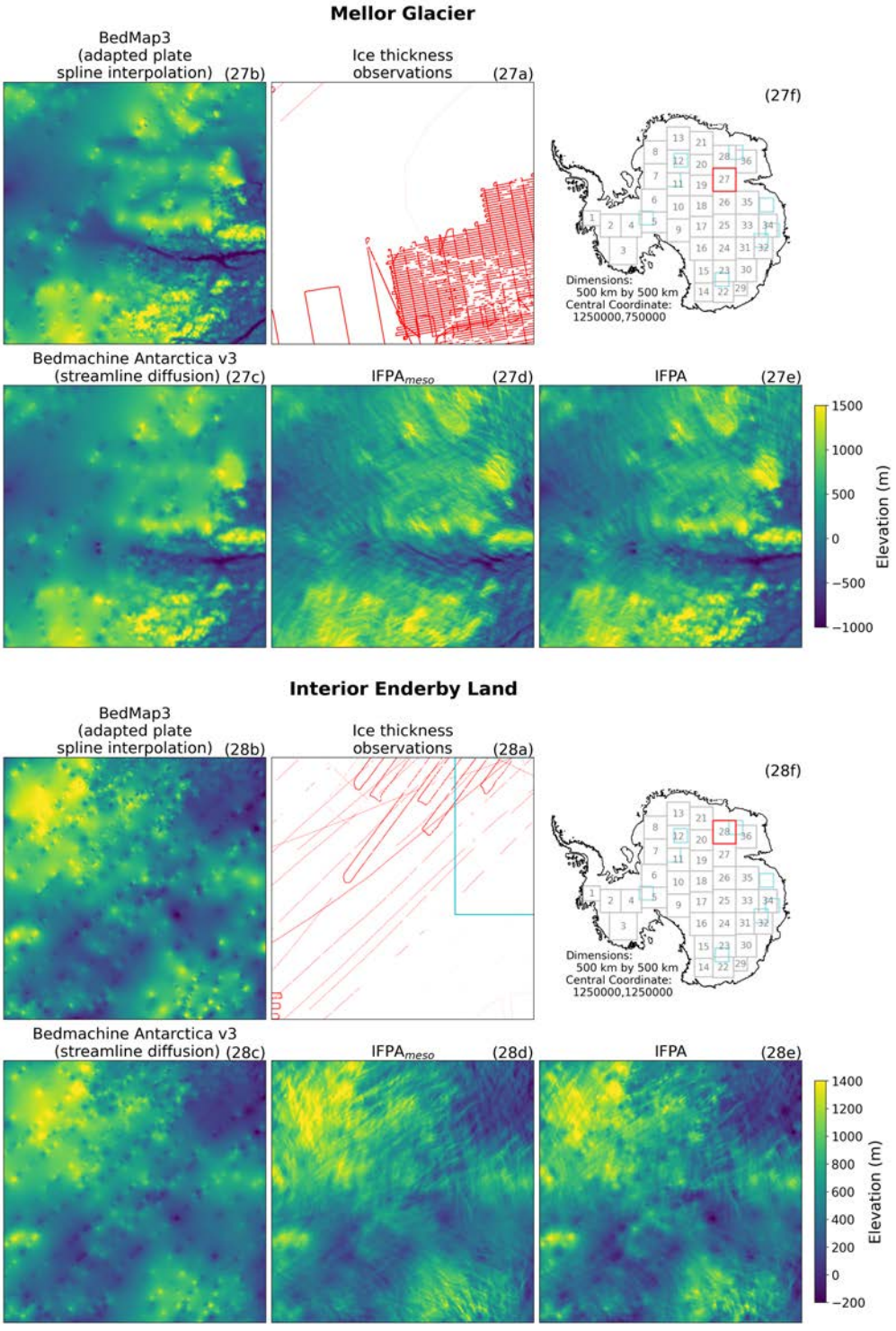

Figure S24: **Mellor Glacier and Interior Enderby Land.** Panels the same as S11.

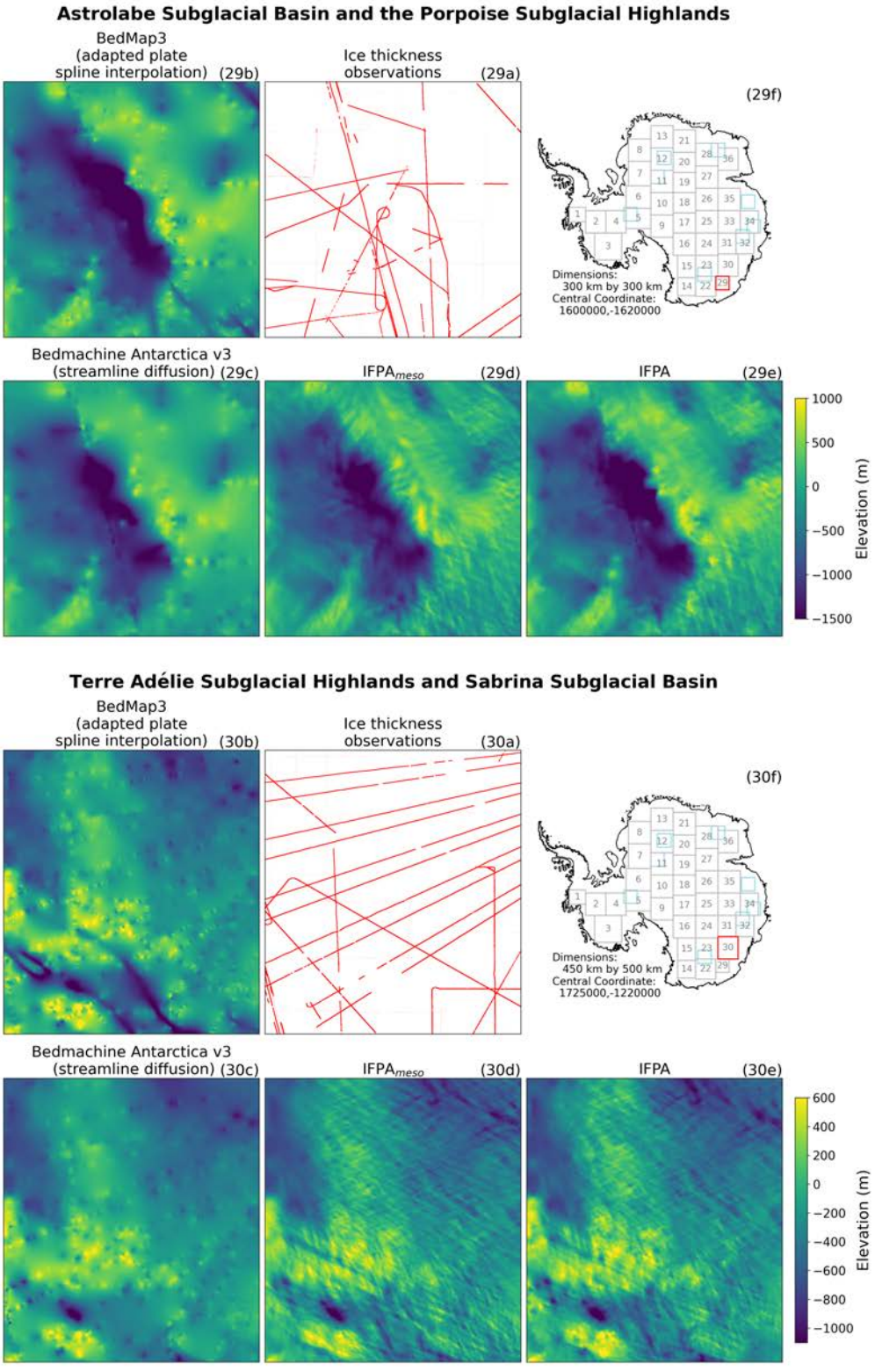

Figure S25: **Astrolabe Subglacial Basin, the Porpose Subglacial Highlands, the Terre Adélie Subglacial Highlands* and Sabrina Subglacial Basin*.** Panels the same as S11.

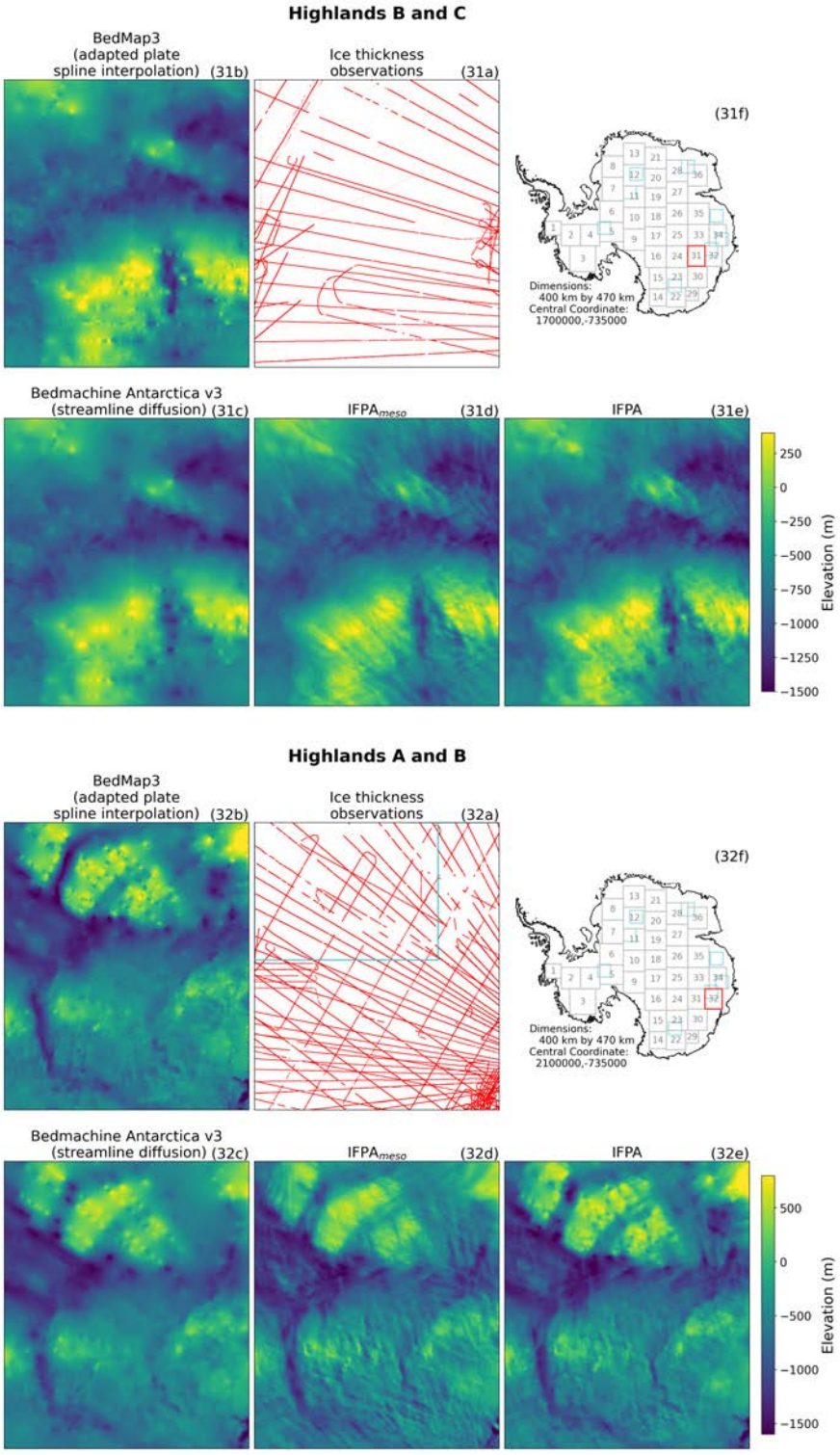

Figure S26: **Highlands A*, B* and C* and Queen Mary Land** Panels the same as S11.

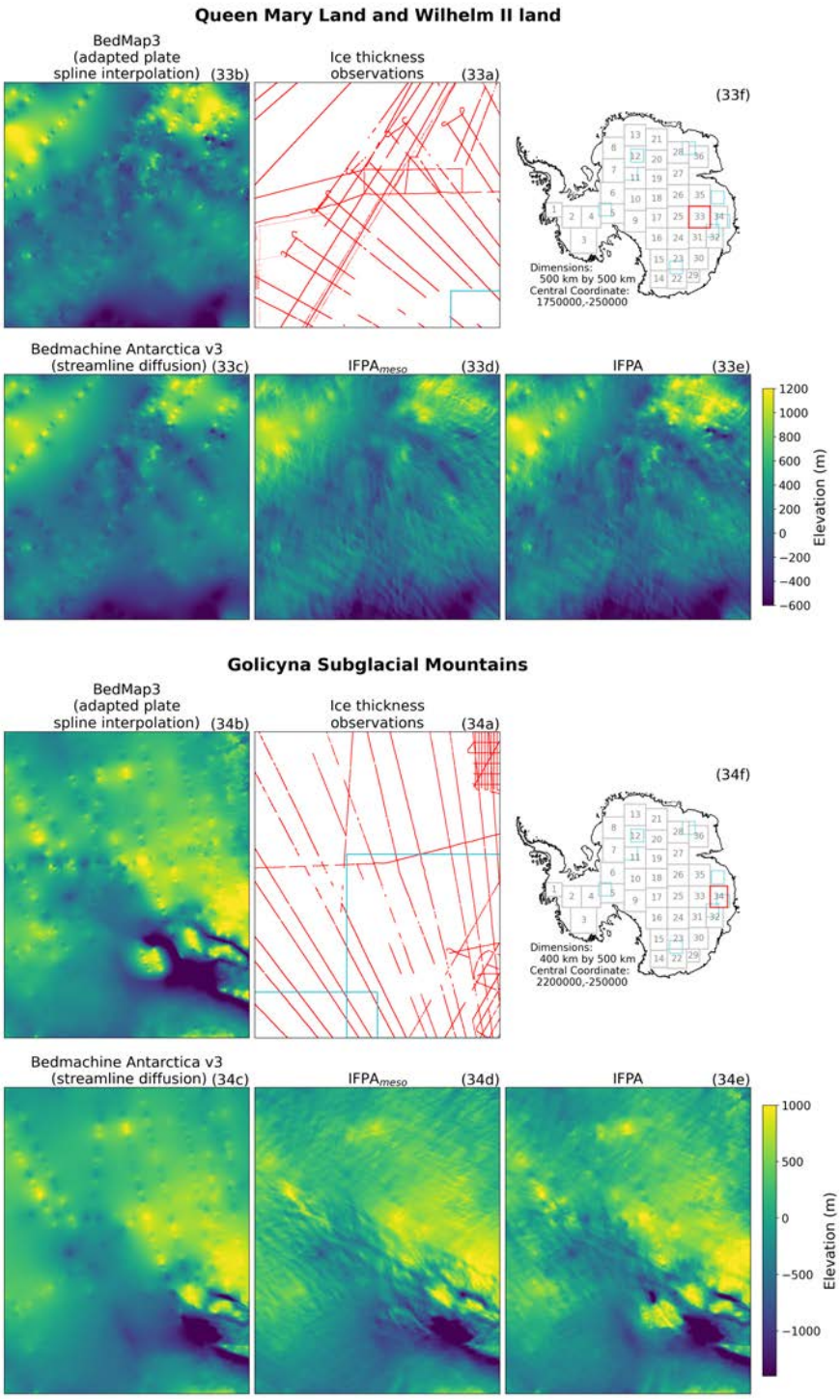

Figure S27: **Wilhelm II Land and Golicyna Subglacial Mountains** Panels the same as S11.

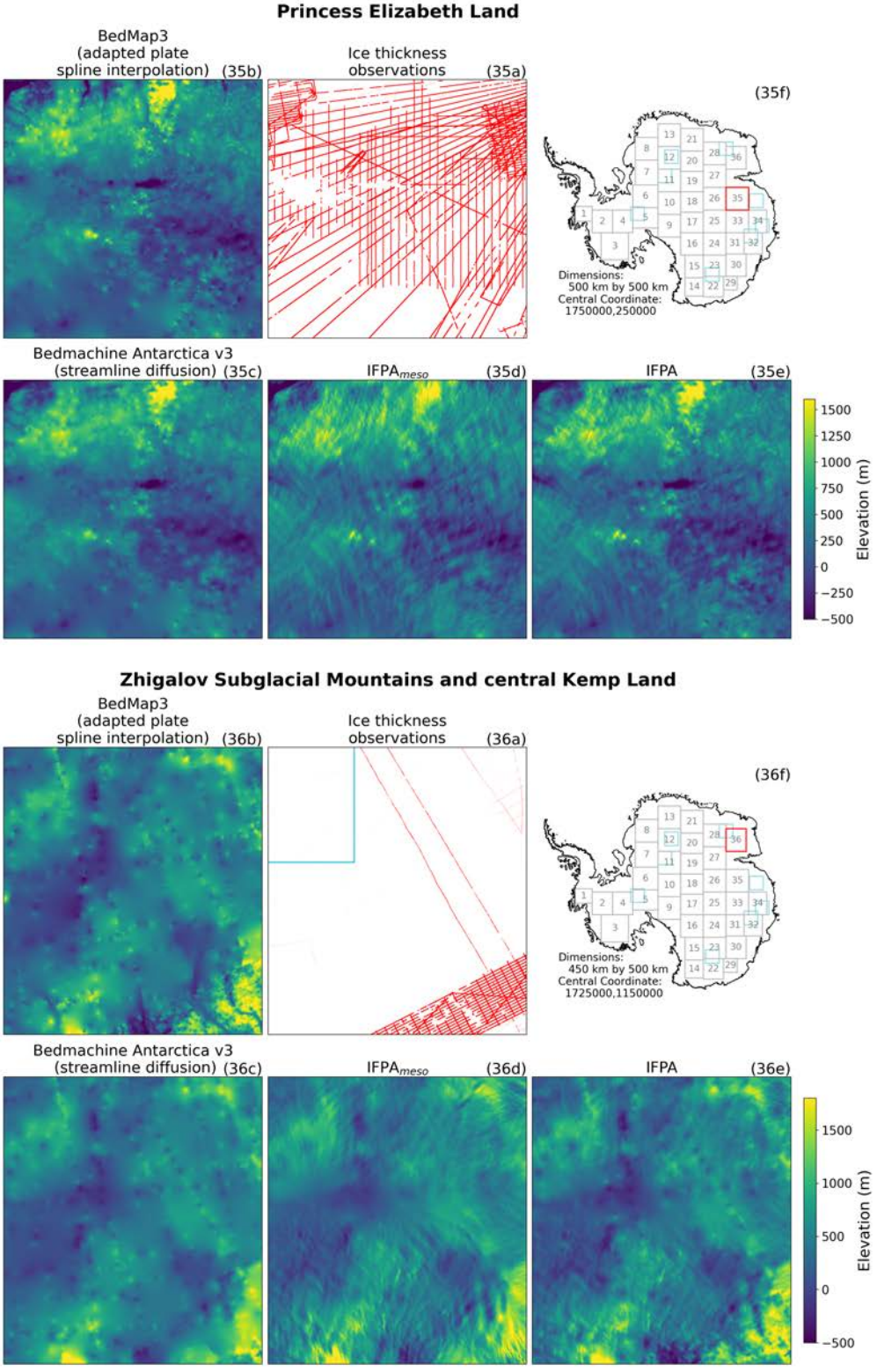

Figure S28: **Princess Elizabeth Land, the Zhigalov Subglacial Mountains and central Kemp Land**. Panels the same as S11.

References and Notes

1. Intergovernmental Panel on Climate Change (IPCC), "The Ocean and Cryosphere in a Changing Climate: Special Report of the Intergovernmental Panel on Climate Change" (Cambridge Univ. Press, 2022); https://doi.org/10.1017/9781009157964.

2. Intergovernmental Panel on Climate Change (IPCC), "9 – Ocean, Cryosphere and Sea Level Change" (Cambridge Univ. Press, 2023); https://doi.org/10.1017/9781009157896.011.

3. K. Gwinner, F. Scholten, F. Preusker, S. Elgner, T. Roatsch, M. Spiegel, R. Schmidt, J. Oberst, R. Jaumann, C. Heipke, Topography of Mars from global mapping by HRSC high-resolution digital terrain models and orthoimages: Characteristics and performance. *Earth Planet. Sci. Lett.* **294**, 506–519 (2010). doi:10.1016/j.epsl.2009.11.007

4. R. R. Herrick, D. L. Stahlke, V. L. Sharpton, Fine-scale Venusian topography from Magellan stereo data. *Eos* **93**, 125–126 (2012). doi:10.1029/2012EO120002

5. K. J. Becker, M. S. Robinson, T. L. Becker, L. A. Weller, K. L. Edmundson, G. A. Neumann, M. E. Perry, S. C. Solomon, "First global digital elevation model of Mercury" in *47th Annual Lunar and Planetary Science Conference* (2016); pp. 2959.

6. Y. Yu, D. T. Sandwell, G. Dibarboure, Abyssal marine tectonics from the SWOT mission. *Science* **386**, 1251–1256 (2024). doi:10.1126/science.ads4472 Medline

7. A. C. Fr'emand, P. Fretwell, J. A. Bodart, H. D. Pritchard, A. Aitken, J. L. Bamber, R. Bell, C. Bianchi, R. G. Bingham, D. D. Blankenship, G. Casassa, G. Catania, K. Christianson, H. Conway, H. F. J. Corr, X. Cui, D. Damaske, V. Damm, R. Drews, G. Eagles, O. Eisen, H. Eisermann, F. Ferraccioli, E. Field, R. Forsberg, S. Franke, S. Fujita, Y. Gim, V. Goel, S. P. Gogineni, J. Greenbaum, B. Hills, R. C. A. Hindmarsh, A. O. Hoffman, P. Holmlund, N. Holschuh, J. W. Holt, A. N. Horlings, A. Humbert, R. W. Jacobel, D. Jansen, A. Jenkins, W. Jokat, T. Jordan, E. King, J. Kohler, W. Krabill, M. Kusk Gillespie, K. Langley, J. Lee, G. Leitchenkov, C. Leuschen, B. Luyendyk, J. MacGregor, E. MacKie, K. Matsuoka, M. Morlighem, J. Mouginot, F. O. Nitsche, Y. Nogi, O. A. Nost, J. Paden, F. Pattyn, S. V. Popov, E. Rignot, D. M. Rippin, A. Rivera, J. Roberts, N. Ross, A. Ruppel, D. M. Schroeder, M. J. Siegert, A. M. Smith, D. Steinhage, M. Studinger, B. Sun, I. Tabacco, K. Tinto, S. Urbini, D. Vaughan, B. C. Welch, D. S. Wilson, D. A. Young, A. Zirizzotti, Antarctic Bedmap data: Findable, Accessible, Interoperable, and Reusable (FAIR) sharing of 60 years of ice bed, surface, and thickness data. *Earth Syst. Sci. Data* **15**, 2695–2710 (2023). doi:10.5194/essd-15-2695-2023

8. H. D. Pritchard, P. T. Fretwell, A. C. Fremand, J. A. Bodart, J. D. Kirkham, A. Aitken, J. Bamber, R. Bell, C. Bianchi, R. G. Bingham, D. D. Blankenship, G. Casassa, K. Christianson, H. Conway, H. F. J. Corr, X. Cui, D. Damaske, V. Damm, B. Dorschel, R. Drews, G. Eagles, O. Eisen, H. Eisermann, F. Ferraccioli, E. Field, R. Forsberg, S. Franke, V. Goel, S. P. Gogineni, J. Greenbaum, B. Hills, R. C. A. Hindmarsh, A. O. Hoffman, N. Holschuh, J. W. Holt, A. Humbert, R. W. Jacobel, D. Jansen, A. Jenkins, W. Jokat, L. Jong, T. A. Jordan, E. C. King, J. Kohler, W. Krabill, J. Maton, M. K. Gillespie, K. Langley, J. Lee, G. Leitchenkov, C. Leuschen, B. Luyendyk, J. A. MacGregor, E. MacKie, G. Moholdt, K. Matsuoka, M. Morlighem, J. Mouginot, F. O. Nitsche, O. A. Nost, J. Paden, F. Pattyn, S. Popov, E. Rignot, D. M. Rippin, A. Rivera, J. L. Roberts, N. Ross, A. Ruppel, D. M. Schroeder, M. J. Siegert, A. M. Smith, D. Steinhage, M.

Studinger, B. Sun, I. Tabacco, K. J. Tinto, S. Urbini, D. G. Vaughan, D. S. Wilson, D. A. Young, A. Zirizzotti, Bedmap3 updated ice bed, surface and thickness gridded datasets for Antarctica. *Sci. Data* **12**, 414 (2025). doi:10.1038/s41597-025-04672-y Medline

9. G. Durand, O. Gagliardini, L. Favier, T. Zwinger, E. le Meur, Impact of bedrock description on modeling ice sheet dynamics. *Geophys. Res. Lett.* **38**, L20501 (2011). doi:10.1029/2011GL048892

10. S. Sun, S. L. Cornford, Y. Liu, J. C. Moore, Dynamic response of Antarctic ice shelves to bedrock uncertainty. *Cryosphere* **8**, 1561–1576 (2014). doi:10.5194/tc-8-1561-2014

11. F. McCormack, B. Galton-Fenzi, H. Seroussi, J. Roberts, The impact of bed elevation resolution on Thwaites Glacier ice dynamics. Twenty-Fifth Annual WAIS Workshop (2018).

12. B. A. Castleman, N.-J. Schlegel, L. Caron, E. Larour, A. Khazendar, Derivation of bedrock topography measurement requirements for the reduction of uncertainty in ice-sheet model projections of Thwaites Glacier. *Cryosphere* **16**, 761–778 (2022). doi:10.5194/tc-16-761-2022

13. M. Morlighem, E. Rignot, T. Binder, D. Blankenship, R. Drews, G. Eagles, O. Eisen, F. Ferraccioli, R. Forsberg, P. Fretwell, V. Goel, J. S. Greenbaum, H. Gudmundsson, J. Guo, V. Helm, C. Hofstede, I. Howat, A. Humbert, W. Jokat, N. B. Karlsson, W. S. Lee, K. Matsuoka, R. Millan, J. Mouginot, J. Paden, F. Pattyn, J. Roberts, S. Rosier, A. Ruppel, H. Seroussi, E. C. Smith, D. Steinhage, B. Sun, M. R. van den Broeke, T. D. van Ommen, M. van Wessem, D. A. Young, Deep glacial troughs and stabilizing ridges unveiled beneath the margins of the Antarctic ice sheet. *Nat. Geosci.* **13**, 132–137 (2020). doi:10.1038/s41561-019-0510-8

14. M. Margold, C. R. Stokes, C. D. Clark, Ice streams in the Laurentide Ice Sheet: Identification, characteristics and comparison to modern ice sheets. *Earth Sci. Rev.* **143**, 117–146 (2015). doi:10.1016/j.earscirev.2015.01.011

15. K. A. Hogan, R. D. Larter, A. G. C. Graham, R. Arthern, J. D. Kirkham, R. L. Totten, T. A. Jordan, R. Clark, V. Fitzgerald, A. K. Wåhlin, J. B. Anderson, C.-D. Hillenbrand, F. O. Nitsche, L. Simkins, J. A. Smith, K. Gohl, J. E. Arndt, J. Hong, J. Wellner, Revealing the former bed of Thwaites Glacier using sea floor bathymetry: Implications for warm-water routing and bed controls on ice flow and buttressing. *Cryosphere* **14**, 2883–2908 (2020). doi:10.5194/tc-14-2883-2020

16. F. A. M. Falcini, M. Krabbendam, K. A. Selby, D. M. Rippin, Using bed-roughness signatures to characterise glacial landform assemblages beneath palaeo-ice sheets. *J. Glaciol.* **68**, 518–532 (2022). doi:10.1017/jog.2021.122

17. E. MacKie, D. Schroeder, J. Caers, M. Siegfried, C. Scheidt, Antarctic topographic realizations and geostatistical modeling used to map subglacial lakes. *J. Geophys. Res. Earth Surf.* **125**, e2019JF005420 (2020). doi:10.1029/2019JF005420

18. W. J. Leong, H. J. Horgan, DeepBedMap: A deep neural network for resolving the bed topography of Antarctica. *Cryosphere* **14**, 3687–3705 (2020). doi:10.5194/tc-14-3687-2020

19. Y. Cai, Z. Yao, S. Lang, X. Cui, F. Wan, Y. He, Generative Elevation Inpainting: An Efficient Completion Method for Generating High-Resolution Antarctic Bed Topography. *IEEE Trans. Geosci. Remote Sens.* **61**, 1–17 (2023). doi:10.1109/TGRS.2023.3303231

20. H. Ockenden, R. G. Bingham, A. Curtis, D. Goldberg, Inverting ice surface elevation and velocity for bed topography and slipperiness beneath Thwaites Glacier. *Cryosphere* **16**, 3867–3887 (2022). doi:10.5194/tc-16-3867-2022

21. H. Ockenden, R. G. Bingham, A. Curtis, D. Goldberg, Ice-Flow Perturbation Analysis: A method to estimate ice-sheet bed topography and conditions from surface datasets. *J. Glaciol.* **69**, 1–10 (2023). doi:10.1017/jog.2023.50

22. I. M. Howat, C. Porter, B. E. Smith, M.-J. Noh, P. Morin, The Reference Elevation Model of Antarctica. *Cryosphere* **13**, 665–674 (2019). doi:10.5194/tc-13-665-2019

23. J. Mouginot, E. Rignot, B. Scheuchl, Continent-Wide, Interferometric SAR Phase, Mapping of Antarctic Ice Velocity. *Geophys. Res. Lett.* **46**, 9710–9718 (2019). doi:10.1029/2019GL083826

24. Y. Dong, J. Zhao, C. Li, M. Liao, Gapless-REMA100: A gapless 100-m reference elevation model of Antarctica with voids filled by multi-source DEMs. *ISPRS J. Photogramm. Remote Sens.* **186**, 70–82 (2022). doi:10.1016/j.isprsjprs.2022.01.024

25. K. C. Rose, N. Ross, R. G. Bingham, H. F. J. Corr, F. Ferraccioli, T. A. Jordan, A. M. Le Brocq, D. M. Rippin, M. J. Siegert, A temperate former West Antarctic ice sheet suggested by an extensive zone of subglacial meltwater channels. *Geology* **42**, 971–974 (2014). doi:10.1130/G35980.1

26. S. J. Livingstone, W. Chu, J. C. Ely, J. Kingslake, Paleofluvial and subglacial channel networks beneath Humboldt Glacier, Greenland. *Geology* **45**, 551–554 (2017). doi:10.1130/G38860.1

27. S. S. R. Jamieson, N. Ross, G. J. G. Paxman, F. J. Clubb, D. A. Young, S. Yan, J. Greenbaum, D. D. Blankenship, M. J. Siegert, An ancient river landscape preserved beneath the East Antarctic Ice Sheet. *Nat. Commun.* **14**, 6507 (2023). doi:10.1038/s41467-023-42152-2 Medline

28. S. S. R. Jamieson, N. Ross, J. S. Greenbaum, D. A. Young, A. R. A. Aitken, J. L. Roberts, D. D. Blankenship, S. Bo, M. J. Siegert, An extensive subglacial lake and canyon system in Princess Elizabeth Land, East Antarctica. *Geology* **44**, 87–90 (2016). doi:10.1130/G37220.1

29. X. Cui, H. Jeofry, J. S. Greenbaum, J. Guo, L. Li, L. E. Lindzey, F. A. Habbal, W. Wei, D. A. Young, N. Ross, M. Morlighem, L. M. Jong, J. L. Roberts, D. D. Blankenship, S. Bo, M. J. Siegert, Bed topography of Princess Elizabeth land in East Antarctica. *Earth Syst. Sci. Data* **12**, 2765–2774 (2020). doi:10.5194/essd-12-2765-2020

30. A. O. Hoffman, N. Holschuh, M. Mueller, J. Paden, A. Muto, G. Ariho, C. Brigham, J. E. Christian, L. Davidge, E. Heitmann, B. Hills, A. Horlings, S. Morey, G. O'Connor, T. J. Fudge, E. J. Steig, K. Christianson, Scars of tectonism promote ice-sheet nucleation from Hercules Dome into West Antarctica. *Nat. Geosci.* **16**, 1–9 (2023). doi:10.1038/s41561-023-01265-5

31. R. E. Bell, M. Studinger, C. A. Shuman, M. A. Fahnestock, I. Joughin, Large subglacial lakes in East Antarctica at the onset of fast-flowing ice streams. *Nature* **445**, 904–907 (2007). doi:10.1038/nature05554 Medline

32. A. Humbert, D. Steinhage, V. Helm, S. Beyer, T. Kleiner, Missing evidence of widespread subglacial lakes at Recovery Glacier, Antarctica. *J. Geophys. Res. Earth Surf.* **123**, 2802–2826 (2018). doi:10.1029/2017JF004591

33. A. Diez, K. Matsuoka, T. A. Jordan, J. Kohler, F. Ferraccioli, H. F. Corr, A. V. Olesen, R. Forsberg, T. G. Casal, Patchy lakes and topographic origin for fast flow in the Recovery Glacier system, East Antarctica. *J. Geophys. Res. Earth Surf.* **124**, 287–304 (2019). doi:10.1029/2018JF004799

34. A. R. A. Aitken, L. Li, B. Kulessa, D. Schroeder, T. A. Jordan, J. M. Whittaker, S. Anandakrishnan, E. J. Dawson, D. A. Wiens, O. Eisen, M. J. Siegert, Antarctic Sedimentary Basins and Their Influence on Ice-Sheet Dynamics. *Reviews of Geophysics* **61**, e2021RG000767 (2023). doi:10.1029/2021RG000767

35. O. Eisen, A. Winter, D. Steinhage, T. Kleiner, A. Humbert, Basal roughness of the East Antarctic Ice Sheet in relation to flow speed and basal thermal state. *Ann. Glaciol.* **61**, 162–175 (2020). doi:10.1017/aog.2020.47

36. D. W. Ashmore, R. G. Bingham, Antarctic subglacial hydrology: Current knowledge and future challenges. *Antarct. Sci.* **26**, 758–773 (2014). doi:10.1017/S0954102014000546

37. E. J. Lea, S. S. Jamieson, M. J. Bentley, Alpine topography of the Gamburtsev Subglacial Mountains, Antarctica, mapped from ice sheet surface morphology. *Cryosphere* **18**, 1733–1751 (2024). doi:10.5194/tc-18-1733-2024

38. C. Schoof, Basal perturbations under ice streams: Form drag and surface expression. *J. Glaciol.* **48**, 407–416 (2002). doi:10.3189/172756502781831269

39. D. E. Sugden, B. S. John, Glaciers and landscape: A geomorphological approach. *Edward Arnold London* **365**, 1–363 (1976). doi:10.14430/arctic3017

40. M. J. Siegert, J. Taylor, A. J. Payne, Spectral roughness of subglacial topography and implications for former ice-sheet dynamics in East Antarctica. *Global Planet. Change* **45**, 249–263 (2005). doi:10.1016/j.gloplacha.2004.09.008

41. S. Franke, H. Eisermann, W. Jokat, G. Eagles, J. Asseng, H. Miller, D. Steinhage, V. Helm, O. Eisen, D. Jansen, Preserved landscapes underneath the Antarctic Ice Sheet reveal the geomorphological history of Jutulstraumen Basin. *Earth Surf. Process. Landf.* **46**, 2728–2745 (2021). doi:10.1002/esp.5203

42. S. S. Jamieson, C. R. Stokes, N. Ross, D. M. Rippin, R. G. Bingham, D. S. Wilson, M. Margold, M. J. Bentley, The glacial geomorphology of the Antarctic ice sheet bed. *Antarct. Sci.* **26**, 724–741 (2014). doi:10.1017/S0954102014000212

43. C. Lambiel, B. Maillard, M. Kummert, E. Reynard, Geomorphology of the H'erens valley (Swiss Alps). *J. Maps* **12**, 160–172 (2016). doi:10.1080/17445647.2014.999135

44. O. Fredin, G. Viola, H. Zwingmann, R. Sørlie, M. Brönner, J.-E. Lie, E. M. Grandal, A. Müller, A. Margreth, C. Vogt, J. Knies, The inheritance of a Mesozoic landscape in

western Scandinavia. *Nat. Commun.* **8**, 14879 (2017). doi:10.1038/ncomms14879 Medline

45. D. Sugden, Glacial erosion by the Laurentide ice sheet. *J. Glaciol.* **20**, 367–391 (1978). doi:10.3189/S0022143000013915

46. A. M. Hall, K. Ebert, J. Kleman, A. Nesje, D. Ottesen, Selective glacial erosion on the Norwegian passive margin. *Geology* **41**, 1203–1206 (2013). doi:10.1130/G34806.1

47. F. Ferraccioli, T. A. Jordan, D. G. Vaughan, J. Holt, M. James, H. Corr, D. D. Blankenship, J. D. Fairhead, T. M. Diehl, New aerogeophysical survey targets the extent of the West Antarctic Rift System over Ellsworth Land. in *10th International Symposium on Antarctic Earth Sciences*. A. K. Cooper, C. R. Raymond, Eds. (USGS, 2007); Extended Abstract 113, pp. 1–10.

48. T. T. Creyts, F. Ferraccioli, R. E. Bell, M. Wolovick, H. Corr, K. C. Rose, N. Frearson, D. Damaske, T. Jordan, D. Braaten, C. Finn, Freezing of ridges and water networks preserves the Gamburtsev Subglacial Mountains for millions of years. *Geophys. Res. Lett.* **41**, 8114–8122 (2014). doi:10.1002/2014GL061491

49. A. Baranov, A. Morelli, A. Chuvaev, ANTASed–an updated sediment model for Antarctica. *Front. Earth Sci. (Lausanne)* **9**, 722699 (2021). doi:10.3389/feart.2021.722699

50. A. R. A. Aitken, D. A. Young, F. Ferraccioli, P. G. Betts, J. S. Greenbaum, T. G. Richter, J. L. Roberts, D. D. Blankenship, M. J. Siegert, The Subglacial Geology of Wilkes land, East Antarctica. *Geophys. Res. Lett.* **41**, 2390–2400 (2014). doi:10.1002/2014GL059405

51. M. J. Siegert, N. F. Glasser, Convergent flow of ice within the Astrolabe subglacial basin, Terre Adélie, East Antarctica: An hypothesis derived from nummerical modelling experiments. *Polar Res.* **16**, 63–72 (1997). doi:10.3402/polar.v16i1.6625

52. D. E. Sugden, S. S. Jamieson, The pre-glacial landscape of Antarctica. *Scott. Geogr. J.* **134**, 203–223 (2018). doi:10.1080/14702541.2018.1535090

53. D. A. Young, A. P. Wright, J. L. Roberts, R. C. Warner, N. W. Young, J. S. Greenbaum, D. M. Schroeder, J. W. Holt, D. E. Sugden, D. D. Blankenship, T. D. van Ommen, M. J. Siegert, A dynamic early East Antarctic Ice Sheet suggested by ice-covered fjord landscapes. *Nature* **474**, 72–75 (2011). doi:10.1038/nature10114 Medline

54. H. Holtedahl, Notes on the formation of fjords and fjord-valleys. *Geogr. Ann., Ser. A* **49**, 188–203 (1967). doi:10.1080/04353676.1967.11879749

55. O. H. Løken, D. Hodgson, On the submarine geomorphology along the east coast of Baffin Island. *Can. J. Earth Sci.* **8**, 185–195 (1971). doi:10.1139/e71-020

56. D. Sugden, *Landscapes of Glacial Erosion in Greenland and their Relationship to Ice, Topographic and Bedrock Conditions* (Univ. of Aberdeen, 1974); 177–195.

57. H. Ockenden, Data accompanying manuscript: Complex mesoscale landscapes beneath Antarctica mapped from space, v3, Zenodo (2025); http://dx.doi.org/10.5281/zenodo.15223468.

58. H. Ockenden, hockenden97/Antarctic_subglacial_topo: Minor edits to figures, v4.0.0, Zenodo (2025); https://zenodo.org/records/17601672

59. Center for Remote Sensing of Ice Sheets (CReSIS), Radio-echo sounding data repository (Open Polar Data Centre, 2025); https://data.cresis.ku.edu/data/rds/.

60. P. Fretwell, H. D. Pritchard, D. G. Vaughan, J. L. Bamber, N. E. Barrand, R. Bell, C. Bianchi, R. G. Bingham, D. D. Blankenship, G. Casassa, G. Catania, D. Callens, H. Conway, A. J. Cook, H. F. J. Corr, D. Damaske, V. Damm, F. Ferraccioli, R. Forsberg, S. Fujita, Y. Gim, P. Gogineni, J. A. Griggs, R. C. A. Hindmarsh, P. Holmlund, J. W. Holt, R. W. Jacobel, A. Jenkins, W. Jokat, T. Jordan, E. C. King, J. Kohler, W. Krabill, M. Riger-Kusk, K. A. Langley, G. Leitchenkov, C. Leuschen, B. P. Luyendyk, K. Matsuoka, J. Mouginot, F. O. Nitsche, Y. Nogi, O. A. Nost, S. V. Popov, E. Rignot, D. M. Rippin, A. Rivera, J. Roberts, N. Ross, M. J. Siegert, A. M. Smith, D. Steinhage, M. Studinger, B. Sun, B. K. Tinto, B. C. Welch, D. Wilson, D. A. Young, C. Xiangbin, A. Zirizzotti, Bedmap2: Improved ice bed, surface and thickness datasets for Antarctica. *Cryosphere* **7**, 375–393 (2013). doi:10.5194/tc-7-375-2013

61. J. F. Nye, The Motion of Ice Sheets and Glaciers. *J. Glaciol.* **3**, 493–507 (1959). doi:10.3189/S002214300001724X

62. W. Budd, Ice Flow Over Bedrock Perturbations. *J. Glaciol.* **9**, 29–48 (1970). doi:10.3189/S0022143000026770

63. N. Reeh, Steady-State Three-Dimensional Ice Flow over an Undulating Base: First-Order Theory with Linear Ice Rheology. *J. Glaciol.* **33**, 177–185 (1987). doi:10.3189/S0022143000008674

64. G. H. Gudmundsson, Transmission of basal variability to a glacier surface. *J. Geophys. Res.* **108**, 2253 (2003). doi:10.1029/2002JB002107

65. G. H. Gudmundsson, Analytical solutions for the surface response to small amplitude perturbations in boundary data in the shallow-ice-stream approximation. *Cryosphere* **2**, 77–93 (2008). doi:10.5194/tc-2-77-2008

66. T. Thorsteinsson, C. F. Raymond, G. Hilmar Gudmundsson, R. A. Bindschadler, P. Vornberger, I. Joughin, Bed topography and lubrication inferred from surface measurements on fast-flowing ice streams. *J. Glaciol.* **49**, 481–490 (2003). doi:10.3189/172756503781830502

67. A. S. Gardner, G. Moholdt, T. Scambos, M. Fahnstock, S. Ligtenberg, M. van den Broeke, J. Nilsson, Increased West Antarctic and unchanged East Antarctic ice discharge over the last 7 years. *Cryosphere* **12**, 521–547 (2018). doi:10.5194/tc-12-521-2018

68. G. H. Gudmundsson, M. Raymond, On the limit to resolution and information on basal properties obtainable from surface data on ice streams. *Cryosphere* **2**, 167–178 (2008). doi:10.5194/tc-2-167-2008

69. D. A. Young, J. D. Paden, J. S. Greenbaum, D. D. Blankenship, M. E. Kerr, S. Singh, S. R. Kaundinya, K. Chan, D. P. Bhul, G. Ng, S. D. Kempf, COLDEX Open Polar Radar MARFA Airborne Radar Data, Texas Data Repository (2024); https://doi.org/10.18738/T8/J38CO5.

70. J. C. Russ, *Fractal surfaces* (Springer, 2013), 10.1007/978-1-4899-2578-7.

71. J. B. Florindo, O. M. Bruno, Fractal descriptors based on Fourier spectrum applied to texture analysis. *Physica A* **391**, 4909–4922 (2012). doi:10.1016/j.physa.2012.03.039

72. A. P. Stroeven, J. Kleman, Age of Sirius Group on Mount Feather, McMurdo Dry Valleys, Antarctica, based on glaciological inferences from the overridden mountain range of Scandinavia. *Global Planet. Change* **23**, 231–247 (1999). doi:10.1016/S0921-8181(99)00059-4

73. S. S. Jamieson, D. E. Sugden, N. R. Hulton, The evolution of the subglacial landscape of Antarctica. *Earth Planet. Sci. Lett.* **293**, 1–27 (2010). doi:10.1016/j.epsl.2010.02.012

74. D. Sugden, A. Hall, Antarctic blue-ice moraines: Analogue for Northern Hemisphere ice sheets? *Quat. Sci. Rev.* **249**, 106620 (2020). doi:10.1016/j.quascirev.2020.106620

75. M. Frezzotti, S. Gandolfi, S. Urbini, Snow megadunes in Antarctica: Sedimentary structure and genesis. *J. Geophys. Res.* **107**, ACL–1 (2002). doi:10.1029/2001JD000673

76. A. M. Smith, T. Murray, Bedform topography and basal conditions beneath a fast-flowing West Antarctic ice stream. *Quat. Sci. Rev.* **28**, 584–596 (2009). doi:10.1016/j.quascirev.2008.05.010

77. E. C. King, H. D. Pritchard, A. M. Smith, Subglacial landforms beneath Rutford Ice Stream, Antarctica: Detailed bed topography from ice-penetrating radar. *Earth Syst. Sci. Data* **8**, 151–158 (2016). doi:10.5194/essd-8-151-2016

78. C. A. Schelpe, G. H. Gudmundsson, Incorporating Horizontal Density Variations Into Large-Scale Modeling of Ice Masses. *J. Geophys. Res. Earth Surf.* **128**, e2022JF006744 (2023). doi:10.1029/2022JF006744

79. H. F. J. Corr, D. G. Vaughan, A recent volcanic eruption beneath the West Antarctic ice sheet. *Nat. Geosci.* **1**, 122–125 (2008). doi:10.1038/ngeo106